Projet de fin d'études

Electrohydrodynamics of the asymmetric electrode array micropump

Lionel Belmon

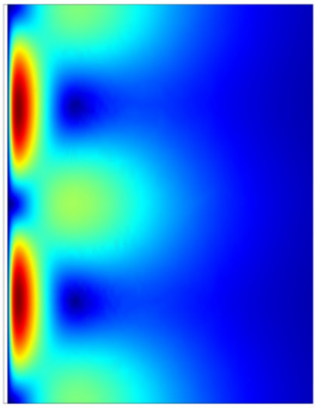

Supervisors: Henrik Bruus and Niels Asger Mortensen

MIC – Department of Micro and Nanotechnology
Technical University of Denmark

15 September 2004

Abstract

Within the past years, interest in microfluidic devices has grown in multiple fields such as biology, medicine, and electronics. In order to fully integrate complex processing systems on chips, micro-pumps are essential. This thesis presents a study of electroosmotic pumping based on asymmetric electrode-arrays subject to an AC voltage bias.

We first introduce the basic equations for microfluidics with charged solutions: the Navier-Stokes equation, the Nernst-Planck equation, and the Poisson equation, which define the frame of the analytical work of the thesis. The fundamentals of electroosmosis are then presented along with various experimental results for pumps and electrode-arrays.

Extending the work of Ajdari, we then develop a model for electrolytes driven by modulated surface potentials where we fully resolve the Debye layer dynamics. With my supervisors we submitted a paper to Physical Review E presenting this work. Afterwards, the theory of the asymmetric electrode-array pump is introduced and we discuss the spatial and temporal asymmetry of the system. When compared with experimental data, our results give a good agreement for resonance frequencies. The high frequency regime is then investigated in order to understand unexpected dynamics discovered by experimental studies. Finally, we present numerical results obtained from finite elements simulations and compare them with analytical and experimental data.

Resumé

Au cours des dernières années, l'intérêt dans les composants microfluidiques a grandi dans de nombreux domaines, tels la biologie, la médicine ou l'électronique. Pour intégrer des process complexes au sein d'une même puce, les micro-pompes sont essentielles. Ce rapport présente une étude d'une pompe electroosmotique basée sur un réseau d'électrodes asymétriques soumises à une tension alternative.

En premier lieu, nous introduisons les équations de base pour des solutions chargées au sein d'un système microfluide: les équations de Navier–Stokes, l'équation de Nernst–Planck et l'équation de Poisson, qui définissent le cadre du travail analytique de ce projet. Les principes fondamentaux de l'electroosmose sont ensuite exposés ainsi que des résultats expérimentaux pour diverses micropompes et réseaux d'électrodes.

Nous développons par la suite un modèle pour les électrolytes soumises à des potentiels modulés, où nous résolvons complètement la couche de Debye. Conjointement avec mes superviseurs, nous avons soumis un article a Physical Review E décrivant ce travail. Par la suite, la théorie de la pompe à électrode asymétrique est présentée et nous discutons de l'asymétrie spatiale et temporelle de la pompe. Nous obtenons une bonne corrélation entre les fréquences de résonance trouvées expérimentalement et celles données par notre modèle. Le domaine des hautes fréquences est étudié afin de comprendre des phénomènes inattendus découvert par une campagne d'expériences. Enfin, nous présentons des résultats numériques obtenus a l'aide de simulations éléments finis et les comparons aux données expérimentales et analytiques.

Preface

The present work is a ”Travail de Fin d’Etudes” which is the final part of my engineering studies at the Ecole Centrale de Nantes. The work has been carried out from April to September 2004 in the Microfluidics Theory and Simulation (MIFTS) group at MIC, DTU, under the dedicated supervision of Henrik Bruus and Niels Asger Mortensen. I would like to thank Laurits Højgaard Olesen and Fridolin Okkels for their precious help. I would also like to thank Goran Goranovic and Henrik Bruus for the e-mail correspondence that convinced me to join the group for doing my Master thesis. Finally, I would like to thank everybody from the MIFTS group for the stimulating and nice work atmosphere I experienced during my stay.

Lionel Belmon
MIC – Department of Micro and Nanotechnology
Technical University of Denmark
15 September 2004

Contents

List of figures xiv

List of tables xv

List of symbols and constants xvii

1 Introduction 1
1.1 micropumps and applications 1
1.2 topics treated in the thesis 3

2 Microfluidics basic physics 5
2.1 Continuity 5
2.2 Navier–Stokes equation 5
2.3 Simplified Navier–Stokes equation for microfluidics 6
2.4 Solution of charged species 7
2.4.1 Diffusion 7
2.4.2 Electromigration 7
2.4.3 Convection 7
2.4.4 Nernst–Planck equation 8
2.4.5 Poisson equation 8
2.5 Electric Double layer 8
2.5.1 Stern layer 8
2.5.2 Debye layer 9
2.5.3 Zeta potential 9
2.6 Chemical reactions 10

3 Electroosmotic micropumps 11
3.1 Electroosmotic flow 11
3.2 EO pumps overview 12
3.2.1 characteristics 12
3.2.2 DC micropumps design 13
3.2.3 AC micropumps design 13
3.3 Experimental data for electrode-arrays 14
3.3.1 Symmetric electrode-array 14

3.3.2 AC electrode-array pump 14

4 Electrolytes driven by modulated surface potentials 17
4.1 Introduction 17
4.2 Non-equilibrium description 18
4.2.1 The insulating layer, $-d < x < 0$ 18
4.2.2 The electrolyte, $x > 0$ 18
4.2.3 Boundary conditions 19
4.3 Static regime, ω =0 20
4.4 Dynamic regime, $\boldsymbol{\omega} > 0$ 20
4.4.1 Debye–Hückel approximation 21
4.4.2 Diffusive regime 21
4.4.3 Long-period and low-frequency modulation 22
4.4.4 Body-force 22
4.4.5 Linearized flow in quasi-steady state 24
4.4.6 Debye layer flow 24
4.4.7 Bulk flow 25
4.5 Discussion 25
4.6 Conclusion 27

5 Theory of an asymmetric electrode array pump 29
5.1 Asymmetric potential 29
5.1.1 Perturbated potential 29
5.1.2 General geometry 30
5.2 Asymmetric surface capacitance 31
5.2.1 Averaged body force 31
5.2.2 Averaged bulk flow 32
5.3 High frequency regime 33
5.3.1 Diffusive break-down, $\omega > \omega_D$ 34
5.3.2 Body-force balance 34
5.3.3 Discussion 37

6 FEMLAB, a finite element solver 39
6.1 The finite element method 39
6.2 FEMLAB 39
6.2.1 Hardware 40
6.2.2 equations formulation 40
6.2.3 FEMLAB limitations 41

7 Numerical simulations 43
7.1 Problem setup 43
7.1.1 Equations solved in the computational domain 43
7.1.2 Boundary conditions 44
7.2 Mesh issues 45

7.2.1 New coordinate system . . . 45
7.2.2 Mesh transformation . . . 46
7.3 Symmetric cosine modulation . . . 47
7.3.1 Numerical and analytical results . . . 47
7.3.2 Voltage dependence for the cosine modulation . . . 49
7.3.3 Frequency dependence for the cosine modulation . . . 49
7.3.4 Computation over the voltage-frequency domain . . . 50
7.4 Simple symmetric electrode . . . 51
7.4.1 simulation setup . . . 51
7.4.2 Frequency dependence for the symmetric electrodes . . . 52
7.5 The Brown pump . . . 53
7.5.1 Streamlines . . . 53
7.5.2 Frequency dependence . . . 53
7.6 Discussion . . . 54

8 Conclusion 55

A Electrode-array with non-zero zeta potential 57
A.1 Non-zero intrinsic zeta potential . . . 57
A.1.1 Zeroth order result . . . 59
A.1.2 First order equations . . . 60
A.1.3 Body force . . . 62
A.2 Discussion . . . 63

B Mesh transformation: a test 65
B.1 Analytical problem . . . 65
B.2 Script listing . . . 65

C Paper submitted to Phys. Rev. E 67

Bibliography 75

List of Figures

1.1 Inkjet printhead schematic. 2
1.2 Micropumps pictures 2

2.1 Structure of electric double layer. 9
2.2 Silicon in aqueous solution 10

3.1 Principle of EO pumping 12
3.2 Sketch of DC EO pumps. 13
3.3 Experimental setup for symmetric electrode-array 14
3.4 Experimental results for symmetric electrode-array 15
3.5 Experimental setup for asymmetric electrodes array 15
3.6 Experimental results for asymmetric electrodes array 16
3.7 Asymmetric electrodes array, flow reversal 16

4.1 Sketch of the symmetric problem 17
4.2 Potential and pressure for the symmetric problem 23
4.3 Velocity field in the bulk and in the Debye layer 24

5.1 Sketch of the potential 29
5.2 Potential obtained with a Fourier series 31
5.3 ν: diffusive breakdown 34
5.4 Plot of the body-force balance versus x 35
5.5 Plots of the integrated body force balance 36
5.6 Plots of the integrated body force balance 36

6.1 Structured and unstructured meshes 41

7.1 Boundary conditions for the simulations 44
7.2 Transformed mesh 46
7.3 Velocity field for the cosine modulation 47
7.4 Numerical error 48
7.5 Voltage dependence 49
7.6 Plots of time-averaged velocity against ω 50
7.7 3D Plots of velocity against voltage and frequency. 50
7.8 Boundary conditions for the Green setup 51

7.9 Comparison between experimental and numerical streamlines 52
7.10 Plots of velocity over the symmetric electrodes against frequency 52
7.11 Velocity field over the asymmetric electrodes 53
7.12 Plots of pumping velocity against ω 54

8.1 Summary of the cases studied 56

A.1 Potential and charges in the Debye layer 62
A.2 Equipotential lines for ϕ_1 for $q\lambda_D = 0.1$, $t = 0$, and $\omega = 0$. 62

List of Tables

4.1 Typical values of central parameters. 26

5.1 ω^* calculated for the Brown [1] and Mpholo [2] experiments 34
5.2 Debye frequencies for given parameters 37

7.1 Typical parameters for the symmetric cosine simulations 48

List of symbols

Symbol	Description	Unit	Value
N_A	Avrogado Number	mol^{-1}	6.022×10^{23}
k_{B}	Boltzmann constant	J K^{-1}	1.381×10^{-23}
e	Elementary charge	C	1.602×10^{-19}
ϵ_0	Vacuum permittivity	C (V m)$^{-1}$	8.854×10^{-12}
ϵ	Permittivity	C (V m)$^{-1}$	$\sim 78\,\epsilon_0$ for water at 20^oC
ρ	Mass density	kg m^{-3}	1.0×10^3 for water at 20^oC
η	Dynamic viscosity	kg m^{-1} s^{-1}	$\sim 10^{-3}$
T	Temperature	K	300 at room temperature
$\mathbf{E}$	Electrical field	V m^{-1}	
$\mathbf{F}$	Body force	N	
$\mathbf{i}$	Particle flux	m^{-2} s^{-1}	
$\mathbf{j}$	Current flux	C m^{-2} s^{-1}	
$\mathbf{r}$	Position	m	
$\mathbf{v}$	Velocity	m s^{-1}	
ϕ	Potential	V	
φ, Φ	Phase	rad	
ν	Charge density	C m^{-3}	
n	Particle density	m^{-3}	
D	Ionic diffusivity constant	m^2 s^{-1}	
v	Speed	m s^{-1}	
p	Pressure	N m^{-2}	
t	Time	s	
q	Spatial modulation	m^{-1}	
ω	Pulsation	s^{-1}	
ω_D	Debye frequency/pulsation	s^{-1}	
λ_D	Debye length	m	

Chapter 1

Introduction

1.1 micropumps and applications

The interest in microfluidics has grown in the past decade for multiple reasons. We can put forward the ever increasing need of automation in biochemistry laboratories for instance. From this has emerged the concept of lab-on-a-chip, sometimes referred as micro total analysis system (μTAS). Those new technologies are promising and may dramatically change medical and chemical analysis. In miniaturizing all the components needed for sample analysis, it is possible to integrate them on a single chip. Such devices provide many advantages when compared to classical methods: low sample consumption, reduced size, high degree of automation, and — in cases of successful mass-production — cheap systems. An example of an application of the Lab-on-a-chip can be found in [3], where a chip is proposed as a solution for fast genotyping from blood samples. To handle samples and reagents, a fully integrated device would need self-contained components able to generate proper fluid flows. This can be achieved by the means of miniaturized pumps. Yet, those micropumps are found in very few current generation systems. Those systems often rely on macro scale pumps outside the chip and thus are not totally integrated.

In addition to driving flows in a lab-on-a-chip, there are numerous applications for micropumps, such as implanted insulin delivery systems for diabetics, microelectronic cooling or even micro-space exploration. The reader can find a detailed review of micropumps in [4], [5].

We will now briefly present the main types of existing designs for pumps:

- Mechanical pumps
  "pumps in which moving boundaries do pressure work on the working fluid in a periodic manner" [4]. This definition applies mainly to piezoeletric, electrostatic, or pneumatic based pumps. A common example of this kind of pump can be found in some inkjet printers (see Fig. 1.1). The printhead uses a a piezoelectric actuator to eject a droplet of ink.

- Electrohydrodynamic pumps
  Electrohydrodynamic pumps rely on the interaction of electrostatic forces with ions

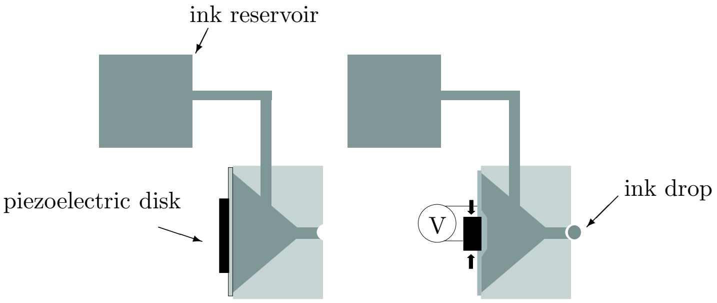

Figure 1.1: IBM inkjet printhead schematic. The volume of the chamber is varied by using a piezoelectric disk actuator.

in dielectric fluids. This type of pump needs the existence of a space charge in the fluid in order to obtain a Coulomb force that can drive the fluid. This is an important limitation, especially for bio-applications.

- Electroosmotic (EO) pumps
  Electroosmotic pumping is based on the double-electrical layer that forms on charged surfaces. The charges subject to a tangential DC electrical field generate a body force that drives the fluid in a near wall region. Due to viscosity, this layer of moving fluid generates a bulk flow in the rest of the channel. Some more complex design implies AC currents such as described in this thesis.

In 2000, a new design for AC EO pumps was introduced by Ajdari in [6], based on asymmetric electrode-array. Even though this thesis deals only with the pumping application, electrode-arrays have been used for other purposes such as separation of particles, viruses, DNA, or proteins [7]. However those topics are not discussed in this work.

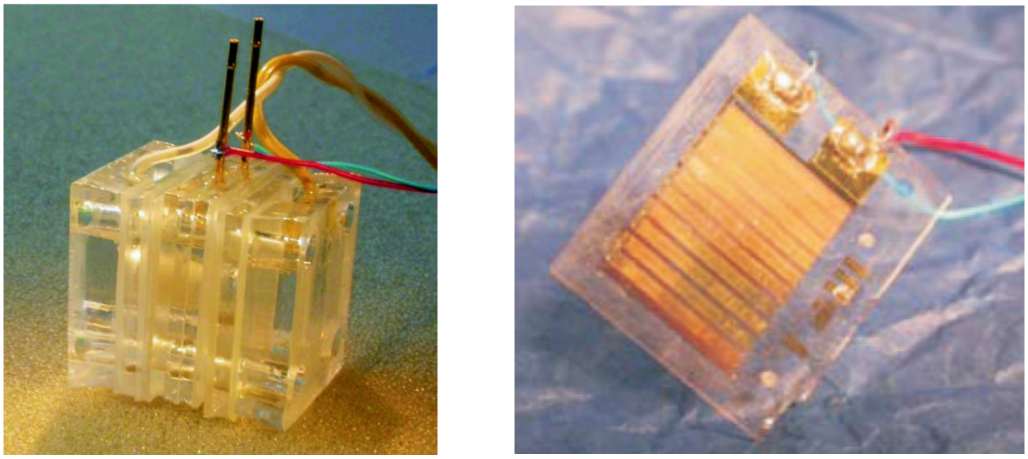

Figure 1.2: Micropumps produced and designed at MIC by Brask, Arnoldus, Hansen ([8] and [9]). The left-hand side shows a DC porous pump and the right hand-side an asymmetric electrode-array pump.

1.2 topics treated in the thesis

This thesis deals with a new concept of electroosmotic pump, based on asymmetric electrode-arrays. We give here a brief overview of the contents of the thesis.

- Basic microfluidics physics
  In this chapter, we introduce the fundamental frame of equations used in microfluidics, to describe both the hydrodynamics and the electrokinetics.

- Electroosmotic pumps
  After describing the fundamental equations, the principle of electroosmotic pumping is exposed. We then introduce various reported designs of micro-pumps and give some fundamental experimental results for the electrode-arrays.

- Theory of the symmetric electrode-array for driving electrolytes flow
  We investigate the electrokinetics inducing fluid flow over electrode-arrays. Together with my supervisors, I submitted a paper (see Ref. [10]) presenting this work.

- Theory of an asymmetric electrode-array pump
  A theory of this design, originally proposed by Ajdari in [6], is given here. Moreover, we investigate the limits of our analytical model along with the high frequency regime.

- FEMLAB: a commercial finite element solver
  We introduce here the finite element method solver FEMLAB which was used for the simulations presented in this thesis. We also discuss the limitations of the Finite Element Method for our problem.

- Simulations
  In this chapter, I present and discuss some numerical results with analytical and experimental data.

Chapter 2

Microfluidics basic physics

This chapter is directly inspired by Chap. 2 and Chap. 3 in the book of Probstein [11]. We introduce here the main equations used in this thesis. However, this chapter is not exhaustive and deals only with the problems encountered within the frame of our work.

2.1 Continuity

In the frame of this thesis, we deal with problems down to nanometric scales. The Navier–Stokes equation is the classical governing equation for fluids. Yet, this formulation makes the assumption that the fluid is a continuum, which means that all macroscopic length scales are considerably larger than the largest molecular length scales. The molecular spacing λ_{mol} is given by

$$\lambda_{mol} = \big(\frac{M}{\rho N_A}\big)^{\frac{1}{3}}, \tag{2.1}$$

where M is molar mass, N_A the Avrogado number and ρ the mass density. For pure water we have

$$\lambda_{mol} = \Big[\frac{18 \times\, 10^{-3}\,\mathrm{kg.mol^{-1}}}{6.022 \times 10^{23}\,\mathrm{mol^{-1}}\;\, 1 \times 10^{3}\mathrm{kg.m^{-3}}}\Big]^{1/3} \simeq 0.31\,\mathrm{nm}.$$

The continuum assumption is then valid for length scales $\ell \geq 1\,\mathrm{nm}$, where we can apply the Navier–Stokes equation to describe the fluid.

2.2 Navier–Stokes equation

The equation system governing fluid flow is composed of the continuity equation (or mass conservation equation), the momentum equation (the Navier–Stokes equation) and the equation for the energy.

- The continuity equation takes the form

$$\partial_t\, \rho + \boldsymbol{\nabla} \cdot (\rho\, \mathbf{v}) = 0. \tag{2.2}$$

In this thesis, we suppose the fluid is incompressible and that ρ is constant[1]. We then have

$$\boldsymbol{\nabla} \cdot \mathbf{v} = 0. \tag{2.3}$$

- The momentum equation
  We only consider the case of Newtonian fluid (where the shear stress is proportional to the strain rate, by a factor η, the viscosity). The momentum equation for a Newtonian fluid is then

  $$\rho\,(\partial_t \mathbf{v} + \mathbf{v} \cdot \boldsymbol{\nabla} \mathbf{v}) = -\boldsymbol{\nabla} p + \eta \boldsymbol{\nabla}^2 \mathbf{v} + \mathbf{F}, \tag{2.4}$$

  where $\mathbf{F}$ are the body forces such as electrostatics forces or gravity. In this thesis, we will mainly deal with electrical forces and will neglect gravity. The left-hand side is usually a source of problem when dealing with the Navier–Stokes equation since it is non-linear. However, we will show that, under certain assumptions valid in microfluidics, we can linearize the momentum equation (see Sec. 2.3).

- Energy equation
  For an elemental volume of fluid, we can write (see Ref. [12]):

  $$\partial_t \big[\, \frac{1}{2} \rho\, v^2 + \rho\, U_{int} \,\big] = -\boldsymbol{\nabla} \cdot \big[\, \rho\, \mathbf{v} (\frac{1}{2} v^2 + H) - \mathbf{v} \cdot \tau^{'} - \rho\, c_p\, D_{heat}\, \boldsymbol{\nabla} T \,\big], \tag{2.5}$$

  where $\rho\, H$ is the enthalpy density and $\tau^{'}$ the stress-tensor. The left-hand side is the rate of change of the kinetic energy and the thermal energy. The right hand side is the energy flux. In viscous flow we have a dissipation of kinetic energy into heat via irreversible process. However, we will not deal with dissipation and thermal matters in this thesis and we will not discuss further about the energy equation. Yet, the thermal issues are to be considered when dealing with EO-pumping because of the Joule effect. A short study of the efficiency of EO-pumping has been done in Ref. [13]. Data for various pumps, including mechanical ones, has been collected in Ref. [4].

2.3 Simplified Navier–Stokes equation for microfluidics

The Reynolds number, defined by the ratio of momentum transported by convection and the momentum transported by viscous diffusion is commonly written as $Re = \rho\, v\, L/\eta$ where L is a characteristic length scale of the flow. For microfluidic devices we can make a simple calculation with $L \sim 10^{-6}$ m and $v \sim 10^{-3}$ m.s^{-1}. The Reynolds number is then 10^{-3}. Even with high velocities in the channels, the Reynolds number will still be very small compared to unity. This means that we can neglect all inertial effects in the Navier–Stokes equation, Eq. (2.4). Moreover, since the Reynolds number $Re \ll 1$ we can of course assume that the flow is laminar. A turbulent flow is very unlikely in a microfluidic device.

---

[1] However, one can argue that, in the general case, the incompressibility constraint is not equivalent to ρ being constant.

In our linearized momentum equation, we only have the viscous forces $\eta\boldsymbol{\nabla}^2\mathbf{v}$, the body force $\mathbf{F}$ and the pressure gradient $\boldsymbol{\nabla}p$:

$$0 = -\boldsymbol{\nabla}p + \eta\boldsymbol{\nabla}^2\mathbf{v} + \mathbf{F}. \tag{2.6}$$

2.4 Solution of charged species

Let us consider a solution of ions, sufficiently dilute so that the species and their gradients do not interact. We wish now to write the equations for the ionic flux. In this chapter, we will handle particle densities instead of molar concentrations. Nevertheless, it is easy to rewrite our results using the Faraday constant :

$$F = N_a\, e. \tag{2.7}$$

2.4.1 Diffusion

For each of the species in the considered solution, a diffusion of mass will occur. This is a consequence of molecular motion. Fick's first law of diffusion states that there is a linear relation between the particle flux and the particle concentration gradient, which we can state by writing for the i_{th} specie:

$$\mathbf{i}_i^{\mathrm{D}} = -D_i\, \boldsymbol{\nabla}\, n_i, \tag{2.8}$$

where the proportionality constant D_i is the ionic diffusivity. Typical values of D are around 10^{-9} m^2 s^{-1}. The reader can find a table giving the diffusivity for common electrolytes solution in Ref. [11], p.25.

2.4.2 Electromigration

Under the action of an electric field, forces act on the different species, giving rise to a mass transfer called electromigration. The force exerted on a particle is then $Z_i e\,\mathbf{E} \equiv -Z_i e \boldsymbol{\nabla}\phi$. The flux due to migration in an electric field is proportional to the force acting on the particle multiplied by the particle concentration, which means that, for the i_{th} specie

$$\mathbf{i}_i^{\mathrm{em}} = -\mu_i\, n_i \boldsymbol{\nabla}\phi, \tag{2.9}$$

where the proportionality constant μ is the mobility. Diffusivity and mobility are directly related by the Nernst–Einstein equation :

$$\mu_i = \frac{Z_i\, e}{k_{\mathrm{B}}\, T}\, D_i. \tag{2.10}$$

2.4.3 Convection

In the case of fluid motion, we have a particle flux induced by convection, which we can write as

$$\mathbf{i}_i^{\mathrm{conv}} = n_i\, \mathbf{v}. \tag{2.11}$$

We will see in Chap. 4 that the convection is a source of problem: it induces a coupling between the Navier–Stokes equation and the electrokinetics.

2.4.4 Nernst–Planck equation

We sum the contribution of electromigration, diffusion and convection to write down the so-called Nernst–Planck equation for the i_{th} specie :

$$\mathbf{i}_i = \mathbf{i}_i^{\text{D}} + \mathbf{i}_i^{\text{em}} + \mathbf{i}_i^{\text{conv}} \tag{2.12a}$$

$$= -D_i \boldsymbol{\nabla} n_i - \mu_i \, n_i \boldsymbol{\nabla} \phi + n_i \mathbf{v}. \tag{2.12b}$$

Along with the continuity equation for the i_{th} specie

$$\partial_t n_i = -\boldsymbol{\nabla} \mathbf{i}_i \,, \tag{2.13}$$

where $\mathbf{i}$ is the particle current, we have

$$\partial_t n_i + \boldsymbol{\nabla}\big[- D_i \boldsymbol{\nabla} n_i - \mu_i \, n_i \boldsymbol{\nabla} \phi + n_i \mathbf{v}\big] = 0. \tag{2.14}$$

2.4.5 Poisson equation

An electrolyte used in EO pumps, for example, could be a solution of NaNO_3, Ref. [1]. The electrolyte is then a region where there exists a charge density, commonly taken to be 0 since the electrolyte is globally neutral. However, we will see in Sec. 2.5 that this is not true in the frame of this work. We consider the electrolyte to be an isotropic dielectric. We can then write the Poisson equation

$$\boldsymbol{\nabla}^2 \phi(\mathbf{r}, t) = -\frac{1}{\epsilon}\, \nu = -\sum_i \frac{1}{\epsilon}\, Z_i e \, n_i, \tag{2.15}$$

where ν is the charge density.

2.5 Electric Double layer

When brought into contact with an aqueous solution, most materials will acquire a surface electric charge due to mechanisms such as ionization, adsorption and ion dissolution. In the case of an electrolyte solution, the distribution of ions will be affected by those charges near the solid/fluid interface. Let us suppose that the surface charges are positive. The negatively charged ions will then be attracted to the surface where as the positives ions will be repelled. Taking into account diffusive and thermal effects, a double electric layer is then formed as shown in Fig. 2.1

2.5.1 Stern layer

The Stern layer is the inner layer where electrical forces dominate. The ions are bound tightly and cannot slip on the charged surface. As this layer contains charges it can be described — in a simple model — as a capacitor. This will be discussed in Chap. 4. At the interface between the Stern layer and the rest of the electrolyte, a zeta (ζ) potential is defined. However, this is not a very precise physcial definition of the ζ potential. This topic will be discussed in Sec. 2.5.3

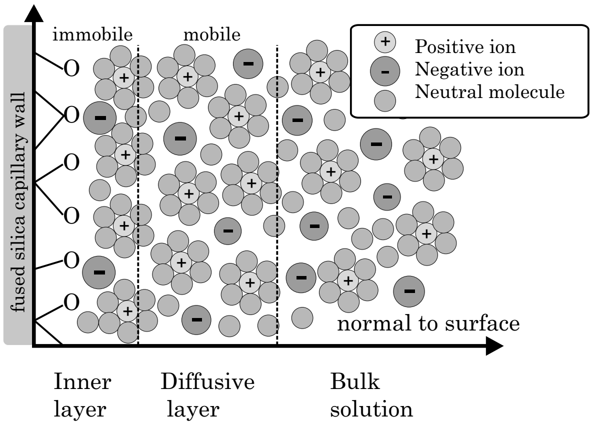

Figure 2.1: Structure of electric double layer with an inner immobile layer. The system wall–liquid is electrically neutral. The positive ions are hydrated. Some of the negative ions are specifically adsorbed at the surface. Fig. from Brask, [13].

2.5.2 Debye layer

In the Debye layer a balance is established between the electrical forces and diffusion (see Eq. (2.12a)). The concentrations of ions relaxes in this layer from the surface concentration to the bulk concentration. This layer can be directly solved analytically in a 1D problem using Eq. (2.12a), Eq. (2.15) and Eq. (2.13) (see Ref. [11] p. 191). However, in this thesis we will mainly deal with a 2D problem coupled with fluid motion. To handle simpler equations we work in the frame of the Debye-Hückel approximation. We then write

$$n = n_* + \delta n \text{ with } \delta n \ll n_* \tag{2.16}$$

where n_* is the unperturbed particle density in the bulk and δn the perturbation of the density in the Debye layer. This approximation is valid when the thermal energy dominates over the electrostatic energy:

$$Z\,e\,\zeta \ll k_{\mathrm{B}}\,T. \tag{2.17}$$

It is then possible to linearize the problem and obtain exponentially decaying solutions over a defined length scale λ_D. A 2D case with spatial modulation is solved in Chap. 4.

2.5.3 Zeta potential

In Sec. 2.5.1, we introduced the Stern layer which is a layer of immobile ions bound by electrical forces on the surface. The zeta potential is defined as the potential at the *shear surface* between the stern layer and the electrolyte solution (see Ref. [11]). This potential is typically of the order of 1-200 mV. Capillaries in microfluidic devices are made of glass, polymers or siliconoxide. If siliconoxide is immersed in water, chemical reactions occurs at the surface and induce a potential. The silanol groups SiOH form SiOH_2^+ or SiO^- depending on the pH of the solution (see Fig. 2.2). Thus the zeta potential is dependent on the pH of the buffer solution used and have an important influence on the electroosmotic effects. It is also possible to adjust the zeta potential by using various coatings on the surfaces. Even if Electroosmosis is usually based on the existence of a zeta potential, the electrode-array theory introduced in Chap. 4 assumes that the zeta potential is vanishing.

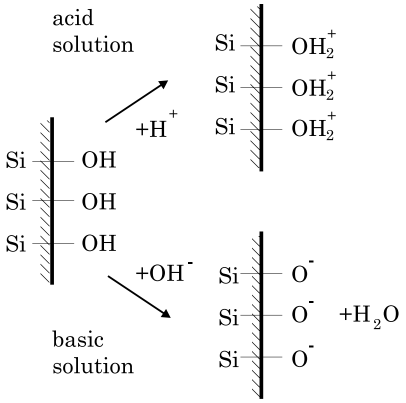

Figure 2.2: Silicon in aqueous solution for basic and acid pH. Note the difference of surface charges for different pH. Fig. from Brask [13]

2.6 Chemical reactions

Up to this point, we have considered that no chemical reactions occured in our system, once the equilibrium is established. When dealing with electrolytes and electrodes, we are exposed to such phenomena as electrolysis. For example, we may encounter the dissociation of water in H_2 and O_2. This is to be avoided for the following reasons :

- capillaries and bubbles
  Bubbles in microfluidic devices causes important problems since they can clog microchannels because of surface tension.

- pumping and bubbles
  Since the gaseous bubbles are not incompressible fluids, it is likely that, instead of inducing flow, the generated pressure will act on the bubbles volume.

- electrodes and electrolysis
  Electrolysis may damage the thin electrodes used in our systems and lead to the destruction of the pump.

For all those reasons we want to avoid any chemical reactions. We must choose our applied potentials carefully.
In the following chapters, we consider the situation with no chemical reactions in the electrolyte. This implies that we have no charge injections from the electrodes. The electrodes are thus considered as ”ideally polarizable” or ”completely blocking without Faradaic processes”, Bazant [14]. The ionic fluxes vanishes at the fluid-electrode interface. If we consider the electrode to be an infinite surface at $x = 0$ then

$$\mathbf{i}\,\big|_{x=0} = 0. \tag{2.18}$$

The reader can find more details about charge injection for the AC EO pump in Ref. [6] and Ref. [14].

Chapter 3

Electroosmotic micropumps

3.1 Electroosmotic flow

We do not intend to study in detail electroosmotic (EO) flow in this chapter, but only to introduce the fundamental facts. The reader may find a comprehensive study of electroosmotic flows in micro-channels in Ref. [11] and Ref. [13].
Electroosmostic flow was first described in 1809 by Reuss, (see [11] p.195). Under the influence of an electric field, water can migrate through porous clay diaphragms. This is now a well understood phenomenon. Let us consider the porous diaphragm as a infinite number of parallel micro-channels. We suppose moreover that the water contains a given concentration of ions. The EO pumping relies then on two effects :

- Debye layer
  On the walls of the micro channel, let us assume the existence of a constant potential, this potential may be intrinsic (in the case of clay, the surface carries negative charges, giving rise to a ζ potential) or imposed via a voltage source. This generates a charged electrical double layer composed of ions, as described in Chap. 2.

- Parallel electrical field
  We now introduce an electrical field parallel to the walls of the channel. This field will generate a body force, due to the ions in the debye layer, as shown in Fig. 3.1. The charged ions are subject to an electrical force, generating motion in the Debye layer. Momentum is then transferred to the fluid bulk by viscosity. The source of the electrical field is usually a cathode and an anode disposed at both end of the channel.

In the microfluidic area, EO flows have been a matter of interest during the past years. A number of important processes used on lab-on-a-chip relies on EO flows such as electrophoretic separation or liquid chromatography. For pumping purpose, EO flow provides various advantages over the mechanical induced flow. There is no moving parts and the design of an EO pump is thus usually simpler. Moreover the flow profile is not hyperbolic like in pressure driven flow but is flat (see Fig. 3.1), which can be interesting in some applications (see Ref. [15]). However, EO pumping is limited by an important drawback: its poor efficiency due to the Joule effect. The efficiency can be defined as

$$\eta = \frac{\Delta p \; Q}{P}, \tag{3.1}$$

where Δp is the pressure built by the pump, Q the flow rate and P the power delivered to the pump. In the DC case, we have $P = V^2 \, \sigma_{\text{elec}}$ with σ_{elec} being the conductivity of the electrolyte and V the applied voltage. Taking some values from Ref. [4], the reported EO pumps have a typical thermodynamic efficiency under 1 %. This means that most of the energy is dissipated into heat. This heat can be a source of problem in some devices. This heat must be evacuated and can interfere with some process downstream the pump.

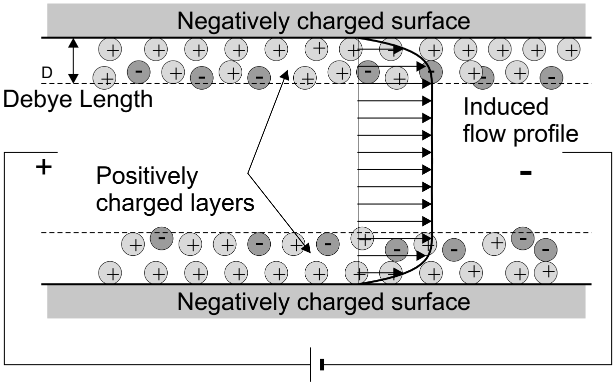

Figure 3.1: Principle of electroosmotic pumping. The charged layers, induced by the electrodes potential, are driven by the parallel electrical field along the channel.Viscosity transfers the momentum to the rest of the fluid. In the case of a vanishing back-pressure, the flow profile is flat in the bulk. (Brask, [13])

3.2 EO pumps overview

We will now give some brief description of various characteristic of the DC Electroosmotic pumps.

3.2.1 characteristics

The manufacturing of EO pumps is usually achieved by various techniques comparable to what is made in common electronics, such as lithography. Microumps are usually based on a thick glass wafer where thin layers of metals are deposited. As this thesis does not deal with manufacturing, the reader should refer to Ref. [16] and Ref. [9] to have more information about this topic.

Microfluidic channels typical dimensions are $1 - 300\mu$m with various shapes depending on the fabrication process. For example, laser ablation gives the channels a gaussian profile. Materials include silicon and various polymers such as PMMA.

Usually the electrodes are made of metal. Because of manufacturing and/or chemical matters, electrodes can be composed of multiple layers of different metals as seen in Ref. [17]. Gold, platinum, titanium or chrome are used for their various interesting properties. However gel electrodes and more complex systems have been reported (see Ref. [18]).

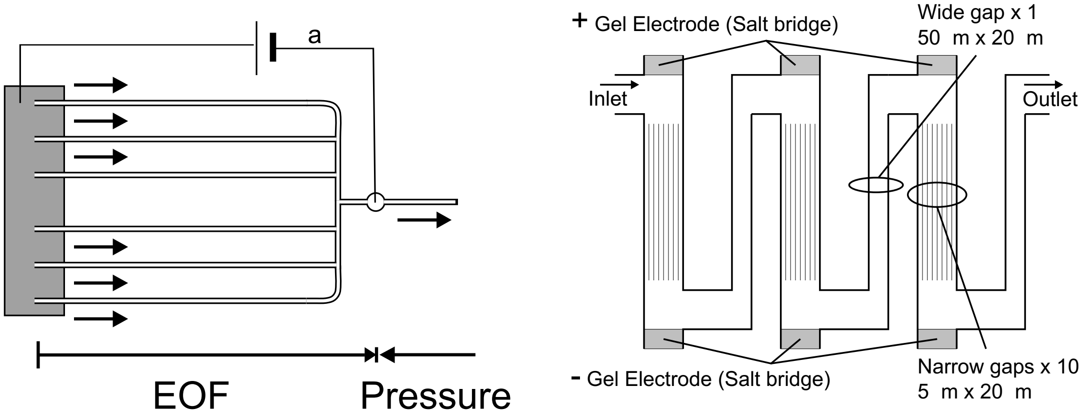

Figure 3.2: On the left-hand side, a sketch of a parallel EO pump with six channels. The flow rate of the channels sums, however it is not possible to build important pressure gradient. On the right-hand side, a sketch of a cascade EO pump, with a narrow and a wide section. The pumping is generated in the narrow section. This design allows to build up pressure gradient sequentially. Figs. taken from (Brask, [13]).

3.2.2 DC micropumps design

- Parallel pumps
  The parallel (see Fig. 3.2) pump is designed to achieve high flow rates. Adding EO pumps in parallel allows to reach higher flow rates with relatively low voltage (see Fig. 3.2). The use of a porous structure (or fritz) is a possible solution to achieve high parallelization of EO pumping. The pores can be downsized down to 0.2 μm (see Ref. [8] and Ref. [19]).

- Pumps in series
  Adding pumps in series allows to build higher pressure (see Fig. 3.2). In order to avoid voltage accumulation, the electrical field is reversed in specific wide parts of the pump where EO flow is less important than in the narrow parts (see Ref. [18]).

3.2.3 AC micropumps design

EO pumps are usually based on DC currents. However, such designs usually needs high voltage to give significant flows. As mentioned in Chap. 2, high voltage may generate undesirable chemical reactions on the electrodes and they are not easy to implement in miniaturized and/or portable devices. AC current designs should be able to overcome this inconvenience. We will present in the next chapters the underlying theory for AC electroosmotic pumping. This is a very open topic of research. A lot of experimental observations are still not fully explained by theoretical models.

3.3 Experimental data for electrode-arrays

3.3.1 Symmetric electrode-array

In Ref. [17], Green studied fluid flow over symmetric electrodes. The setup used is briefly described in Fig. 3.3. The two electrodes are identical and an AC voltage is applied to them, so that the difference of potential between the two electrodes has an amplitude V_0. The fluid flow takes then the pattern of rolls across the electrodes. The velocities observed are directly related to the frequency and to the amplitude of the AC current used. Some values are given in Fig. 3.4. Complete results can be found in Ref. [17]. González *et al.* proposed a theory to explain this flow in Ref. [20]. The flow observed over the symmetric electrodes is, indeed, symmetric. Thus, it does not give rise to a pumping velocity. Yet, we will show in Chap. 4 that a full understanding of the electro-hydrodynamics of the symmetric electrode-array is an essential step towards a complete model for the electrode-array pump.

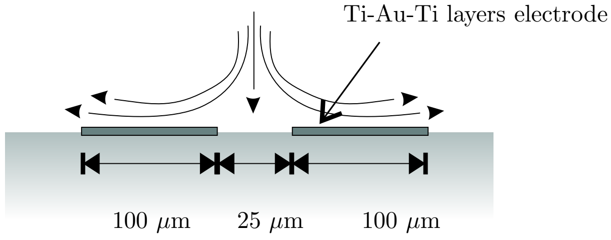

Figure 3.3: Experimental setup for symmetric electrode-array used by Green [17]. The electrolyte is a dilute aqueous solution of KCl. On the electrodes a AC voltage is applied, with the frequency up to 100 kHz and the voltage $V_0 < 5$ V. The velocities are measured by μPIV. The fluid flow observed gives velocities up to 500 μm.s^{-1} over the electrodes.

3.3.2 AC electrode-array pump

In [6], Ajdari proposed to introduce asymmetry in the system in order to obtain a directional net flow. In Ref. [1] and Ref. [2], Brown and Mpholo have conducted various experiments using asymmetric electrodes array. The setup used is given in Fig. 3.5. In this setup, the asymmetry is introduced by taking a wide electrode and a narrow electrode. It is possible to introduce asymmetry by other means, such as modifying the height of electrodes or the capacitance of the electrode. Yet, from a practical point of view, the most convenient way is to use a wide and narrow electrode cell. The main results of this work was to prove that the asymmetric electrode-array design is able to generate a net directional fluid motion in the channel. Some results are given in Fig. 3.6.

Beside those first results, Studer and Ajdari have shown, using a similar setup as Brown's, that it is possible to reverse the fluid flow for given frequencies (see Ref. [21] and Fig. 3.7). This is a highly interesting feature for a microfluidic device, since it means that this design is probably able to generate pumping in two directions. This topic will be discussed in Chap. 5.

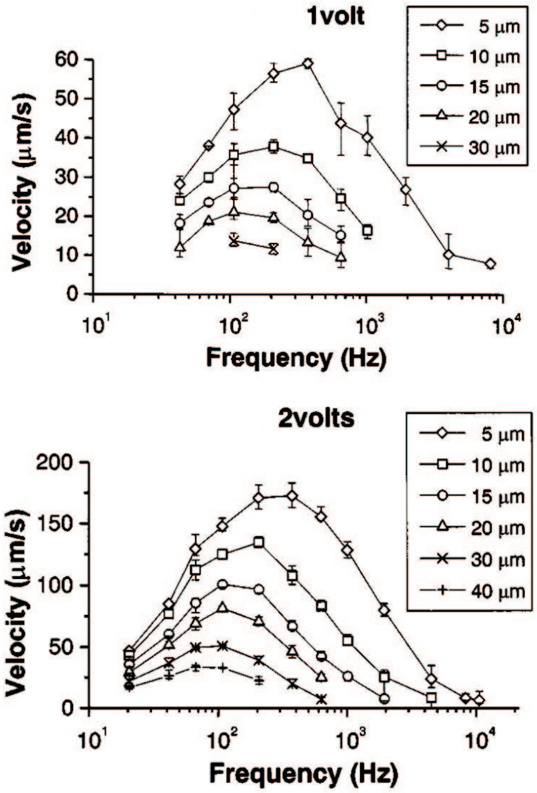

Figure 3.4: Experimental results from Ref. [17] for the symmetric electrode-array. As voltage is increased, the velocities are increased. The frequency dependence shows a peak for a given frequency between 10^2 Hz and 10^3 Hz. This position of the peak varies with the dilution of the electrolyte and with the applied voltage. With higher concentrations, this peak is displaced towards higher frequencies.

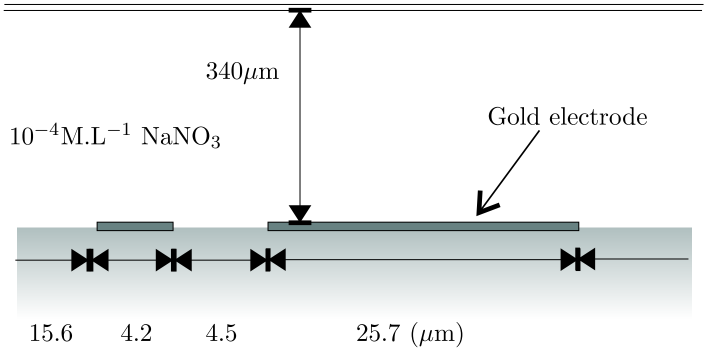

Figure 3.5: Experimental setup for asymmetric electrodes arrays used by Brown [1]. The spatial period of the electrode cell is 50μm. On the electrodes a voltage is applied so that the difference of potential between the two electrodes V_0 is smaller than 1.4 V. The velocities are measured by μPIV.

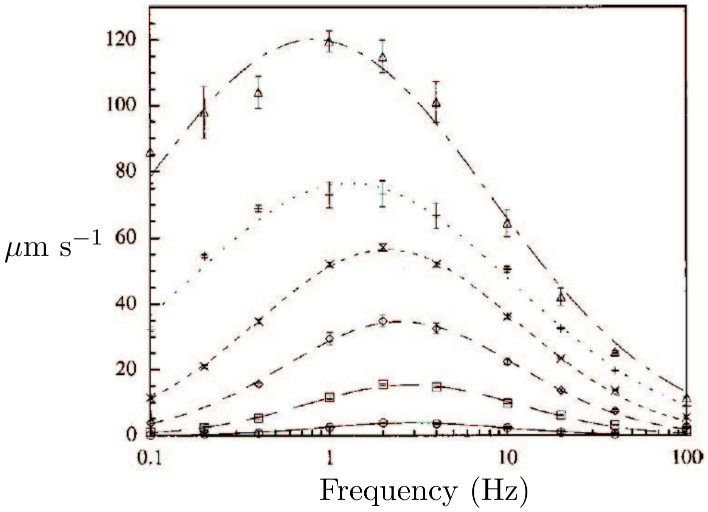

Figure 3.6: Experimental results for the asymmetric electrode-array. The plot shows pumping velocities over the electrodes against the applied frequency at six different values of the applied voltage : 0.2 0.4 0.6 0.8 1.0 and 1.2 V_{rms}. For higher voltage, the resonance frequency is lowered. (Brown, [1])

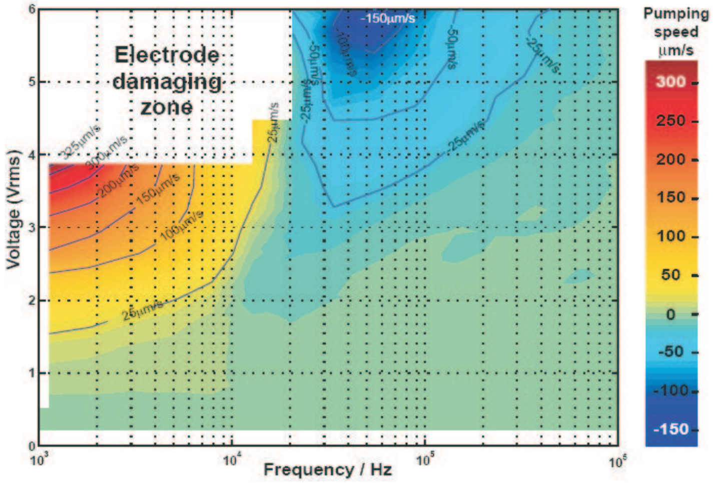

Figure 3.7: Plot of pumping speed for a given domain of voltage and frequency. Notice the change of the flow direction for $f \simeq 2 \times 10^4$ Hz. (Studer, [21])

Chapter 4

Electrolytes driven by modulated surface potentials

4.1 Introduction

This chapter is directly taken from the article [10] submitted to Phys. Rev E. We revisit the problem studied by Ajdari [6] where an electrolyte is perturbed by an AC-driven spatially modulated surface potential. However, instead of modelling the surface as well as the Debye layer by simple capacitors as Ajdari did, we develop a full non-equilibrium description of the electro-hydrodynamics. This allows us to study the full dynamics of ion concentrations, electrical potentials, velocity fields, pressure fields, and electrical currents. The study of this symmetric case is necessary to understand the dynamics of the asymmetric electrode-array.

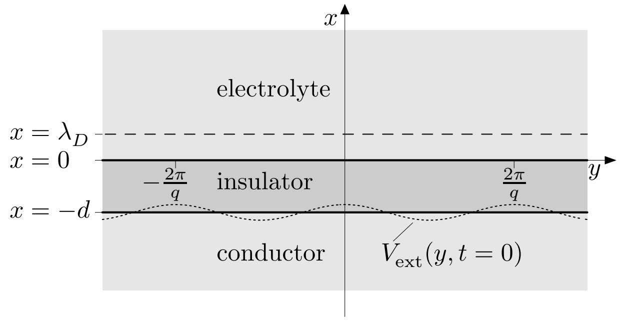

Figure 4.1: A sketch of the system under study. The bi-ionic electrolyte is situated in the half space $x > 0$. Below it, for $-d < x < 0$, is a planar wall consisting of an insulating dielectric slab of thickness d and below that, for $x < -d$, is a semi-infinite conductor.

In the following we consider a bi-ionic electrolyte, *i.e.*, an aqueous solution of a salt containing a positive and a negative type of ions with charges $+Ze$ and $-Ze$, respectively, where Z is the valence and e the elementary charge. In terms of Cartesian coordinates (x, y, z) the electrolyte is confined to the semi-infinite space $x > 0$ by an impenetrable, homogeneous and planar insulating layer with dielectric constant ϵ_s placed at $-d < x < 0$, see Fig. 4.1. This layer models either a Stern layer or an oxide layer. In the case of a modelling of the Stern layer, we have $d \simeq \lambda_{mol}$. If the insulator layer models an oxide layer, then d can take values up to a few nanometers. The insulating layer is bounded by a conductor at $x < -d$ which has been biased at the surface $x = -d$ by a spatially modulated, external AC potential $V_{\text{ext}}(y, t)$.

$$V_{\text{ext}}(y,t) = V_0 \cos(qy) e^{i\omega t}, \tag{4.1}$$

where V_0 is the amplitude, q the wavenumber of the spatial modulation, and ω the driving angular frequency.

There is complete translation invariance along the z axis, so the z coordinate drops out of our analysis, and all positions $\mathbf{r} = (x, y)$ are therefore just refereing to the xy plane.

4.2 Non-equilibrium description

4.2.1 The insulating layer, $-d < x < 0$

The insulating layer contains neither free space charge nor free currents so the electrical potential $\phi(\mathbf{r}, t)$ is governed by the Laplace equation,

$$\boldsymbol{\nabla}^2 \phi(\mathbf{r}, t) = 0, \quad \text{for } -d < x < 0. \tag{4.2}$$

4.2.2 The electrolyte, $x > 0$

In the liquid electrolyte we consider the ionic densities $n^{\pm}(\mathbf{r}, t)$, the potential $\phi(\mathbf{r}, t)$, the ionic current densities (the ionic flux densities) $\mathbf{i}^{\pm}(\mathbf{r}, t)$, the velocity field $\mathbf{v}(\mathbf{r}, t)$ of the electrolyte, and the pressure field $p(\mathbf{r}, t)$.

The number densities of the ions couple to the potential via Poisson equation,

$$\boldsymbol{\nabla}^2 \phi(\mathbf{r}, t) = -\frac{Ze}{\epsilon}\big[n^{+}(\mathbf{r}, t) - n^{-}(\mathbf{r}, t)\big]. \tag{4.3a}$$

The ionic current densities are coupled to the ionic densities by a continuity equation, which in the absence of any chemical reactions in the system is

$$\partial_t n^{\pm}(\mathbf{r}, t) = -\boldsymbol{\nabla} \cdot \mathbf{i}^{\pm}(\mathbf{r}, t). \tag{4.3b}$$

The presence of convection or of gradients in the densities $n^{\pm}(\mathbf{r}, t)$ and the electric potential $\phi(\mathbf{r}, t)$ will generate ionic current densities $\mathbf{i}^{\pm}(\mathbf{r}, t)$. These currents are given by the Nernst–Planck equation

$$\mathbf{i}^{\pm}(\mathbf{r}, t) = -D\boldsymbol{\nabla} n^{\pm}(\mathbf{r}, t) + n^{\pm}(\mathbf{r}, t)\mathbf{v}(\mathbf{r}, t) \mp \mu n^{\pm}(\mathbf{r}, t)\boldsymbol{\nabla}\phi(\mathbf{r}, t),$$

where, for simplicity, we have assumed that the two types of ions have the same diffusion constant D and the same mobility μ. We remind the reader that both the diffusion constant D and the electric conductivity σ are linked to the mobility μ via the Nernst–Einstein relation $D = \frac{k_{\text{B}}T}{Ze}\,\mu$ and $\sigma^{\pm} = Zen^{\pm}\mu$.

Finally, the velocity field and pressure field of the liquid are coupled to the potential and ionic densities by the Navier–Stokes equation

$$\begin{aligned}&\rho\big[\partial_t\mathbf{v}(\mathbf{r},t)+\mathbf{v}(\mathbf{r},t)\cdot\boldsymbol{\nabla}\mathbf{v}(\mathbf{r},t)\big]= \\ &-\boldsymbol{\nabla}p(\mathbf{r},t)+\eta\boldsymbol{\nabla}^2\mathbf{v}(\mathbf{r},t)-Ze\big[n^+(\mathbf{r},t)-n^-(\mathbf{r},t)\big]\boldsymbol{\nabla}\phi(\mathbf{r},t),\end{aligned} \tag{4.3c}$$

where ρ is the mass density, η is the viscosity of the liquid, and p is the pressure. Furthermore, treating the electrolyte as an incompressible fluid we have

$$\boldsymbol{\nabla}\cdot\mathbf{v}(\mathbf{r},t)=0. \tag{4.3d}$$

The five coupled equations, Eqs. (4.3a) to (4.3d), fully govern the five physical quantities $n^{\pm}$, ϕ, $\mathbf{i}^{\pm}$, $\mathbf{v}$, and p.

4.2.3 Boundary conditions

We consider a vanishing zeta-potential (*i.e.*, no un-passivated surface charges on the insulator-electrolyte interface). The non-vanishing zeta-potential case has been studied in Chap. A and did not lead to the desired effects. Assuming a zero zeta-potential, the boundary condition for the electric potential is then

$$\phi(\mathbf{r},t)\big|_{x=-d}=V_{\mathrm{ext}}(y,t), \tag{4.4a}$$

$$\phi(\mathbf{r},t)\big|_{x=\infty}=0. \tag{4.4b}$$

At the interface between the electrolyte and the insulating region the normal component of the ionic current density vanishes,

$$0=\partial_x n^{\pm}(\mathbf{r},t)\big|_{x=0}\pm\frac{Ze}{k_BT}n^{\pm}(\mathbf{r},t)\partial_x\phi(\mathbf{r},t)\big|_{x=0}. \tag{4.5}$$

Here, we have utilized Eq. (4.3c) and the absence of convection at the interface due to the no-slip boundary condition,

$$\mathbf{v}(\mathbf{r},t)\big|_{x=0}=\mathbf{0}. \tag{4.6}$$

For the ionic densities we have

$$n^{\pm}(\mathbf{r},t)\big|_{x=\infty}=n_{\infty}, \tag{4.7}$$

where n_{∞} is the homogeneous density of either of the two types of ions in the absence of an external perturbation, *i.e.*, when $V_0=0$. For the pressure, we assume that we have no externally applied pressure gradients so that p is the internal pressure caused by fluid flow and the electrical forces on the ions.

4.3 Static regime, $\omega = 0$

In the static regime we have equilibrium and neither current nor fluid flow, *i.e.*, $\mathbf{i}^{\pm} = \mathbf{0}$ and $\mathbf{v} = \mathbf{0}$. The pressure gradient balances the electrical forces on the charges. The governing equations for ϕ and $n^{\pm}$ of course reduce to those of electro-statics.

In the insulating layer $\phi(\mathbf{r})$ follows from Eqs. (4.2) and (4.4a),

$$\phi(\mathbf{r}) = \left[C_1 e^{-qx} + C_2 e^{qx}\right] \cos(qy), \quad \text{for } -d < x < 0, \tag{4.8}$$

where $C_{1,2}$ are integration constants.

In the electrolyte $\phi(\mathbf{r})$ is governed by the Poisson–Boltzmann equation which in the Debye–Hückel approximation $ZeV_0 \ll k_B T$ becomes (see, *e.g.*, Sec. 4.4.1 below or Ref. [22])

$$\boldsymbol{\nabla}^2 \phi(\mathbf{r}) = \lambda_D^{-2} \phi(\mathbf{r}). \tag{4.9}$$

Here, we have introduced the Debye screening length λ_D as

$$\lambda_D \equiv \sqrt{\frac{\epsilon k_{\mathrm{B}} T}{2Z^2 e^2 n_\infty}}. \tag{4.10}$$

The space charge follows from Poisson equation, Eq. (4.3a). From a straightforward solution for ϕ and $Ze(n^+ - n^-)$ we arrive at the following expression relating the total potential drop across the system and accumulated charge in the electrolyte,

$$\phi(\infty, y) - \phi(-d, y) \equiv \frac{1}{C_{\text{eff}}} \int_0^\infty dx Ze[n^+(\mathbf{r}) - n^-(\mathbf{r})]. \tag{4.11a}$$

The coefficient,

$$C_{\text{eff}}^{-1} = \left[1 + (q\lambda_D)^2\right] \frac{\sinh(qd)}{qd}\, C_s^{-1} + \sqrt{1 + (q\lambda_D)^2}\, \cosh(qd)\, C_D^{-1}, \tag{4.11b}$$

is identified as the inverse of an effective series capacitance. The constant C_s is the intrinsic surface capacitance and C_D the capacitance of the Debye layer given by

$$C_s \equiv \frac{\epsilon_s}{d}, \tag{4.11c}$$

$$C_D \equiv \frac{\epsilon}{\lambda_D}. \tag{4.11d}$$

In Ref. [6] the potential in the bulk of the electrolyte ($x \gg \lambda_D$) is governed by the Laplace equation which is coupled to the external potential V_{ext} by an effective capacitance $C_{\text{eff}} = \left(C_s^{-1} + C_D^{-1}\right)^{-1}$. As shown above this approach is valid up to second order in the small parameters $q\lambda_D \ll 1$ and $qd \ll 1$.

4.4 Dynamic regime, $\omega > 0$

We now solve Eqs. (4.3) in the dynamic regime, $\omega > 0$. First the ionic current densities are eliminated by inserting Eq. (4.3c) into Eq. (A.5). Using the incompressibility of the fluid, Eq. (4.3d), we get the continuity equation

$$\partial_t n^{\pm}(\mathbf{r}, t) = D\, \boldsymbol{\nabla}^2 n^{\pm}(\mathbf{r}, t) - [\boldsymbol{\nabla} n^{\pm}(\mathbf{r}, t)] \cdot \mathbf{v}(\mathbf{r}, t) \pm \mu \boldsymbol{\nabla} \cdot \left[n^{\pm}(\mathbf{r}, t)\, \boldsymbol{\nabla}\phi(\mathbf{r}, t)\right]. \tag{4.12}$$

4.4.1 Debye–Hückel approximation

To advance further by analytical methods, we now linearize the continuity equation, Eq. (A.14), in the density as follows. We assume $n^{\pm}(\mathbf{r},t)\big|_{x=\infty} \equiv n_{\infty}$ and write

$$n^{\pm}(\mathbf{r},t) = n_{\infty} + \delta n^{\pm}(\mathbf{r},t), \qquad \lim_{x\to\infty} \delta n^{\pm}(\mathbf{r},t) = 0. \tag{4.13}$$

It is a non-zero V_0 that spawns $\delta n^{\pm} \neq 0$, and when the applied voltage V_0 is much smaller than the thermal voltage V_T, defined by

$$V_T \equiv k_{\mathrm{B}}T/Ze, \tag{4.14}$$

we have $|\delta n_0^{\pm}| \ll n_{\infty}$. In this limit the so-called Debye–Hückel approximation is valid, and $n^{\pm}(\mathbf{r},t)\, \boldsymbol{\nabla}\phi(\mathbf{r},t)$ is substituted by $n_{\infty}\, \boldsymbol{\nabla}\phi(\mathbf{r},t)$ in Eq. (A.14). We subsequently use Eq. (4.3a) to replace $\boldsymbol{\nabla}^2\phi(\mathbf{r},t)$ with $-\nu(\mathbf{r},t)/\epsilon$ where

$$\nu(\mathbf{r},t) \equiv n^{+}(\mathbf{r},t) - n^{-}(\mathbf{r},t) = \delta n^{+}(\mathbf{r},t) - \delta n^{-}(\mathbf{r},t). \tag{4.15}$$

Finally, we form the difference of the "±"-versions of Eq. (A.14) and obtain the partial differential equation

$$\partial_t \nu(\mathbf{r},t) = \left[D\boldsymbol{\nabla}^2 - D\frac{1}{\lambda_D^2} - \mathbf{v}(\mathbf{r},t)\cdot\boldsymbol{\nabla} \right] \nu(\mathbf{r},t). \tag{4.16}$$

4.4.2 Diffusive regime

From our study of the static regime we know that the net charge density is non-zero only in the Debye layer, $x \lesssim \lambda_D$. In this region the velocity will be vanishing because of the no-slip boundary condition. Thus, diffusion will dominate so that convection can be neglected, and the electro- and hydro-dynamic problems decouple. Since the density difference ν changes over the length scales λ_D and q^{-1} for the x and y directions, respectively, the condition for the decoupling is $|v_x|/\lambda_D + |v_y| q \ll Dq^2$ for $0 < x \lesssim \lambda_D$. In this limit Eq. (4.16) has a general $\cos(qy)e^{i\omega t}$ modulated decaying solution of the form

$$\nu(\mathbf{r},t) = C_1 e^{-\kappa x}\cos(qy)e^{i\omega t}\ ,\ x > 0, \tag{4.17a}$$

where the decay parameter κ depends on the Debye frequency ω_D,

$$\kappa \equiv \frac{1}{\lambda_D}\sqrt{1 + (q\lambda_D)^2 + i\,\frac{\omega}{\omega_D}}, \tag{4.17b}$$

$$\omega_D \equiv \frac{D}{\lambda_D^2}. \tag{4.17c}$$

For the potential we seek a solution of a form similar to Eq. (4.17a), $\phi \propto \cos(qy)e^{i\omega t}$, and substituting this together with Eq. (4.17a) into Eq. (4.3a) yields

$$(\partial_x^2 - q^2)\phi(\mathbf{r},t) = -\frac{Ze}{\epsilon} C_1 e^{-\kappa x}\cos(qy)e^{i\omega t}. \tag{4.18}$$

Demanding $\phi(\mathbf{r},t)\big|_{x=\infty} = 0$ the solution is

$$\phi(\mathbf{r},t) = \Big[C_1 \frac{Ze}{\epsilon}(q^2-\kappa^2)^{-1}e^{-\kappa x} + C_2 e^{-qx}\Big] \times \cos(qy)e^{i\omega t}, \quad x > 0. \tag{4.19}$$

In the insulating layer we have the following $\cos(qy)e^{i\omega t}$ modulated general solution to Eq. (4.2),

$$\phi(\mathbf{r},t) = \Big[C_3 e^{-qx} + C_4 e^{qx}\Big] \cos(qy)e^{i\omega t} \;,\; -d < x < 0. \tag{4.20}$$

In order to determine C_n $(n = 1, 2, 3, 4)$ we first consider the boundary condition for the current. Applying the Debye–Hückel approximation to the second term in Eq. (4.5) and forming the difference of the "±" solutions we arrive at

$$0 = \partial_x \Big[\nu(\mathbf{r},t) + \frac{C_D}{Ze\lambda_D}\phi(\mathbf{r},t)\Big]\Big|_{x=0}. \tag{4.21}$$

Together with the boundary condition for ϕ at $x = -d$ as well as the continuity of ϕ and $\epsilon\partial_x\phi$ at $x = 0$ we may determine the constants straightforwardly.

4.4.3 Long-period and low-frequency modulation

Next, we consider the regime where the spatial period of the modulation is much longer than all other length scales, *i.e.*, $q\lambda_D \ll 1$ and $qd \ll 1$. We also assume that $\omega \ll \omega_D$ so that $\kappa \simeq 1/\lambda_D$. In this limit we get

$$\nu(\mathbf{r},t) = -\frac{q\sigma_\infty V_0}{Ze\lambda_D}\frac{1}{\omega^* + i\omega}e^{-x/\lambda_D}\cos(qy)e^{i\omega t} + \mathcal{O}([q\lambda_D]^2), \tag{4.22}$$

and

$$\phi(\mathbf{r},t) = V_0 \frac{i\omega}{\omega^* + i\omega}e^{-qx}\cos(qy)e^{i\omega t} + \mathcal{O}(q\lambda_D), \tag{4.23}$$

where we have used the notation of Ajdari [6]

$$\text{resonance frequency:} \quad \omega^* = q\lambda_D(1+\delta)\,\omega_D, \tag{4.24a}$$
$$\text{conductivity:} \quad \sigma_\infty = [\sigma^+ + \sigma^-]\big|_\infty = \epsilon\omega_D, \tag{4.24b}$$
$$\text{capacitance ratio:} \quad \delta = \frac{C_D}{C_s}. \tag{4.24c}$$

These results are equivalent to those in Ref. [6] if we similarly to Eq. (4.11a) introduce the Debye layer surface charge $\sigma_D(y) = Ze\int_0^\infty dx\,\nu(x,y)$.

4.4.4 Body-force

Until this point we have used the exponential notation for the temporal dependence. However, since the body-force is essentially non-linear in the electrical potential/density

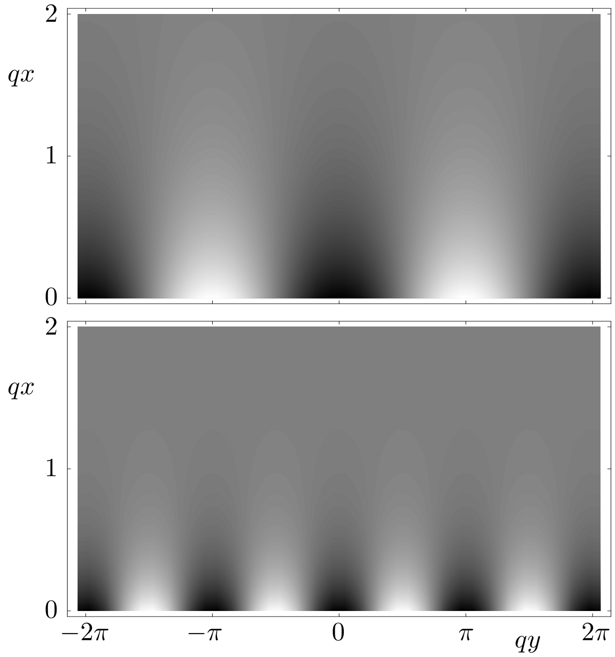

Figure 4.2: Top and bottom panels are gray scale plots of the amplitudes of the potential $\phi(\mathbf{r},t)$ [see Eq. (4.23)] and of the pressure $p(\mathbf{r},t)$ [see Eq. (4.32)] as a function of qx and qy. Notice the period doubling in the pressure field compared to the electric potential.

[see last term in Eq. (2.4)] we have to take the real part to get the body-force, *i.e.*, $\mathbf{F} = -Ze\nu\boldsymbol{\nabla}\phi = -Ze\mathrm{Re}\{\nu\}\mathrm{Re}\{\boldsymbol{\nabla}\phi\}$ so that we get

$$\begin{aligned}\mathbf{F}(\mathbf{r},t) = \frac{\eta v_1}{\lambda_D^2}\,\frac{\cos(2\omega t+\varphi)}{\frac{\omega}{\omega^*}+\frac{\omega^*}{\omega}}\,e^{-x/\lambda_D}&\\ \times\left[2\cos^2(qy)\mathbf{e}_x+\sin(2qy)\mathbf{e}_y\right]+\mathcal{O}\big([q\lambda_D]^2\big)&\end{aligned} \tag{4.25a}$$

where we following Ref. [6] have introduced

$$v_1 \equiv \frac{q\epsilon V_0^2}{4\eta(1+\delta)} \tag{4.25b}$$

and the frequency dependent phase shift

$$\varphi = -\arctan\left(\frac{\omega}{2\omega^*}-\frac{\omega^*}{2\omega}\right). \tag{4.25c}$$

In the derivation of Eq. (4.25a) we have used that

$$\mathrm{Re}\bigg\{\frac{e^{i\omega t}}{i\omega+\omega^*}\bigg\}\mathrm{Re}\bigg\{\frac{i\omega e^{i\omega t}}{i\omega+\omega^*}\bigg\} = \frac{-1}{2\omega^*}\frac{\cos(2\omega t+\varphi)}{\frac{\omega}{\omega^*}+\frac{\omega^*}{\omega}}. \tag{4.26}$$

At low frequencies, $\mathbf{F} \propto \omega$, it becomes maximal at the resonance frequency ω^*, and then it falls off again at higher frequencies. We note that $\lim_{\omega\to 0}\mathbf{F} = \mathcal{O}\big([q\lambda_D]^2\big)$, but this small force will just be balanced by a pressure gradient so that $\lim_{\omega\to 0}\mathbf{v} = \mathbf{0}$ and $\lim_{\omega\to 0}\mathbf{i}^{\pm} = \mathbf{0}$.

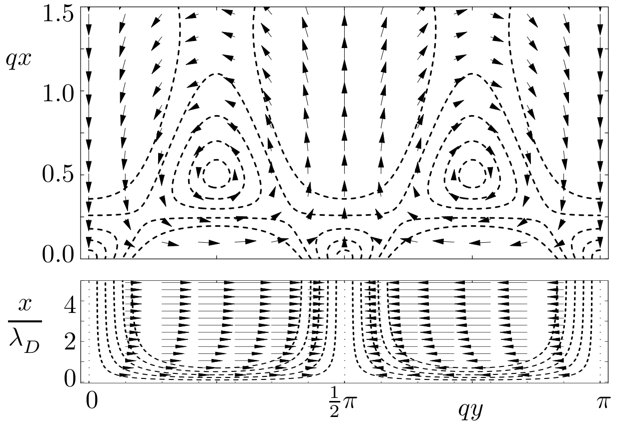

Figure 4.3: Vector-plots of the vector-amplitude of the velocity-field $\mathbf{v}(\mathbf{r},t)$ in the bulk [top panel] given by Eq. (4.31) and in the Debye layer [bottom panel] given by Eq. (4.28). The flow pattern contains rolls (with a temporal harmonic motion), which are indicated by contours of constant velocity (dashed lines).

4.4.5 Linearized flow in quasi-steady state

In order to solve the Navier–Stokes equation, Eq. (2.4), we note that for a body-force of small magnitude and with slow temporal variation the fluid response is linear and the flow will approximately be at steady state at each moment in time. We begin by comparing the inertial terms on the left-hand side (LHS) with the viscous term (second term) on the right-hand side (RHS). The body force has a characteristic frequency ω and two characteristic length scales λ_D and q^{-1} for the x and y-directions, respectively. Since ∂_t essentially gives a factor of ω, and $\boldsymbol{\nabla}$ essentially gives $\lambda_D^{-1}\mathbf{e}_x + q\mathbf{e}_y$, we can show that the viscous term dominates over the LHS when $\omega \ll \omega_c \equiv \frac{\eta}{\rho D}\,\omega_D$. This condition is easily fulfilled when $\omega \ll \omega_D$, since typically $\frac{\eta}{\rho D} \gg 1$, and Eq. (2.4) then becomes

$$\mathbf{0} \simeq -\boldsymbol{\nabla} p(\mathbf{r},t) + \eta\boldsymbol{\nabla}^2\mathbf{v}(\mathbf{r},t) + \mathbf{F}(\mathbf{r},t). \tag{4.27}$$

This is the resulting quasi-steady flow problem which is linear in the velocity field.

4.4.6 Debye layer flow

In order to solve Eqs. (4.3d) and (4.27) we study the flow over a λ_D-scale at the boundary first and then a q^{-1}-scale. For this boundary layer approach, we assume that for $x \lesssim \lambda_D$, we have $v_x \sim 0$. Solving for the pressure and substituting into the y-component of Eq. (4.27) we get

$$v_y(\mathbf{r},t) = v_s(y,t)\left(1 - e^{-x/\lambda_D}\right) + \mathcal{O}(q\lambda_D),\ x \lesssim \lambda_D \tag{4.28}$$

where the prefactor

$$v_s(y,t) \equiv v_1\,\frac{\cos(2\,\omega\,t + \varphi)}{\frac{\omega}{\omega^*} + \frac{\omega^*}{\omega}}\,\sin(2\,q\,y), \tag{4.29}$$

in the limit $1/q \gg x \gtrsim \lambda_D$ can be interpreted as a slip-velocity at the wall acting as a conveyor belt for the bulk fluid (see bottom panel of Fig. 4.3).

4.4.7 Bulk flow

For $x \gtrsim \lambda_D$ we have that $\mathbf{F} \simeq \mathbf{0}$ and we solve Eq. (4.27) together with Eq. (4.3d) and the boundary condition

$$\mathbf{v}(\mathbf{r},t)\big|_{x=0} = v_s(y,t)\,\mathbf{e}_y. \tag{4.30}$$

To lowest order in $q\lambda_D$ this gives

$$\begin{aligned}\mathbf{v}(\mathbf{r},t) \simeq v_1\,\frac{\cos(2\,\omega\,t+\varphi)}{\frac{\omega}{\omega^*}+\frac{\omega^*}{\omega}}\,e^{-2qx} \\ \times\Big(-2qx\cos(2qy)\mathbf{e}_x + (1-2qx)\sin(2qy)\mathbf{e}_y\Big),\end{aligned} \tag{4.31}$$

and

$$p(\mathbf{r},t) \simeq 4q\eta v_1\,\frac{\cos(2\omega t+\varphi)}{\frac{\omega}{\omega^*}+\frac{\omega^*}{\omega}}\,e^{-2qx}\cos(2qy). \tag{4.32}$$

If we now substitute into Eq. (2.4) we get RHS − LHS $\propto e^{-x/\lambda_D} + \mathcal{O}(\omega/\omega_D) + \mathcal{O}([q\lambda_D]^2)$ which shows that Eqs. (4.31) and (4.32) are indeed excellent approximations to the full solution of the non-linear time-dependent Navier–Stokes equation, Eq. (2.4), for $x \gg \lambda_D$. For the incompressibility constraint, Eq. (4.3d), our solution gives $\boldsymbol{\nabla}\cdot\mathbf{v} = \mathcal{O}([q\lambda_D]^2)$. In Fig. 4.3 we show a field-plot of the velocity-field, Eq. (4.31), along with the contours for constant velocity.

4.5 Discussion

We have analyzed the full non-equilibrium electro-hydrodynamics of the Debye screening layer that arises in an aqueous bi-ionic solution near a planar wall when applying a spatially modulated ac-voltage $V_0\cos(qy)e^{i\omega t}$, Eq. (4.1). Our analysis applies to the low-frequency Debye–Hückel regime where the amplitude V_0 of the external potential is lower than the thermal voltage V_T and the driving frequency ω is lower than the inverse response-time of the electrolyte $\omega_D = \sigma_\infty/\epsilon$ (see Secs. 4.4.1 and 4.4.3). Furthermore, we have limited ourselves to the diffusive regime where convection can be neglected corresponding to a sufficiently low driving amplitude, $V_0 \ll V_c$ where

$$V_c \equiv \sqrt{(1+\delta)\eta D/\epsilon} \tag{4.33}$$

is a critical voltage [see first paragraph of Sec. 4.4.2, $\mathbf{v} \sim v_1\mathbf{e}_y$ in the Debye layer]. We have also considered the low-frequency regime $\omega \ll \omega_c$ where viscosity dominates over inertia (see Sec. 4.4.5). Finally, we have considered the limit with the spatial modulation being much longer than all other length scales in the problem, i.e. $qd \ll 1$ and $q\lambda_D \ll 1$ (see Sec. 4.4.3). In summary this means that we have studied the effect of Eq. (4.1) in the limits

$$q \ll \min\big\{d^{-1},\,\lambda_D^{-1}\big\}, \tag{4.34a}$$

$$\omega \ll \min\big\{\omega_D,\,\omega_c\big\}, \tag{4.34b}$$

$$V_0 \ll \min\big\{V_T,\,V_c\big\}. \tag{4.34c}$$

Table 4.1: Typical values of central parameters.

Spatial modulation	q^{-1}	10^{-5} m
Insulator thickness	d	10^{-8} m
Debye screening length	λ_D	10^{-8} m
Resonance frequency	ω^*	10^6 s^{-1}
Debye frequency	$\omega_D = \sigma_\infty/\epsilon$	10^7 s^{-1}
Critical frequency	$\omega_c = (\eta/\rho D)\sigma_\infty/\epsilon$	10^{10} s^{-1}
Thermal voltage	$V_T = k_B T/Ze$	25 mV
Critical voltage	$V_c = \sqrt{(1+\delta)\eta D/\epsilon}$	100 mV
Ionic density	n_∞	1 mol L^{-1}
Viscosity	η	10^{-3} Pa s
Mass density	ρ	10^3 kg m^{-3}
Ionic diffusion constant	D	10^{-9} m^2 s^{-1}
Capacitance ratio	$\delta = C_D/C_s$	10

Typical values of our parameters are listed in Table 4.1.

Using first order perturbation theory we have obtained analytic solutions for the pressure and velocity field of the electrolyte and for the electric potential. The solutions have been obtained both in the narrow Debye layer on the length scale λ_D and in the bulk on the larger length scale $1/q$ set by the period of the applied external potential. As a main result we have supplied a proof for the validity of the phenomenological capacitor model.

The full dynamics seems however not to be captured by the capacitor model. Taking the time-average in Eqs. (4.25a) and (4.31) we get $\langle \mathbf{F} \rangle_t = \mathbf{0}$ and $\langle \mathbf{v} \rangle_t = \mathbf{0}$ (in full agreement with the discussion in Ref. [6]). In contrast, we obtain $\langle \mathbf{F} \rangle_t \neq \mathbf{0}$ if we begin from Eqs. (4.17a) and (4.19) without expanding in ω/ω_D and $q\lambda_D$ (the result is finite even in the zero-frequency limit). Somewhat similar results were reported in another non-equilibrium study [20], though for a different geometry. Naively, this observation could suggest that $\langle \mathbf{v} \rangle_t \neq \mathbf{0}$ contrary to the statement in Ref. [6]. However, by also averaging over the y-direction we get $\langle F_y \rangle_{t,y} = 0$ suggesting that $\langle v_y \rangle_{t,y} = 0$ in agrement with the symmetry arguments emphasized in Ref. [6]. If the finite $\langle \mathbf{F} \rangle_t$ does not give the fluid a directional flow globally, we might speculate that, at high frequencies, it makes the fluid circulate in non-oscillating vortices (with a spatial pattern like in Fig. 4.3) whereas the fluid is at rest at zero-frequency – despite $\langle \mathbf{F} \rangle_t$ being finite. The solution to this apparent contradiction lies in the pressure which will compensate the body-force at low frequencies. This has not been pointed out previously in the literature. We can explicitly show that the time-averaged body-force $\langle \mathbf{F}(\mathbf{r},t) \rangle_t$ can be written as a gradient of a potential $p_F(\mathbf{r})$:

$$\langle \mathbf{F}(\mathbf{r},t) \rangle_t = \nabla p_F(\mathbf{r}) + \mathcal{O}\big([\omega/\omega_D]^2\big) \tag{4.35}$$

where

$$p_F(\mathbf{r}) = p_0 + \frac{\frac{1}{4}\epsilon q^2 V_0^2}{\Big[q\lambda_D \cosh(qd) + \frac{\epsilon}{\epsilon_s}\sqrt{1+(q\lambda_D)^2}\,\sinh(qd)\Big]^2} \times e^{-2\sqrt{1+(q\lambda_D)^2}\,x/\lambda_D}\cos^2(qy) \tag{4.36}$$

with p_0 being a constant. Introducing the effective capacitance, Eq. (4.11b), we can also write this as

$$p_F(\mathbf{r}) = p_0 + q\eta v_1\left(1+\frac{C_D}{C_s}\right)\left(\frac{C_{\text{eff}}}{C_D}\right)^2 \frac{1+(q\lambda_D)^2}{(q\lambda_D)^2} \times e^{-2\sqrt{1+(q\lambda_D)^2}\,x/\lambda_D}\cos^2(qy). \tag{4.37}$$

The form of Eq. (4.35) suggests that

$$\big\langle \mathbf{v}(\mathbf{r},t)\big\rangle_t = \mathbf{0} + \mathcal{O}\big([\omega/\omega_D]^2\big) \tag{4.38}$$

with p_F being a pressure that compensates the low-frequency part of the body force, see Eq. (4.27). At high frequencies we expect vortices to co-exist with the harmonic fluid motion described in Eq. (4.31) whereas at low frequencies the circulation vanishes and we are left with the pure harmonic motion. Time-dependent finite element simulations confirm this picture (see Chap. 7).

4.6 Conclusion

Our results provide the theoretical underpinning of the phenomenological capacitor model widely used in the literature [6, 1, 17, 20, 5], and form a firm starting point for future studies of electro-kinetic pumps and mixers driven by spatially modulated surface potentials. The electrode-array based pumps relies on the dynamics described in this chapter (see Chap. 5). However, our non-equilibrium approach has also revealed interesting short-comings in the capacitor approach in [6] for high-frequency dynamics where vortices may appear along with the harmonic rolls also predicted by the capacitor model. Moreover, the capacitor approach is unable to describe the flow reversal observed in [21]. This matter will be discussed in Chap. 5 and in Chap. 7.

Chapter 5

Theory of an asymmetric electrode array pump

The symmetric case has been presented in Chap. 4 where we described the flow obtained for time modulated potentials. Ajdari introduces a symmetry argument to predict a directional net mean flow (e.g. a pumping effect). *Generically, if a fluid is placed in a* locally *asymmetric environment and if dissipation is induced by external means, then the fluid should be* globally *set into motion in the direction of broken symmetry, even in the absence of macroscopic gradients* [6]. In this chapter we investigate this statement in the frame of our analytical results from Chap. 4.

5.1 Asymmetric potential

5.1.1 Perturbated potential

We now introduce a perturbation in order to break the spatial symmetry of the previous electrode array defined in Chap. 4. We rewrite the excitation potential as

$$V_{\mathrm{ext}}(y,t) = V_0 \cos(q\,y)\big[1 + \beta \cos(\,2q\,y + \Psi)\big]\, e^{i\,\omega\,t}, \tag{5.1}$$

where $\beta \ll 1$. In the following we typically set the phase shift $\Psi = \frac{\pi}{2}$ to achieve maximal asymmetry. We can note that for $\Psi = 0$ the problem is symmetric.

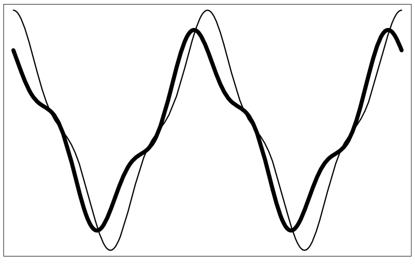

Figure 5.1: A sketch of the asymmetric potential applied on the surface. The thick line is for $\Psi = \frac{\pi}{2}$, the thin line for $\Psi = 0$ (symmetric case). For the figure, the coefficient β is taken here at 0.5.

We have chosen here to introduce only a spatial asymmetry like Brown *et al.* have done in their experiments [1]. As introduced in Chap. 3, the setup used was an array of wide and narrow electrodes, which is purely a spatial asymmetry.

In the frame of Chap. 4 we know that our equations for the electrical field ϕ and for the charge difference ν are linear. Using Eqs. (4.22) and (4.23) we have

$$\nu(\mathbf{r},t) = -\frac{q\sigma_\infty V_0}{Ze\lambda_D}\frac{1}{\omega^*+i\omega}e^{-x/\lambda_D}\cos(qy)\big[1+\beta\cos(2\,q\,y+\Psi)\big]e^{i\omega t} + \mathcal{O}\big([q\lambda_D]^2\big) + \mathcal{O}\big([\frac{\omega}{\omega_D}]^2\big), \tag{5.2}$$

$$\phi(\mathbf{r},t) = V_0\frac{i\omega}{\omega^*+i\omega}e^{-qx}\cos(qy)\big[1+\beta\cos(2\,q\,y+\Psi)\big]e^{i\omega t} + \mathcal{O}(q\lambda_D) + \mathcal{O}\big([\frac{\omega}{\omega_D}]^2\big).$$

We only consider the first order of the perturbation:

$$\mathbf{F}_1 = -Z\,e\big[\mathrm{Re}(\nu_0)\mathrm{Re}(\boldsymbol{\nabla}\,\phi_1) + \mathrm{Re}(\nu_1)\mathrm{Re}(\boldsymbol{\nabla}\,\phi_0)\big], \tag{5.3}$$

where ν_0 and ϕ_0 are the unperturbated solutions with $\beta = 0$. As for ν_1 and ϕ_1 we have

$$\nu_1(\mathbf{r},t) = -\beta\frac{q\sigma_\infty V_0}{Ze\lambda_D}\frac{1}{\omega^*+i\omega}e^{-x/\lambda_D}\cos(q\,y)\cos(2\,q\,y+\Psi)e^{i\omega t} + \mathcal{O}([q\lambda_D]^2) + \mathcal{O}\big([\frac{\omega}{\omega_D}]^2\big), \tag{5.4}$$

$$\phi_1(\mathbf{r},t) = \beta\,V_0\frac{i\omega}{\omega^*+i\omega}e^{-qx}\cos(q\,y)\cos(2\,q\,y+\Psi)e^{i\omega t} + \mathcal{O}(q\lambda_D) + \mathcal{O}\big([\frac{\omega}{\omega_D}]^2\big).$$

Since we only changed the prefactor in ν and ϕ, we can still use the following relation, seen in Chap. 4, to simplify our equation:

$$\mathrm{Re}\bigg\{\frac{e^{i\omega t}}{i\omega+\omega^*}\bigg\}\mathrm{Re}\bigg\{\frac{i\omega e^{i\omega t}}{i\omega+\omega^*}\bigg\} = \frac{-1}{2\omega^*}\frac{\cos(2\omega t+\varphi)}{\frac{\omega}{\omega^*}+\frac{\omega^*}{\omega}}. \tag{5.5}$$

If we integrate $\mathbf{F}_1$ over time, we then have

$$\big\langle\mathbf{F}(\mathbf{r},t)\big\rangle_t = \mathcal{O}(q\lambda_D) + \mathcal{O}\big([\frac{\omega}{\omega_D}]^2\big).$$

This null averaged body force — when inserted into the time averaged Navier-Stokes equation — cannot produce a mean velocity, and therefore no pumping effect. However this is true only for first order in ω (since the correction comes in as $\mathcal{O}\big([\frac{\omega}{\omega_D}]^2\big)$. As discussed in Chap. 4, for high frequencies, a mean flow pattern is expected (see Ref. [1] and [20]). Those are new facts that were not included in the original study from Ajdari [6].

5.1.2 General geometry

We can extend this result to more complex geometry, such as the Brown pump [1], by using Fourier series.

$$V(y,t) = \sum_{n=1}^{\infty}\big[a_n\cos(2\,\pi\,n\,q\,y) + b_n\sin(2\,\pi\,n\,q\,y)\big] + a_0, \tag{5.6}$$

where $V(y,t)$ is a given potential applied on the electrode. We can apply our results from Chap. 4 as long as $n\,q\,\lambda_D \ll 1$. Fig. 5.2 shows an example of a potential from a truncated Fourier series. Using analog calculations as previously, we can then show that the time averaged velocity field is 0.

Using only first order results in ω and spatial asymmetry, it is not possible to obtain any mean velocity field because the mean flow obtained lies then in higher order terms in ω. Ajdari has proposed a different approach in Ref. [6], where both spatial and temporal symmetry is broken via the capacitance of the insulating layer.

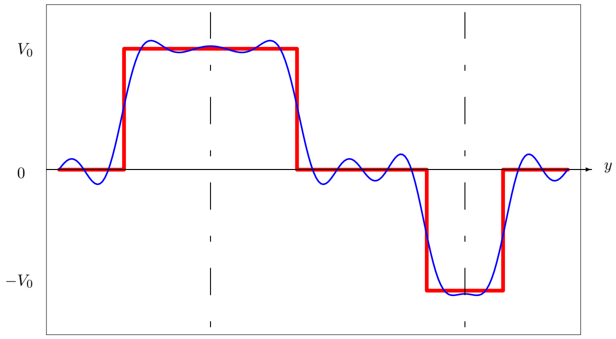

Figure 5.2: Sketch of a potential with a truncated Fourier series. The thin line is the truncated Fourier series with $n \leq 10$. The thick line is the original square potential. At first examination this setup seems to be asymmetric. However, if the sections with $V(y) = 0$ have equal lengths, we can note that we have symmetry axes in the middle of each electrode.

5.2 Asymmetric surface capacitance

5.2.1 Averaged body force

We showed that a spatial asymmetry does not give rise to a pumping effect to lowest order in ω. We wish now to introduce a spatio-temporal asymmetry. Instead of using a distorted potential, we follow Ajdari and introduce a perturbation in surface capacitance. We now rewrite the surface capacitance as follows:

$$C_s = \frac{C_D}{\delta} = \frac{\epsilon}{\lambda_D\,\delta}, \tag{5.7a}$$

$$\delta = \delta_0\big[1 + \beta\,\cos(2\,q\,y + \Psi)\big], \tag{5.7b}$$

$$\omega^* = q\lambda_D(1+\delta)\,\omega_D, \tag{5.7c}$$

where Ψ is a given phase. We choose $\beta \ll 1$ and we make a Taylor expansion to write

$$\phi = \phi_0 + \phi_1 + \mathcal{O}(\beta^2), \tag{5.8a}$$

$$\nu = \nu_0 + \nu_1 + \mathcal{O}(\beta^2), \tag{5.8b}$$

where ϕ_0 and ν_0 are the unperturbed potential and charge difference obtained in Chap. 4, Eqs. (4.23) and (4.22), respectively. We have then for ϕ_1 and ν_1 :

$$\phi_1 = -i\,q\,\lambda_D\,V_0\,\frac{\omega\,\omega_D}{(i\omega+\omega^*)^2}\,\delta_0\,\beta\cos(q\,y)\cos(2\,q\,y+\Psi)e^{-q\,x}e^{i\,t\,\omega} \tag{5.9a}$$

$$\nu_1 = q^2\,\lambda_D\,\frac{V_0\epsilon}{Ze}\,\frac{{\omega_D}^2}{(i\omega+\omega^*)^2}\,\delta_0\,\beta\cos(q\,y)\cos(2\,q\,y+\Psi)e^{-\frac{x}{\lambda_D}}\,e^{i\,t\,\omega} \tag{5.9b}$$

We remind the reader that ω^* is now a function of β, according to Eq. (5.7c). The first order component of the body force is then obtained by Eq. (5.3). After time-averaging, we have

$$\big\langle \mathbf{F}_1(\mathbf{r},t)\big\rangle_t = -\beta\,q^3\delta_0 V_0^2\,\epsilon\frac{\omega^2\,{\omega_D}^2}{(\omega^2+\omega^{*2})^2}e^{-\frac{x}{\lambda_D}}\,\cos(q\,y)^2\sin(2\,q\,y+\Psi)\,\mathbf{e}_y. \tag{5.10}$$

We may remark that the x component of the body force vanishes whereas the y component is finite. We now average over a spatial period,

$$\big\langle \mathbf{F}_1(\mathbf{r},t)\big\rangle_{t,y} = \frac{\beta}{4}\,\delta_0\,q^3\,V_0^2\,\epsilon\,\frac{\omega^2\,{\omega_D}^2}{(\omega^2+\omega^{*2})^2}\,e^{-\frac{x}{\lambda_D}}\,\sin(\Psi)\,\mathbf{e}_y. \tag{5.11}$$

This non-zero averaged body force, when inserted into the Navier–Stokes equation will give rise to non-zero velocity field.

5.2.2 Averaged bulk flow

We use the same simplification as in Chap. 4. That means that our Navier–Stokes equation is non-inertial and thus linearized. Since we know that the zeroth order gives a null velocity field, we only consider the first–order terms in β for the body force,

$$\mathbf{0} \simeq -\boldsymbol{\nabla}p(\mathbf{r},t) + \eta\boldsymbol{\nabla}^2\mathbf{v}(\mathbf{r},t) + \mathbf{F}_1(\mathbf{r},t). \tag{5.12}$$

We consider only the pumping flow, which means that we average the equations over space and time.

$$\mathbf{0} \simeq -\boldsymbol{\nabla}\big\langle p(\mathbf{r},t)\big\rangle_{t,y} + \eta\boldsymbol{\nabla}^2\mathbf{v}_{\text{pump}}(\mathbf{r},t) + \big\langle \mathbf{F}_1(\mathbf{r},t)\big\rangle_{t,y}. \tag{5.13}$$

Applying a Debye layer flow assumption as in Chap. 4, we can easily solve our problem. Using Ajdari's notation, we obtain :

$$\mathbf{v}_{\text{pump}} = v_p\sin(\Psi)\Big(\frac{\omega}{\omega^*}+\frac{\omega^*}{\omega}\Big)^{-2}\,(1-e^{-\frac{x}{\lambda_D}})\,\mathbf{e}_y\,+\mathcal{O}(q\lambda_D)+\mathcal{O}(\frac{\omega}{\omega_D})^2, \tag{5.14}$$

with

$$v_p = \beta\,q\,V_0^2\,\epsilon\,\frac{\delta_0}{4\,\eta\,(1+\delta_0)^2}, \tag{5.15}$$

and where we used

$$(q\,\lambda_D\,\omega_D)^2 \simeq \Big(\frac{\omega^*}{1+\delta_0}\Big)^2 \tag{5.16a}$$

$$\Big(\frac{\omega^*\,\omega}{\omega^2+\omega^{*2}}\Big)^2 = \Big(\frac{\omega}{\omega^*}+\frac{\omega^*}{\omega}\Big)^{-2} \tag{5.16b}$$

We note that our results are consistent with Ref. [6]. Using this asymmetric capacitance, we have shown that we can achieve a pumping effect in the first order in $\mathcal{O}(\frac{\omega}{\omega_D})$ for $\sin(\Psi) \neq 0$. If $\sin(\Psi) = 0$, we still have a mean flow [see Eq. (5.10)] in the form of a periodic rolls pattern without pumping (see Chap. 4). Using the typical parameters from Table. 4.1 and $\beta = 0.1$, we have $v_p \approx 100\,\text{nm s}^{-1}$ for $V_0 = 25$ mV. We could apply higher voltages such as $V_0 = 1$ V but then we are not anymore in the frame of the Debye–Hückel approximation (see Chap. 4, sec. 4.4.1) and our results may not be valid. Nevertheless, if we set $V_0 = 1$ V we get $v_p \approx 150\,\mu\text{m s}^{-1}$ which is comparable to the values obtained by Brown in his experiments [1].

If we try to compare the frequency where the max velocity is reached in the experiments with the analytical results, we are confronted with the problem of determining ω^*. In Chap. 4, we introduced an insulating layer to model either the Stern layer or an oxide layer. We must then define a proper thickness of the insulating layer in our model to fit the physics. Yet, this thickness is not given in the experimental data. However, in the case of a Stern layer, we have the insulator thickness $d \approx \lambda_{\text{mol}} \approx 0.3$ nm. Moreover, in our model, we assumed that the anion and the cation have the same diffusivity constant, whereas Brown used a solution of NaNO_3 at 10^{-4} mol L^{-1} in his experiments [1]. The pair Na^+, NO_3^- has different diffusivity constant for each species. We choose to set in our model the diffusivity $D = 1.5 \times 10^{-9}$ m s^{-1} which is a rough estimate taken from chemistry tables. The results are given in Table. 5.1.

The predicted resonance frequency ω^* agrees nicely with the experimental data from Ref. [1]. Brown found maximum velocities for a frequency range from 0.7 to 2.5 kHz, depending on the voltage (the resonance frequency varies with the applied voltage). Our model gives $\omega^* = 1,74$ kHz for $V_0 < 25$ mV, and for the lowest voltage given by Brown (0.2 V), the resonance is around 2 kHz. We performed the same calculations using the experimental data from Mpholo [2]. This case is similar to Ref. [1] except that the lengths of the electrode patterns are different and that Mpholo uses only voltage higher than 1 V, which is beyond the range of validity of the Debye-Hückel approximation of our analytical model. The parameters used are given in table Table. 5.1. The theoretical values do not match perfectly the experimental data but are still qualitatively relevant. The reader should keep in mind that the values given for ω^* are very sensible to any change in the input parameters.

5.3 High frequency regime

We wish now to study the high frequency domain. Interesting effects have been reported in Ref. [21] where a reversal of the fluid flow has been observed. Our results from Chap. 4 are unable to predict such flows. We suspect that the diffusivity of ions is somehow related to this, yet we simplified our expressions considering that $\omega \ll \omega_D$. Thus, we intend now to use the full solution of the electrokinetic problem defined in Sec. 4.4.2. Using software such as Mathematica, it is possible to work with those fastidious expressions.

Table 5.1: ω^* calculated for the Brown [1] and Mpholo [2] experiments

Concentration (mol m^{-3})	0.1	-	-	-
λ_D (nm)	30.5	-	-	-
Patterns length (μm)	50	25	15	10
D (m^{-2} s^{-1}) $\times 10^{-9}$	1.5	-	-	-
d (insulator thickness, nm)	0.3	-	-	-
theoretical ω^* (kHz)	1.74	2.32	3.86	5.80
ω^*_{xp} experimental resonance freq. (kHz)	0.7	1.1	1.7	2.7
$\omega^*_{\mathrm{xp}}/\omega^*$	0.40	0.47	0.44	0.46

5.3.1 Diffusive break-down, $\omega > \omega_D$

When the excitation frequency ω is comparable to ω_D, the charge distribution in the Debye layer is not anymore a simple exponential decay and the term $\kappa = 1/\lambda_D \sqrt{1 + (q\lambda_D)^2 + i\,\frac{\omega}{\omega_D}}$ does not simplify to $\kappa \simeq 1/\lambda_D$.

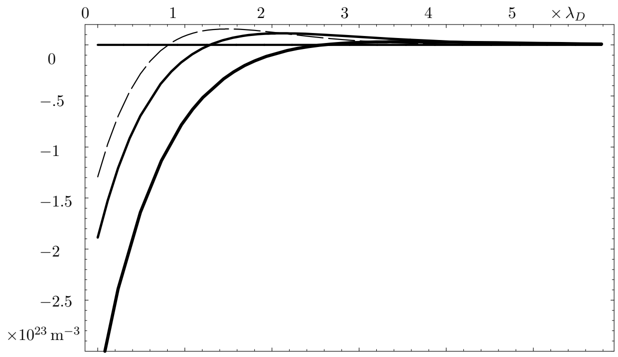

Figure 5.3: Plot of ν versus x for various frequencies, $y = 0$ and $t = 0$. The thick line is for $\omega = 0$, the thin line for $\omega = \omega_D$ and the dashed line for $\omega = 2\,\omega_D$. For low frequencies ν is a monotonous function of x. When $\omega_D \lesssim \omega$, ν has opposite signs in the Debye layer and in the bulk.

Instead of being a monotonous function of x, ν changes sign before vanishing when $x \gg \lambda_D$ (see Fig. 5.3). For $\omega \gg \omega_D$ the charge build-up is too slow to follow the oscillating driving force generated by the potential and we have then $\nu \simeq 0$.

5.3.2 Body-force balance

For $\mathbf{v} = 0$ we have a balance between the time-averaged pressure gradient and the body force such as

$$\big\langle \boldsymbol{\nabla}\, p(\mathbf{r}, t)\big\rangle_t = \big\langle \mathbf{F}(\mathbf{r}, t)\big\rangle_t. \tag{5.17}$$

Performing an integration for the x component of Eq. (5.17), we can write

$$\big\langle p\big\rangle_t = p_0 + \int \big\langle \mathbf{F}\cdot\mathbf{e}_x\big\rangle_t\, dx, \tag{5.18}$$

which upon insertion into the $\mathbf{e}_y$ component of the pressure and body force balance, leads to

$$\partial y\left[\int \left\langle \mathbf{F}\cdot\mathbf{e}_x\right\rangle_t dx\right] - \left\langle \mathbf{F}\cdot\mathbf{e}_y\right\rangle_t = 0. \tag{5.19}$$

This is true only if $\mathbf{v} = 0$. If $\mathbf{v} \neq 0$ we indeed have the Navier–Stokes equation with a non-zero term $\eta\boldsymbol{\nabla}^2\mathbf{v}$ and the balance from Eq. (5.19) becomes

$$\partial y\left[\int \left\langle \mathbf{F}\right\rangle_t\cdot\mathbf{e}_x\, dx\right] - \left\langle \mathbf{F}\right\rangle_t\cdot\mathbf{e}_y = f, \tag{5.20}$$

where f is a scalar function of r, t and ω. f is directly related to $\eta\boldsymbol{\nabla}^2\left\langle\mathbf{v}\right\rangle_t$ and thus to the fluid velocity. This balance is an indicator for the resulting fluid flow. Fig. 5.4 shows plots of f versus x. It appears that the balance is positive or negative depending on x. To be able to conclude about the effect of the balance on the Debye layer flow, we integrate it for $0 < x < \infty$.

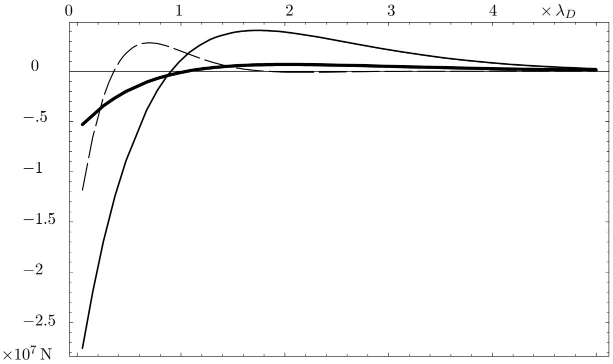

Figure 5.4: Plot of the body-force balance f versus x for $y = \pi/(4\,q)$ and $t = 0$. The thick line stands for $\omega = 0.1\,\omega_D$, the thin line for $\omega = \omega_D$ and the dashed line for $\omega = 10\,\omega_D$. f vanishes as expected for $\omega = 0$.

The results of this spatial integration are shown in Fig. 5.5, with plots of the integral $\int_0^\infty f\,dx$ against ω. It appears that the integrated value of the balance does not change sign. However, this direct integration may not be relevant because the values of the body force are huge for $x \ll \lambda_D$ and have a strong influence on the result. This is problematic since the first layers of molecules on the electrode are not likely to move because of electrical forces not described in our model. In Chap. 2 we defined the inter-molecular spacing λ_{mol} for water. The numerical value was 0.3 nm. We know that the continuum assumption made in Chap. 2 is not valid anymore for length scale smaller than λ_{mol}. Thus it is likely that our model does not describe properly the thin layer $0 < x < \lambda_{\text{mol}}$ because we did not take into account some forces. Let us write the contribution of those forces to the balance as

$$F_{\text{Stern}} = \int_0^{\lambda_{\text{mol}}} f_{\text{Stern}}\, dx. \tag{5.21}$$

Let us suppose that the first layer of molecules outside the insulating layer is immobile. This includes the domain $0 < x < \lambda_{\text{mol}}$. The balance of the forces in this layer vanishes since we have $v = 0$. This gives

$$\int_0^{\lambda_{\text{mol}}} f_{\text{Stern}}\, dx + \int_0^{\lambda_{\text{mol}}} f\, dx = 0. \tag{5.22}$$

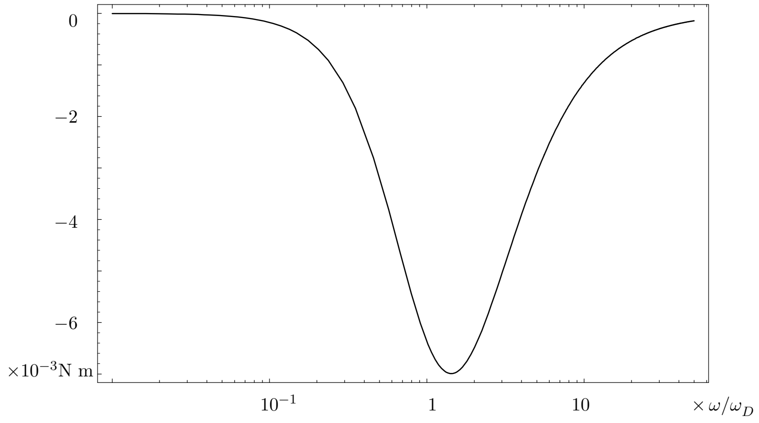

Figure 5.5: Plots of $\int_0^\infty f\,dx$ for $y = \pi/(4\,q)$ versus ω. We do not observe a change of sign for f. We can notice that the balance reaches its maximum around $\omega = \omega_D$.

Over the whole domain, we can write the integral of the body force balance as :

$$\int_0^{\lambda_{\text{mol}}} f_{\text{Stern}}\,dx + \int_0^\infty f\,dx = \int_0^{\lambda_{\text{mol}}} f\,dx + \int_{\lambda_{\text{mol}}}^\infty f\,dx + \int_0^{\lambda_{\text{mol}}} f_{\text{Stern}}\,dx, \tag{5.23}$$

which reduces to

$$\int_0^{\lambda_{\text{mol}}} f_{\text{Stern}}\,dx + \int_0^\infty f\,dx = \int_{\lambda_{\text{mol}}}^\infty f\,dx. \tag{5.24}$$

We showed that the relevant integrated body force balance to be considered is the integral $\int_{\lambda_{\text{mol}}}^\infty f\,dx$. Fig. 5.6 shows some numerical results of this integral.

Those results are highly interesting because they show a change of sign of the integrated body-force balance f around $\omega = \omega_D$. This means that, for a given frequency we have $f = 0$, which is equivalent to $\mathbf{v} = 0$. Thus we may expect a fluid flow reversal around $\omega = \omega_D$. The rolls will turn the opposite way over the electrodes. If we had introduced asymmetry in the system, our pumping velocity would revert.

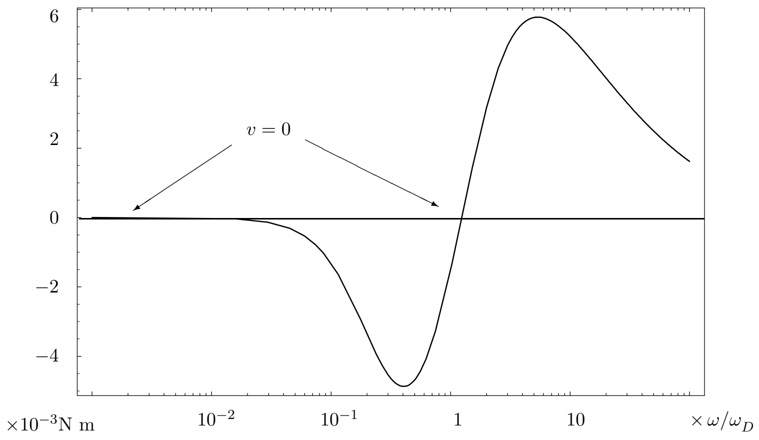

Figure 5.6: Plots of $\int_{\lambda_{\text{mol}}}^\infty f\,dx$ for $y = \pi/(4\,q)$ versus ω. f is zero around $\omega = \omega_D$, which suggests a change of direction in the fluid flow.

Table 5.2: Debye frequencies for given parameters

Concentration ($\mathrm{mol\,m^{-3}}$)	1	0.1
D (for KCl, $\mathrm{m^2\ s^{-1}}$)	$\simeq 2 \times 10^{-9}$	$\simeq 2 \times 10^{-9}$
λ_D (m)	9.64×10^{-9}	3.05×10^{-8}
ω_D ($\mathrm{s^{-1}}$)	2.15×10^{7}	2.15×10^{6}

5.3.3 Discussion

We wish now to confront this theory to the experimental data from Refs. [1], [17] and [21]. We determined the Debye frequencies for each case (see Table. 5.2). Brown and Green did not observe any reversal in fluid motion (Ref. [1] and [17]). Since they gave results for ranges of ω smaller than ω_D we can only conclude that our theory does not disagree with their data. However in the case of Ref. [21], the fluid reversal is observed at $\omega \simeq 2 \times 10^4$ and $\omega \simeq 5 \times 10^4$ for a 0.1 mol $\mathrm{m^{-3}}$ and a 1 mol $\mathrm{m^{-3}}$ KCl buffer respectively. As shown in Table. 5.2, the Debye frequency in both case are much larger so the fluid reversal happens for $\omega < \omega_D$. Yet, we can still argue that when the concentration of the electrolyte raises, the frequency at which the fluid reversal is observed raises too. We have here a qualitative agreement between the experiments and our theory, since the Debye frequency is related to the concentration via the Debye length expression Eq. (4.10). As for the quantitative comparison, it is not surprising it does not match, since our model relies on simple cosine modulation in the frame of the Debye-Hückel approximation with $V_0 < 25$ mV whereas the experimental values for V_0 are up to 10 V. Moreover, we know from the experimental data that the non-linearities arising from high voltages affects the frequency dependence of our system. The numerical results from Chap. 7 seem to confirm this picture. For example, when the applied voltage is raised, the resonance frequency is lowered (see Ref. [1]). It is possible that our comparison between the experimental frequencies and our predicted frequencies is biased because of the non-linear effects.

Chapter 6

FEMLAB, a finite element solver

The analytical work from Chap. 4 and Chap. 5 has been conducted in parallel with a numerical study. We will now briefly introduce the computational tool and the method used during this thesis. An introduction to the finite element method for microfluidic system can be found in Ref. [23]. For an exhaustive documentation on the FEM, the reader should refer to Ref. [24].

6.1 The finite element method

The finite element method (FEM) is a numerical method that can solve most partial differential equations (PDE) encountered in physical problems. This numerical method is widely used over a large area of applications, the classic one being structural mechanics. Since the finite element method is able to solve PDE problems, it is possible to solve the electrokinetics equations defined in this thesis. Even though many numerical solvers developed for the Navier–Stokes equation use the Finite Volume Method, the FEM is able to handle the fluid problem as well. Thus, this tool allows us to solve numerically our fully coupled PDE problem.

6.2 FEMLAB

FEMLAB was developed in 1999 by COMSOL (see Ref. [25]). The version 3.0a (2004) has been used for this thesis. This software is closely interfaced to Matlab for scripting and post-processing. There are thus two principal ways of working with FEMLAB: the Graphical User Interface (GUI) or the programming language in Matlab. The GUI is sufficient to deal with common problems. However, more complex modelling requires the use of the programming language. For the simulations presented in this thesis, we both used the GUI and the FEMLAB programming language.

6.2.1 Hardware

The simulations were run under windows2000 with a Pentium4 CPU at 3 GHz with 1 gigabyte of memory. We did experience some stability problem of the FEMLAB GUI that seemed to be related to video card and memory system of the computer. Typically, the simulations took between a couple of seconds up to a couple of hours to run, depending on the various parameters.

6.2.2 equations formulation

FEMLAB has different ways of representing the equations to be solved, the so-called *application modes.* Those application modes cover a wide range of physics such as heat transfer or structural mechanics. However, we only used the General PDE mode and the Navier–Stokes mode.

- General PDE formulation
  For a single variable U, FEMLAB represents the PDE system in the domain Ω with boundary $\partial\Omega$ by

$$d_a \partial_t U + \boldsymbol{\nabla} \cdot \boldsymbol{\Gamma} = F \quad \text{in } \Omega \tag{6.1a}$$

$$-\mathbf{n} \cdot \boldsymbol{\Gamma} = G + (\partial_u R)^T \mu \quad \text{on } \partial\Omega \tag{6.1b}$$

$$0 = R \quad \text{on } \partial\Omega \tag{6.1c}$$

  where the supscript T denotes the transpose. The first equation is the PDE itself. The second and third equations are the Neumann and Dirichlet boundary conditions, respectively. The terms $\boldsymbol{\Gamma}$, F, G, and R are coefficients given by the user. They can be functions of the spatial coordinates, of the solution U, or of the space derivatives of U. The coefficients F, G, R, and d_a are scalar, whereas $\boldsymbol{\Gamma}$ is the flux vector. Finally, the variable μ is the Lagrange multiplier (p. 227 in the modelling guide [25]). This way of writing the PDE suits perfectly our electrokinetics problem as we will see in Chap. 7.

- Navier–Stokes application mode
  The Navier–Stokes application mode uses the PDE general formulation to implement the momentum equation and the incompressibility constraint. The pressure term is placed in the $\boldsymbol{\Gamma}$ term of the PDE general form. This is called the full stress tensor formulation:

$$\rho\, \partial_t \mathbf{v} - \boldsymbol{\nabla} \cdot \big[p\,\mathbf{I} + \eta\big(\boldsymbol{\nabla}\mathbf{v} + (\boldsymbol{\nabla}\mathbf{v})^T\big)\big] + \rho\,\mathbf{v} \cdot \boldsymbol{\nabla}\mathbf{v} = \mathbf{F}, \tag{6.2}$$

$$\boldsymbol{\nabla}\mathbf{v} = 0, \tag{6.3}$$

  where $\mathbf{I}$ is the unit diagonal matrix. For the boundary conditions FEMLAB allows the user to choose between no-slip velocity, imposed velocity profile, symmetry or pressure constraint. It is also possible to introduce periodic boundary conditions (p.64 in the modelling guide [25]).

6.2.3 FEMLAB limitations

The use of the FEM method in a Matlab environment allows fast and simple post-processing of the results in a high level programming language. Setting up a problem and solving is fast and convenient. However, FEMLAB has some limitations.

An important limitation concerns the mesh. FEMLAB generates only unstructured grids where the aspect ratio of the elements is constant. Yet, to solve boundary layers, it is useful to have a variable aspect ratio. The unstructured mesh shown in Fig. 6.1 does not make a proper use of elements and lead to an important amount of wasted memory and computation time. This matter becomes especially problematic in the frame of this thesis since we deal with both nanometric and micrometric length scales with a full simulation of the Debye layer.

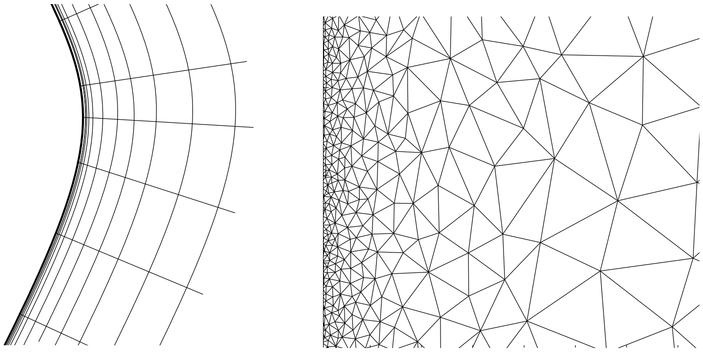

Figure 6.1: Sketch of a structured (left hand side) and unstructured mesh (right hand side) for a boundary layer. Notice the change in aspect ratio of the cells for the structured mesh.

A solution to that would be to solve the boundary layer in a different FEMLAB geometry where a high aspect ratio for the mesh is imposed. Unfortunately such a process is not very convenient because it involves coupling variables. Another solution would be to use a different mesh generator where it would be possible to apply a variable aspect ratio on the elements near the electrode.

As the geometries used in this thesis are extremely simple, we addressed this problem in yet another way. We simply generated a mesh using the Femlab mesh tool, exported it in Matlab and then applied a transformation to the nodal coordinates of the mesh in order to have a high density of elements in the Debye layer. This topic will be discussed in Chap. 7

Chapter 7

Numerical simulations

We used FEMLAB with two purposes. First, FEMLAB was used as a numerical partial differential equation solver which enabled us to investigate the problems encountered when working with the analytics. Second, it was used to simulate different cases that were not in reach of our analytical model, this comprehend three aspects: complex geometries, high frequencies and high voltages. This work should be regarded as numerical experiments. The data presented here is more qualitative than quantitative. The aim is to understand the general behavior of the electrode-array and to isolate some fundamental parameters.

7.1 Problem setup

7.1.1 Equations solved in the computational domain

In the electrolyte, we use ϕ, c^+, c^-, $\mathbf{v}$ and p as independent variable with c^+ and c^- being the molar concentrations for the positive and negative ions respectively. We use molar concentrations instead of particle densities just to handle smaller numbers, with $N_A\, c^\pm = n^\pm$. We look for a solution of the following equation system:

$$\epsilon\, \boldsymbol{\nabla}^2 \phi(\mathbf{r},t) = -F\,(c^+ - c^-), \tag{7.1a}$$

$$\partial_t c^\pm + \boldsymbol{\nabla}\big[- D\boldsymbol{\nabla} c^\pm \mp \mu\; c^\pm \boldsymbol{\nabla}\phi + c^\pm \mathbf{v}\big] = 0, \tag{7.1b}$$

$$\rho\,\partial_t \mathbf{v} - \boldsymbol{\nabla}\cdot\big[p\,\mathbf{I} + \eta\big(\boldsymbol{\nabla}\mathbf{v} + (\boldsymbol{\nabla}\mathbf{v})^T\big)\big] + \rho\,\mathbf{v}\cdot\boldsymbol{\nabla}\mathbf{v} = -F\,(\,c^+ - c^-\,)\boldsymbol{\nabla}\,\phi, \tag{7.1c}$$

where $F = N_A\, e$ is the Faraday constant. This equation system can be fit into FEMLAB using the PDE general form and the Navier–Stokes application mode. For example, for the variables $c^\pm$, we write $\boldsymbol{\Gamma} = \mathbf{i}^\pm = -D\boldsymbol{\nabla} c^\pm \mp \mu\; c^\pm \boldsymbol{\nabla}\phi + c^\pm \mathbf{v}$.

In the insulating layer, since there are no charges, the Poisson equation reduces to the Laplace equation. There is indeed no fluid in the insulator. The equation to be solved is then:

$$\boldsymbol{\nabla}\cdot\big(\epsilon_s\,\boldsymbol{\nabla}\phi(\mathbf{r},t)\big) = 0. \tag{7.2}$$

Once the problem is set up, we can run a time-dependent simulation until the system converges towards a temporal periodic solution, which usually occurs after a couple of time periods.

7.1.2 Boundary conditions

We apply the boundary conditions as described in Fig. 7.1. Some changes may occur among the different simulations. In some simulations we discarded the insulator layer to save memory. For the symmetric systems, we sometimes used the symmetric boundary conditions instead of the periodic conditions, which are then equivalent. Moreover the symmetry argument allows us to reduce the computational domain by a factor two, with $0 < y < \pi/q$ instead of $0 < y < 2\,\pi/q$.

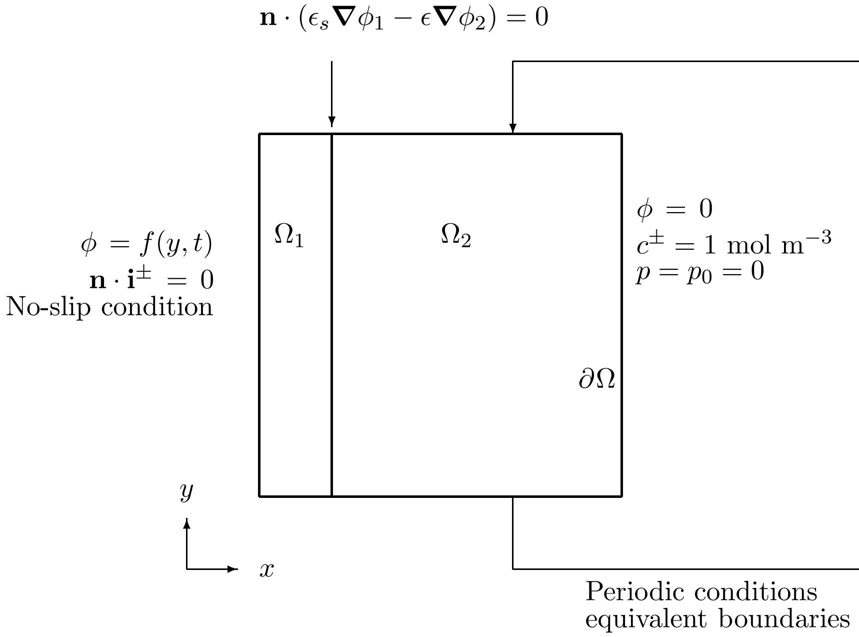
$\mathbf{n}\cdot(\epsilon_s\boldsymbol{\nabla}\phi_1 - \epsilon\boldsymbol{\nabla}\phi_2) = 0$
$\phi = f(y,t)$
$\mathbf{n}\cdot\mathbf{i}^{\pm} = 0$
No-slip condition
Ω_1
Ω_2
$\phi = 0$
$c^{\pm} = 1$ mol m^{-3}
$p = p_0 = 0$
$\partial\Omega$
y
x
Periodic conditions
equivalent boundaries

Figure 7.1: The boundary conditions applied for the simulations. The case shown is the model of Ajdari with insulator, in an open channel. The periodic boundary conditions are here equivalent to the symmetric boundary conditions.

We will now make clear what we refer to as periodic boundary conditions and symmetric boundary conditions.

- Symmetric boundary conditions
  For the symmetric case, we can consider that there is no ionic flux at the interfaces and that the symmetry plane acts as an insulator plane for the potential. We thus apply Neumann conditions for the charges and for the potential on the y boundaries.

- Periodic boundary conditions
  Periodic boundary conditions define equivalent boundaries. We choose a source boundary and a destination boundary. The considered expression and their derivatives must match. We apply this periodicity for all the independent variable. It is possible to implement more elaborate periodicity conditions, however we did not need them in our simulations.

7.2 Mesh issues

As discussed in Chap. 6, the standard mesh tool from FEMLAB impose a constant aspect ratio over the meshed geometry. To mesh the Debye layer properly, we need to have a couple elements in the x direction for $0 < x < \lambda_D$. For example, if we have $\lambda_D = 10\,\mathrm{nm}$, we should take the size of the elements on the electrode boundary around 2 nm. The mesh generator of FEMLAB produces equilateral triangles on the boundary. If the electrode is $20\,\mu\mathrm{m}$ long, we have then 10.000 elements on the boundary. This is a waste of elements, since we know that the gradients in the y direction along the electrode are very small.

7.2.1 New coordinate system

We know that our analytical solution for the electrokinetics decreases exponentially over a length-scale λ_D. Thus, we have considered introducing a new coordinate system such as

$$\xi(x) = e^{-x\,\frac{\alpha}{\lambda_D}}, \tag{7.3}$$

$$x(\xi) = -\frac{\lambda_D}{\alpha}\ln(\xi). \tag{7.4}$$

The y coordinates are left identical. Let us now consider an infinitely derivable function g. We then have

$$\partial_x g\big(\xi(x)\big) = -\,\xi\,\frac{\alpha}{\lambda_D}\,\partial_\xi g, \tag{7.5}$$

$$\partial_x{}^2 g\big(\xi(x)\big) = \xi\,\big(\frac{\alpha}{\lambda_D}\big)^2\Big[\partial_\xi g + \xi\partial_\xi{}^2 g\Big]. \tag{7.6}$$

With this, we can rewrite our equations system Eq. (7.1a) in the new coordinate system (ξ, y). However this approach is maybe not the most efficient one. We still have to deal with the following problems:

- Complex geometries
  Up to now, we considered very simple geometries. Unfortunately, if we want to deal with more general cases, this coordinates transformation would not apply.

- PDE form
  Once our equations are put into the new coordinates system, we still must fit them into the PDE general form. We loose then the direct interpretation of Γ as the ionic flux, which was convenient.

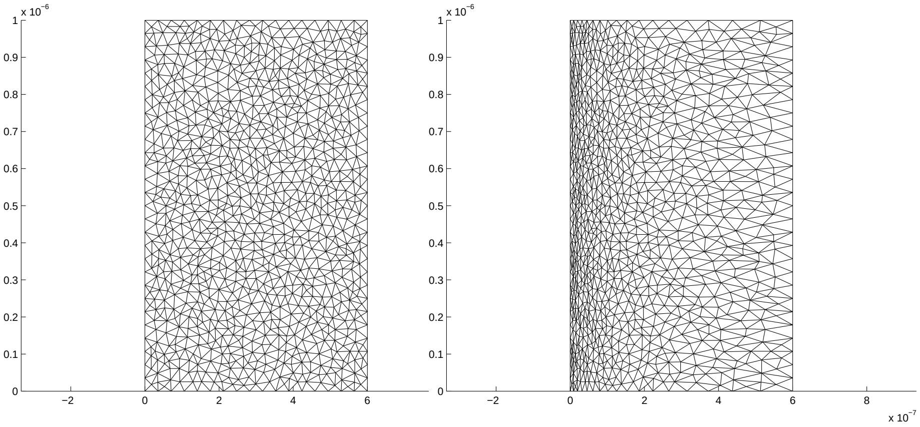

Figure 7.2: Example of transformed mesh for $\alpha = 25\lambda_D$. The mesh shown here is composed of 1872 elements. Actual meshes for the simulations contained between 5000 and 7000 elements.

- Fluid length scale
  The flow occurs on two length scales : λ_D and q^{-1}. Thus we may suppose that this new coordinate system is not suitable to solve the fluid flow.

We did not go further in this way and we moved forward to a more effective solution.

7.2.2 Mesh transformation

Instead of changing the coordinate systems, it is possible to apply a more effective mesh. This means that we must concentrate elements where needed, in the Debye layer. The considered geometry is a $L \times \ell$ rectangle. We apply the following transformation on the nodal coordinates,

$$\xi(x) = L\left(e^{\alpha\frac{x}{\lambda_D}} - 1\right)\left(e^{\alpha\frac{L}{\lambda_D}} - 1\right)^{-1}, \tag{7.7}$$

where α is a parameter for the transformation. We conserve the geometry since we have

$$\begin{aligned} \xi(0) &= 0, \\ \xi(L) &= L. \end{aligned} \tag{7.8}$$

Fig. 7.2 shows an example of a transformed mesh. We tested this transformation for a simple problem with good results (see Chap. B). However, when we applied this transformation to our model, we were confronted to some problems on the boundaries. Inside the domain, the solution was equivalent to the one obtained with a mesh given by the mesh tool from FEMLAB. Yet, on the first boundary elements, the solver gave unexpected discontinuities for the potential and the charges. Despite our efforts, we did not find the source of those artifacts.

Since it was still possible to run the simulations properly with the standard meshing tool of FEMLAB, we decided to leave this problem aside. This imposed some limitations on the $q\,\lambda_D$ values in the simulations. Thus, we mainly worked with $q = \pi\,10^6$ m^{-1}, $\lambda_D \simeq 10^{-8}$ m, giving $q\,\lambda_D \simeq 3 \times 10^{-2}$, so that the expansion in first order of $q\,\lambda_D$ from Chap. 4 is relevant.

7.3 Symmetric cosine modulation

In this section we present the numerical results obtained for the symmetric case described in Chap. 4. The parameters used for the simulations are given in Table. 7.1. A typical instantaneous velocity field obtained is shown in Fig. 7.3.

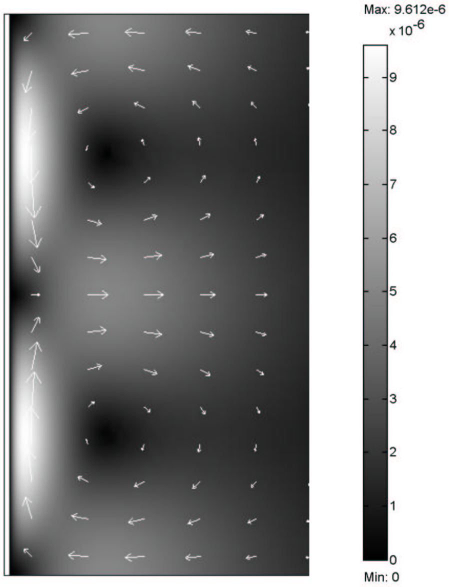

Figure 7.3: Typical plot of the instantaneous velocity field obtained for the Ajdari's model. The scale for x and y axis are the same. We have $\omega = 10^6$, $V_0 = 25$ mV. The domain is $1\,\mu$m long. We used the symmetry properties to divide the computational domain by 2.

7.3.1 Numerical and analytical results

We first wanted to be sure that the numerical solution of the model is consistent with the analytical problem from Chap. 4. However, we did not apply any expansion on the potential and the charges. Instead we kept the full solution[1], as we did in Chap. 5, and inserted numerical values for each constants so that we could compare the numerical

---

[1] This was done using Mathematica. The analytical solution found is valid within the Debye-Hückel approximation whereas the FEMLAB model does not use this assumption.

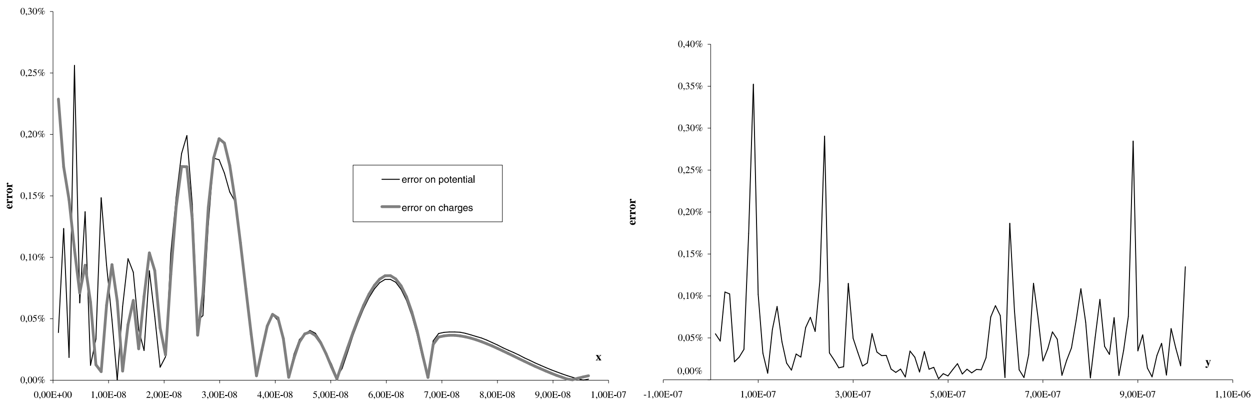

Figure 7.4: The left-hand side plot shows the numerical error e_1 versus x for ϕ and ν. The cross-section is $y = 0$, $0 < x < 10\,\lambda_D$ and $t = 0$. The right-hand side plot shows the numerical error for ϕ over the cross-section $x = 5\,\lambda_D$, $0 < y < \pi/q$

solution from FEMLAB and the analytical solution. The error is defined here by

$$e_1 = \frac{U_{\mathrm{an}} - U_{\mathrm{num}}}{\mathrm{Max}(U_{\mathrm{an}},\,\Omega)}, \tag{7.9}$$

where U_{an} is the analytical solution and U_{num} the solution provided by FEMLAB for the same problem. Fig. 7.4 shows a plot of the error for two different cross-section in the electrolyte. The error is confined under 1% which is a fairly good result.

In order to confirm our hypothesis made in Chap. 4, we compared computations without the convection term against computations with the convection term. For $\omega = 10^4$ s^{-1} and $V_0 = 25$ mV, we found an error e_1 around 2.6 %. For $V_0 = 0.5$ V, we found an error of 3.8 %. With voltage up to $V_0 = 1$ V, the error found was under 9 %. As the computations

Table 7.1: Typical parameters for the symmetric cosine simulations

Spatial modulation	q	$\pi \times 10^6$ m^{-1}
Insulator thickness	d	10 nm
Debye screening length	λ_D	9.63 nm
frequency	ω	$10^2 - 10^9$ s^{-1}
Thermal voltage	$V_T = k_B T/Ze$	25 mV
Applied voltage	V_0	0-25 mV
Bulk ionic density	n_∞	1 mol m^{-3}
Viscosity	η	10^{-3} Pa s
Mass density	ρ	10^3 kg m^{-3}
Ionic diffusion constant	D	10^{-9} m^2 s^{-1}
Capacitance ratio	$\delta = C_D/C_s$	8.3

are much faster without the convection term, in most of the following simulations, we discarded the convective effects.

7.3.2 Voltage dependence for the cosine modulation

We wish to obtain results for voltages where the Debye-Hückel approximation is not valid. We ran simulations with $0 < V_0 < 2\,\mathrm{V}$ for a dilute concentration of $c = 0.1\,\mathrm{mol\ m^{-3}}$ so that the Debye length is $\lambda_D \simeq 30$ nm. The results are given in Fig. 7.5. We used this dilute concentration and greater Debye length in order to have a more simple problem to solve numerically. As expected from the analytical model, the velocity obtained is proportional to V_0^2 for V_0 small enough. For higher voltages, this is not true anymore. For $V_0 \geq 1.5$ V, the time-averaged velocity diminishes. This confirms the picture given by Brown in Ref. [1]. He has shown in his experiment that the excitation frequency giving the maximum velocity is a function of the voltage. Thus, since we ran the simulations for a constant $\omega = 10^4\ \mathrm{s^{-1}}$, we do not give here the maximum velocity achievable for the given voltage.

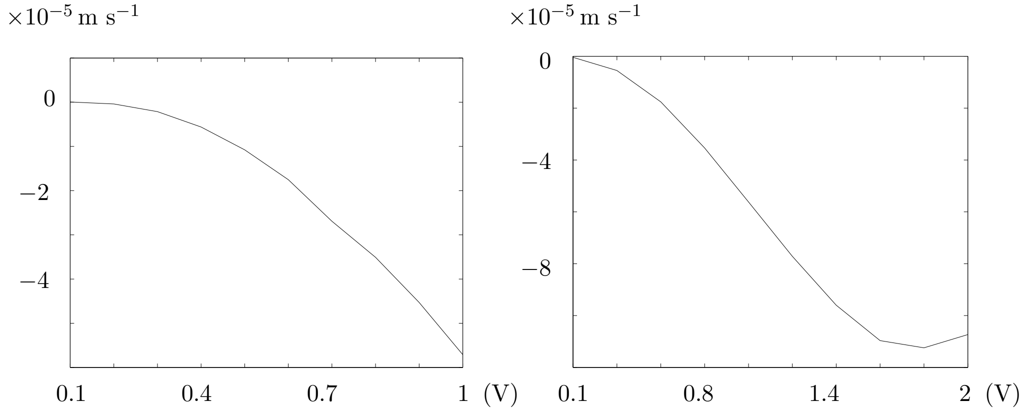

Figure 7.5: Symmetric cosine modulation: plots of time averaged velocity (x-component) in the electrolyte for $\omega = 10^4\ \mathrm{s^{-2}}$ and $c = 0.1\,\mathrm{mol\ m^{-3}}$. The velocity is taken on the point $(x, y) = (6.5\,\lambda_D\,;\,1/q \times \pi/2) = (0.2\,\mu\mathrm{m}; 5\,\mu\mathrm{m})$. The profile is proportional to V_0^2 for $V_0 \leq 0.5$ V. For $V_0 \geq 0.5$ V, we observe a linear relation between V_0 and $\langle v \rangle_t$. Finally, for $V_0 \geq 1.5$ V, $\langle v \rangle_t$ diminishes. This is not unexpected since we know from the experiments in Ref. [1] that the frequency giving the maximum speed is a function of the given voltage.

7.3.3 Frequency dependence for the cosine modulation

Here, we ran simulations in order to observe the fluid reversal. The results of those computations are shown in Fig. 7.6, where we observe the fluid motion inversion for ω_D between 2×10^5 and $5 \times 10^5\ \mathrm{s^{-1}}$. However, we can note that the speed for each direction differs by at least one order of magnitude.

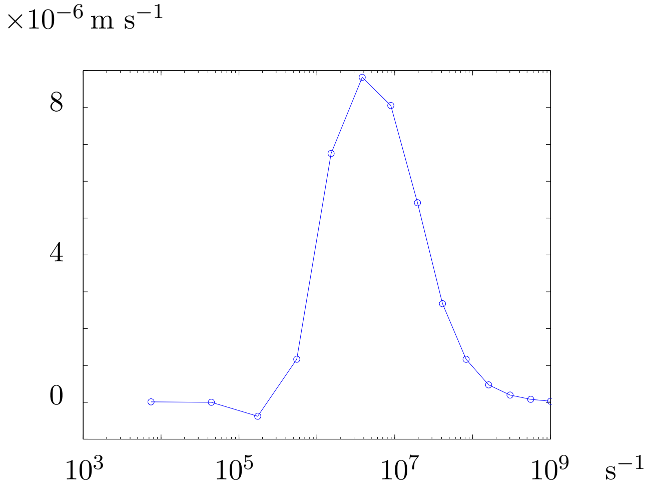

Figure 7.6: Symmetric cosine modulation: plots of time-averaged velocity (x–component) against ω. The velocity is evaluated on the point $(x, y) = (6.5\,\lambda_D\,,\,1/q \times \pi/2)$. The applied voltage is 25 mV. We have $\omega^* \simeq 3 \times 10^6$ and $\omega_D \simeq 3 \times 10^7$. The velocity reverts for ω between 2×10^5 and 5×10^5.

7.3.4 Computation over the voltage-frequency domain

We wish now to give more complete results for the voltage-frequency dependence. With this aim in mind, we ran a script to perform computations for a hundred points in the given domain. The results are shown in Fig. 7.7. We do not observe the fluid reversal, probably because of a lack of points in the proper area.

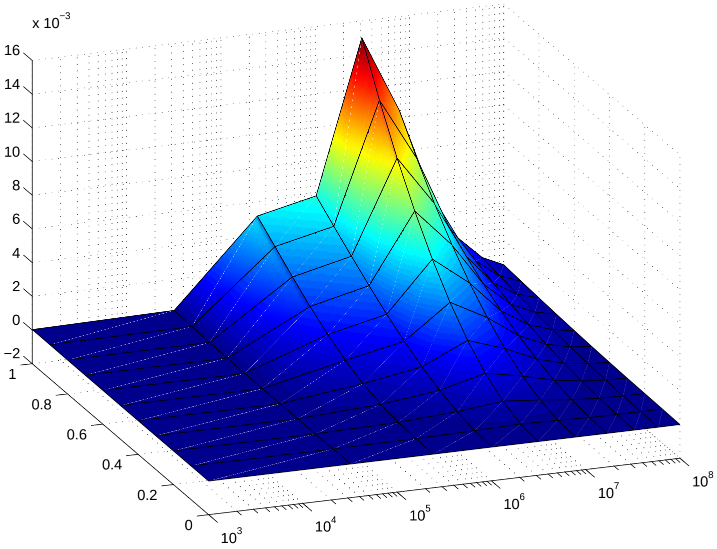

Figure 7.7: Symmetric cosine case : 3D Plots of time-averaged velocity (x–component) against voltage and frequency with $\lambda_D = 30.4$ nm, $\omega^* = 3.07 \times 10^5$ s^{-1}, $\omega_D = 1.07 \times 10^6$ s^{-1} The velocity is evaluated at the point $(x, y) = (6.5\,\lambda_D\,,\,1/q \times \pi/2)$

7.4 Simple symmetric electrode

7.4.1 simulation setup

The pumping effect is based on the existence of a mean flow over electrodes-arrays. The pumping velocity is obtained by introducing asymmetry in the electrode-array. The understanding of the symmetric case is thus a necessary step. We present now some simulations of the symmetric setup described by Green in [17] (see Chap. 3). In the experiments, the electrodes used were 100 μm wide. Yet, it was not possible to run simulations with the same size of electrodes for the reasons discussed in Sec. 7.2. The mesh then would contain far too many elements.[2] The size of the electrodes are 1 μm, the gap between the two electrodes being modelized by a smoothed Heavyside function. On the liquid/wall interface, we applied Neumann boundary conditions for the inert substract and Dirichlet boundary conditions for the electrode (see Fig. 7.8). We could have reduced the computational domain using some symmetry argument. However, since we have in mind to extend our simulations to the asymmetric case, we did not use those properties. Finally, we assume that the insulating layer thickness vanishes. This means that the capacitance ratio $\delta = C_D/C_s$ goes to zero which gives $\omega^* = q\,\lambda_D\,\omega_D$. In this simulation we have $\omega^* = 6.3 \times 10^5$ s^{-1}. In Fig. 7.9, we compare the experimental time-averaged streamlines obtained in Ref. [26] with our numerical results.

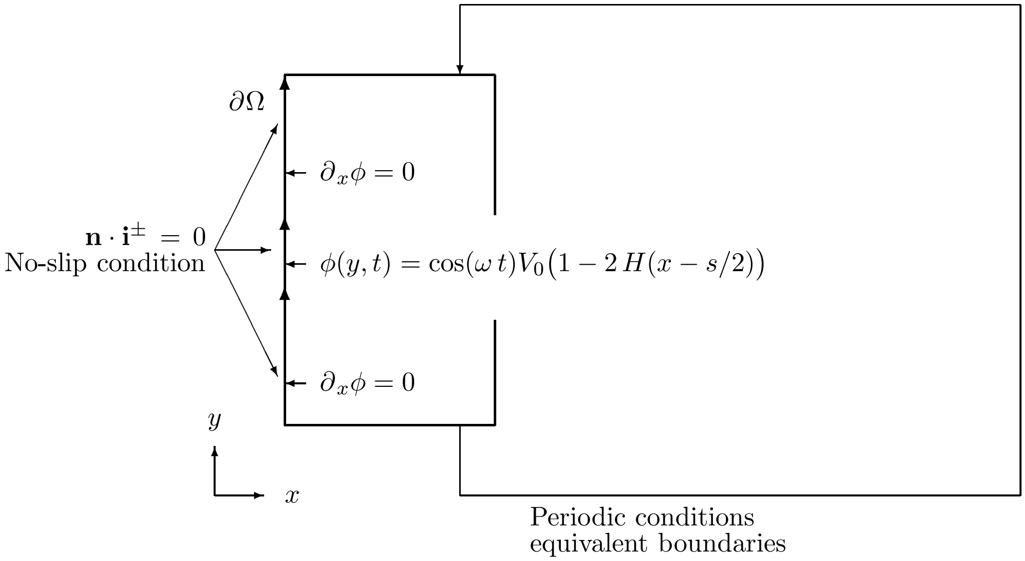

Figure 7.8: Boundary conditions applied for the Green setup. H denotes the Heavyside function and s the curve parameter, with $0 < s < 1$. The insulating layer is here discarded.

---

[2] The relevant parameter to consider being $q\lambda_D$, it is possible to decrease the ionic concentrations in order to obtain a larger Debye length and thus reduce the number of elements needed.

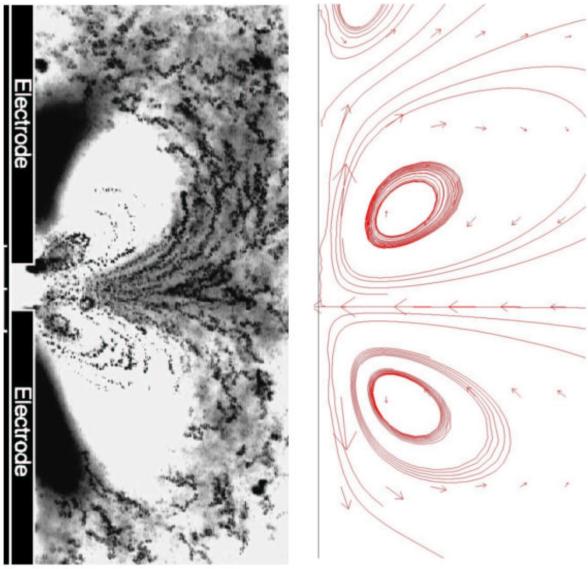

Figure 7.9: Comparison between experimental and my numerical streamlines patterns. On the left hand side, the experimental streamlines from Ref. [26]. On the right-hand side, my the numerical results.

7.4.2 Frequency dependence for the symmetric electrodes

We ran simulations over the frequency domain $10^4 < \omega < 10^8$ s^{-1}. The results are shown in Fig. 7.10. We have the resonance for $\omega \approx 10^6$ s^{-1}. The theoretical resonance calculated with the results from Chap. 4 is $\omega^* = 6.5 \times 10^5$, and we have here a fairly good agreement.

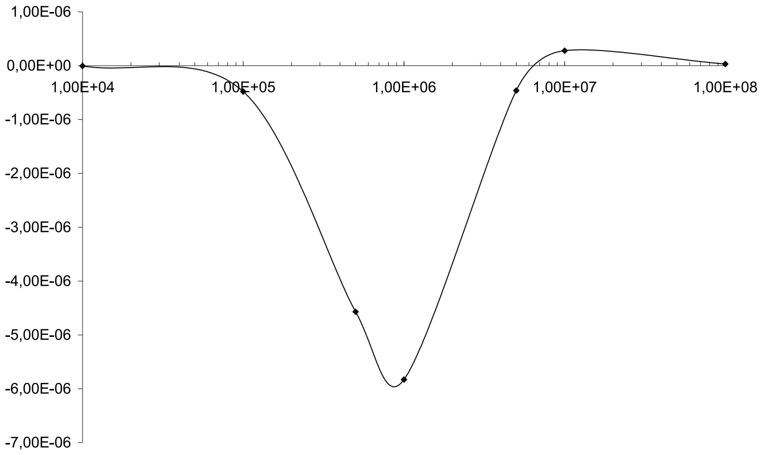

Figure 7.10: Plot of time-averaged velocity over the symmetric electrodes against frequency. The point where the velocity is evaluated at a distance $x = 0.3\,\mu$m over the inter-electrode gap.

7.5 The Brown pump

We use the same setup as described in Sec. 7.4.1, except that we do not have symmetric electrodes. The cell size is $1\,\mu$m, the gap between the two electrodes is modelized by a smoothed Heavyside function. The electrode-array is placed in an open channel without bonding. We have $\lambda_D \approx 10$ nm, $\omega_D = 10^7$ s^{-1} and $\omega^* = 6.5 \times 10^5$ s^{-1}.

7.5.1 Streamlines

In order to provide a simple picture of the flow over the electrode-array, we give some streamlines plots, for the instantaneous velocity field and for the time-averaged velocity field (Fig. 7.11).

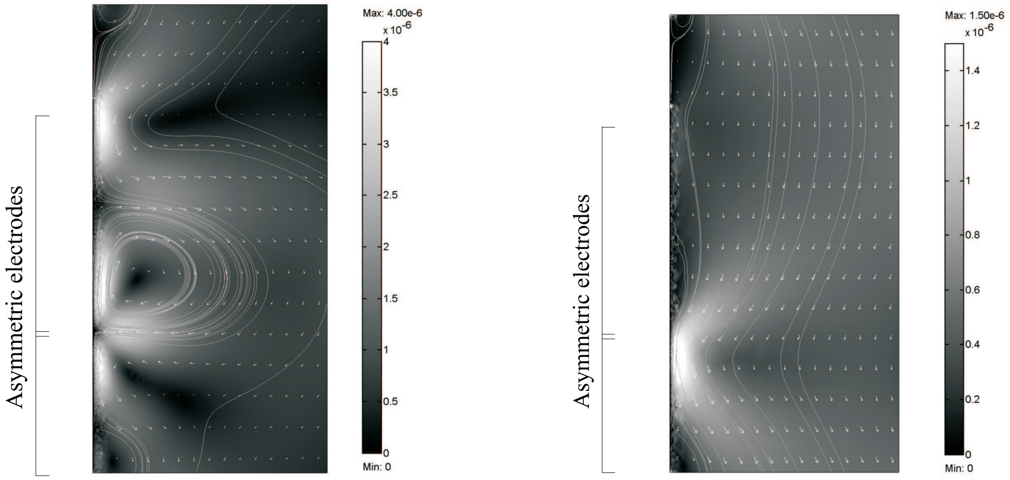

Figure 7.11: On the left-hand side: plot of instantaneous velocity field over the asymmetric electrodes with $\omega = 10^5$ s^{-1}, $V_0 = 10$ mV. The domain is $1\,\mu$m long. The maximum speed observed are about 4 μm s^{-1}. Note the rolls over each electrodes. On the right-hand side: time-averaged velocity field for the same parameters. Note the presence of a pumping velocity about 1 μm s^{-1} .

7.5.2 Frequency dependence

In Fig. 7.12, we give some plots for a low voltage simulation with $V_0 = 10$ mV in order to show the fluid reversal. The fluid reversal occurs around $\omega = 5 \times 10^5$, which is lower than ω^*. This result is not predicted by our theory from Chap. 5. The frequency given by the theory would be around ω_D. It could be interesting to run a complete simulation over the frequency-domain with voltage up to 5 V so that we can compare the map obtained by the numerics with the map obtained by Studer in [21]. However we did not have time to conduct this study in the frame of this thesis. Each computation takes around one hour and we need at least a hundred points. Assuming that no unexpected problem occurs, this means at least four days of computation.

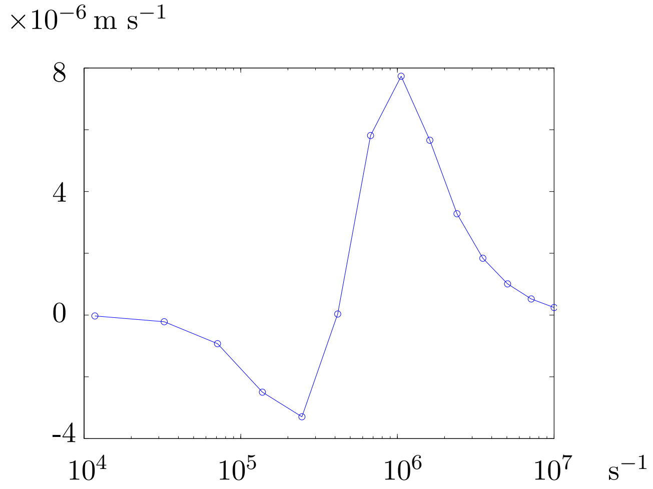

Figure 7.12: Plot of time-averaged pumping velocity agains ω for the Brown pump with $V_0 = 10$ mV. The velocity is taken at $0.3\,\mu$m over the large electrode.

7.6 Discussion

In this chapter, we first showed the effectiveness and limitations of FEMLAB to solve our coupled equations. Previous numerical studies (see Ref. [26]) used a slip-velocity model and did not fully resolve the Debye layer like we do. However we did not have time to run an exhaustive numerical study but the needed tools have been tested and validated. We confirmed the picture that the convective effects do not have a massive impact on the velocity field obtained. Yet, it could be interesting to check this matter more carefully. If we want to compare our linear analytical results (with a Debye–Hückel approximation), to our numerical results with voltage $V_0 > 25$ mV, we are confronted to unpredicted phenomena coming from the non-linearities. Thus, is seems that the linearization of the equations via the Debye–Hückel approximation induces a loose of not only quantitative but also qualitative relevance of our model for voltage greater than 25 mV.

Chapter 8

Conclusion

AC EO pumps based on electrode-arrays could be an interesting solution for integrated micropumps in lab-on-a-chip devices. Their design is fairly simple and the voltage needed is low, which are important matters in microfluidics. Following up on the work of Ajdari in [6], we proposed a model for the symmetric electrode array, where the Debye layer is fully resolved (see Chap. 4).[1] The asymmetric array is then considered as a perturbed symmetric array in Chap. 5. We worked in the frame of the Debye-Hückel approximation with excitation frequencies small in front of the Debye frequency, whereas the experiments are conducted beyond those voltage and frequency domains. Yet, we found good agreement for the resonance frequency between our model and the experiments. Nevertheless, our low-frequency analytical results were not able to predict the fluid reversal observed in Ref. [21]. We then studied the full analytical solution with the help of Mathematica (see Chap. 5). We showed that the fluid reversal phenomenon is contained in our electrolyte model. This work is summarized in Fig. 8.1, starting with the symmetric case with a pure harmonic flow and ending on the asymmetric electrode-array giving rise to a pumping velocity. In Chap. 7, we conducted a numerical study where we fully simulated the Debye layer using the finite element method solver FEMLAB. We demonstrated the effectiveness of this approach. We confirmed the fact that the fluid reversal can be described by our model. Moreover we investigated domains unreachable within the analytics. This means voltages beyond the reach of the Debye-Hückel approximation, at high frequencies and with convection coupling.

A lot of theoretical work has still to be done about the electrode-arrays. We still did not provide a simple analytical solution of our model in the general case. Our model does not take into account various physical properties of the electrode-arrays but the non-linearities and the equations coupling already limit the analytical approach. The model does not include charges injection that are likely to happen for voltages high enough. It does not include Joule heating and thermal effects either. Nevertheless we obtained consistent values for resonance frequencies and for pumping velocities.

Concerning the numerical simulations, we can give at least three interesting studies to be conducted. First, it should be possible to give an optimized geometry, possibly non-flat, for the electrodes. Second, it should be also possible to give some relevant parameters for the frequency at which the motion reversal occurs. And finally, the influence of the height of the pumping channel on the flow rate has yet to be investigated.

---

[1] A paper was submitted to Phys.Rev. E presenting this work.

At this point, it should be clear that the electrode-array pump is a very open topic of discussion. The available experimental data is still very limited and the theoretical models found in the literature can not fully explain the dynamics observed. We can thus expect promising developments in the future.

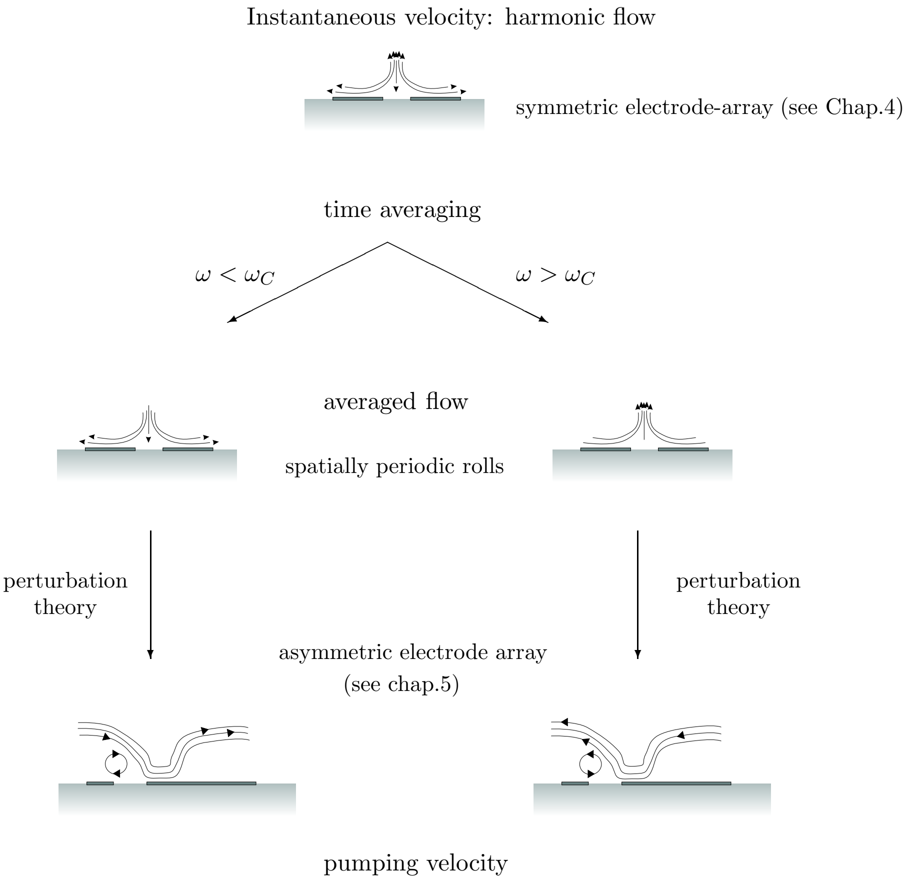
Instantaneous velocity: harmonic flow
symmetric electrode-array (see Chap.4)
time averaging
$\omega < \omega_C$
$\omega > \omega_C$
averaged flow
spatially periodic rolls
perturbation theory
perturbation theory
asymmetric electrode array
(see chap.5)
pumping velocity

Figure 8.1: Summary of the study conducted on the electrode-arrays. We first described the symmetric electrode-array with the means of cosine modulated potentials. After time-averaging, we obtain a mean flow consisting of a spatially periodic roll patterns. It is possible to obtain two directions for the mean flow. In this figure, we introduced ω_C as the critical frequency where we have $v = 0$ and the inversion of the pumping velocity. Then, introducing a perturbation on the potential or on the surface capacitance, we obtain an asymmetric electrode-array giving rise to a pumping velocity.

Appendix A

Electrode-array with non-zero zeta potential

In this appendix, we work in the frame defined in Chap. 4, except that:

- Zeta potential
  We assume the zeta potential to be finite. We then introduce a perturbation ζ_1 with spatial and time modulation.

- Insulating layer
  The insulating layer previously introduced is now discarded. We wish to only consider the effect of the potential perturbation.

A.1 Non-zero intrinsic zeta potential

Consider an aqueous solution of a salt containing a positive and a negative type of ions with charges $+Ze$ and $-Ze$, respectively, where Z is the valence and e the elementary charge. The liquid is confined to the half-space $x > 0$ by an impenetrable, homogeneous and planar wall placed in the plane $x = 0$. The electric potential on the wall is denoted $\zeta(y,t)$. Charge transfer processes at the wall gives rise to a constant intrinsic zeta potential ζ_0, while an external voltage source leads to a smaller, possibly correction, of amplitude ζ_1, such that

$$\zeta(y,t) = \zeta_0 + \zeta_1 \cos(qy)\, e^{i\omega t}, \qquad |\zeta_1| \ll |\zeta_0|. \tag{A.1}$$

The boundary conditions for the electric potential ϕ are

$$\phi(0,y,z,t) = \zeta(y,t), \qquad \phi(\infty,y,z,t) = 0. \tag{A.2}$$

In the following the ionic densities $n^{\pm}$, the potential ϕ, the velocity field $\mathbf{v}$, and the pressure p, are all written as a zero order contribution, for the case when ζ_1 is zero, plus a first order contribution, when ζ_1 differs from zero,

$$n^{\pm}(\mathbf{r},t) = n_0^{\pm}(x) + n_1^{\pm}(x,y,t), \tag{A.3a}$$

$$\phi(\mathbf{r},t) = \phi_0(x) + \phi_1(x,y,t), \tag{A.3b}$$

$$\mathbf{v}(\mathbf{r},t) = \mathbf{0} + \mathbf{v}_1(x,y,t), \tag{A.3c}$$

$$p(\mathbf{r},t) = p_0(x) + p_1(x,y,t). \tag{A.3d}$$

Note that we have anticipated that in zeroth order the velocity is zero and the pressure a constant.

From the number densities of the ions $n^{\pm}(\mathbf{r},t)$ we form the difference $\nu(\mathbf{r},t)$, and the sum $n^{\Sigma}(\mathbf{r},t)$,

$$\nu(\mathbf{r},t) \equiv n^{+}(\mathbf{r},t) - n^{-}(\mathbf{r},t) = \nu_0(x) + \nu_1(x,y,t), \tag{A.4a}$$

$$n^{\Sigma}(\mathbf{r},t) \equiv n^{+}(\mathbf{r},t) + n^{-}(\mathbf{r},t) = n_0^{\Sigma}(x) + n_1^{\Sigma}(x,y,t). \tag{A.4b}$$

The ionic flux densities are denoted $\mathbf{i}^{\pm}(\mathbf{r},t)$. The continuity equations for each type of ion in the absence of any chemical reactions in the system can thus be stated as

$$\partial_t n^{\pm}(\mathbf{r},t) = -\boldsymbol{\nabla}\cdot\mathbf{i}^{\pm}(\mathbf{r},t). \tag{A.5}$$

The electric current densities are denoted $\mathbf{j}^{\pm}$,

$$\mathbf{j}^{\pm}(\mathbf{r},t) = \pm Ze\,\mathbf{i}^{\pm}(\mathbf{r},t). \tag{A.6}$$

The presence of gradients in the densities $\boldsymbol{\nabla} n^{\pm}(\mathbf{r},t)$ and/or the electric potential $\boldsymbol{\nabla}\phi(\mathbf{r},t)$ will generate ionic current densities. These are given by the Nernst-Planck equation

$$\mathbf{i}^{\pm}(\mathbf{r},t) = -D\boldsymbol{\nabla} n^{\pm}(\mathbf{r},t) \mp \mu n^{\pm}(\mathbf{r},t)\boldsymbol{\nabla}\phi(\mathbf{r},t) + n^{\pm}(\mathbf{r},t)\mathbf{v}(\mathbf{r},t), \tag{A.7}$$

where, for simplicity, we have assumed that the two types of ions have the same diffusion constant D and the same mobility μ. We remind the reader that both the diffusion constant D and the electric conductivity σ can be obtained from the mobility μ as

$$D = \frac{k_{\mathrm{B}}T}{Ze}\,\mu, \tag{A.8}$$

$$\sigma^{\pm}(\mathbf{r},t) = Ze\,n^{\pm}(\mathbf{r},t)\,\mu. \tag{A.9}$$

The governing equations for $\phi(\mathbf{r},t)$ and $n^{\pm}(\mathbf{r},t)$ can now be written down. Combining the Poisson equation with Eq. (A.4a) yields

$$\boldsymbol{\nabla}^2\phi(\mathbf{r},t) = -\frac{Ze}{\epsilon}\,\nu(\mathbf{r},t), \tag{A.10}$$

and insertion of the Nernst-Planck equation Eq. (A.7) into the continuity equation Eq. (A.5) leads to

$$\partial_t n^{\pm}(\mathbf{r},t) = D\,\boldsymbol{\nabla}^2 n^{\pm}(\mathbf{r},t) \pm \mu\boldsymbol{\nabla}\cdot\big[n^{\pm}(\mathbf{r},t)\,\boldsymbol{\nabla}\phi(\mathbf{r},t)\big] - \boldsymbol{\nabla}\cdot[n^{\pm}(\mathbf{r},t)\,\mathbf{v}(\mathbf{r},t)]. \tag{A.11}$$

A.1.1 Zeroth order result

For the zeroth order the system is in thermodynamic equilibrium. The velocity field is zero, the pressure is constant, and the ionic currents due to the gradients in the electric potential and in the density exactly cancel each other.

We now linearize the continuity equation Eq. (A.11) in the density as follows. We assume $n_0^\pm(\infty) \equiv n_*$ and write

$$n_0^\pm(x) = n_* + \delta n_0^\pm(x), \qquad \delta n_0^\pm(\infty) = 0. \tag{A.12}$$

Since it is a non-zero ζ_0 that spawns $\delta n^\pm \neq 0$, we shall prove later that $|\delta n_0^\pm| \ll n_*$ when the electrostatic energy is much smaller than the thermal energy,

$$Ze\,\zeta_0 \ll k_\mathrm{B}T. \tag{A.13}$$

In this case the so-called Debye-Hückel approximation is valid, i.e., we substitute $n^\pm(\mathbf{r},t)\boldsymbol{\nabla}\phi(\mathbf{r},t)$ by $n_*\,\boldsymbol{\nabla}\phi(\mathbf{r},t)$ in Eq. (A.11). Using this, and noting $\partial_t n^\pm(x) = 0$ as well as $\mathbf{v}_0 = \mathbf{0}$, we arrive at

$$0 = D\left[\boldsymbol{\nabla}^2\delta n_0^\pm(x) \pm \frac{Zen_*}{k_\mathrm{B}T}\boldsymbol{\nabla}^2\phi_0(x,t)\right], \tag{A.14}$$

When the Poisson equation Eq. (4.3a) is inserted into Eq. (A.14), we obtain an equation only involving densities,

$$0 = D\left[\boldsymbol{\nabla}^2\delta n_0^\pm(x) \mp \frac{1}{2\lambda_D^2}\nu_0(x)\right], \tag{A.15}$$

where we have introduced the Debye screening length λ_D given by

$$\lambda_D \equiv \sqrt{\frac{\epsilon k_\mathrm{B}T}{2Z^2e^2n_*}}. \tag{A.16}$$

By adding the "±"-equations of Eq. (A.15) we obtain $\boldsymbol{\nabla}^2 n_0^\Sigma(x) = 0$, which mean that $n^\Sigma(x)$ is a linear function of x. But since $n_0^\pm(\infty) = n_*$ we must conclude

$$n_0^\Sigma(x) = 2n_*. \tag{A.17}$$

If instead we form the difference of the "±"-equations of Eq. (A.15) we obtain a partial differential equation involving only $\nu_0(x)$,

$$0 = \boldsymbol{\nabla}^2\nu_0(x) - \frac{1}{\lambda_D^2}\nu_0(x). \tag{A.18}$$

It is easily proven by direct insertion that the solutions for ϕ_0, ν_0, and $n_0^\pm$ are given by

$$\phi_0(x) = \zeta_0\, e^{-x/\lambda_D}, \tag{A.19a}$$

$$\nu_0(x) = -2\,\frac{Ze\zeta_0}{k_\mathrm{B}T}\,n_*\,e^{-x/\lambda_D}, \tag{A.19b}$$

$$n_0^\pm(x) = n_* \pm \frac{1}{2}\,\nu_0(x). \tag{A.19c}$$

Note how the validity of the Debye-Hückel approximation follows from Eqs. (A.19b) and (A.19c): $|n^{\pm}(x) - n_*| \ll n_*$ when $Ze\zeta_0 \ll k_{\mathrm{B}}T$.

Since the velocity field is zero ($\mathbf{v}_0 = \mathbf{0}$) the Navier–Stokes equation gives

$$\mathbf{0} = -\boldsymbol{\nabla} p_0 - Ze\nu_0 \boldsymbol{\nabla}\phi_0, \tag{A.20}$$

from which we get

$$p_0(x) = \text{const.} + \frac{(Ze\zeta_0)^2}{k_{\mathrm{B}}T}\, n_*\, e^{-2x/\lambda_D}. \tag{A.21}$$

A.1.2 First order equations

The first order contribution to the diffusion-convection equation Eq. (A.11) is

$$\begin{aligned}\partial_t n_1^{\pm}(\mathbf{r},t) = D\,\boldsymbol{\nabla}^2 n_1^{\pm}(\mathbf{r},t) - [\boldsymbol{\nabla} n_0^{\pm}(x)]\cdot\mathbf{v}_1(\mathbf{r},t)\\ \pm\mu\Big[[\boldsymbol{\nabla} n_0^{\pm}(x)]\cdot\boldsymbol{\nabla}\phi_1(\mathbf{r},t) + n_0^{\pm}(x)\boldsymbol{\nabla}^2\phi_1(\mathbf{r},t)\\ [\boldsymbol{\nabla} n_1^{\pm}(\mathbf{r},t)]\cdot\boldsymbol{\nabla}\phi_0(x) + n_1^{\pm}(\mathbf{r},t)\boldsymbol{\nabla}^2\phi_0(x)\Big].\end{aligned} \tag{A.22}$$

By forming $\partial_t n^+ - \partial_t n^-$ the following expression for $\partial_t\nu_1$ appears

$$\partial_t\nu_1 = D\Big[\boldsymbol{\nabla}^2\nu_1 - \frac{1}{\lambda_D^2}\,\nu_1 + \frac{\nu_0(x)}{2\lambda_D n_*}\,\big(\partial_x n_1^{\Sigma}\big) - \frac{\nu_0(x)}{2\lambda_D^2 n_*}\,n_1^{\Sigma}\Big]. \tag{A.23}$$

Likewise, we find for the sum $\partial_t n^+ + \partial_t n^-$

$$\begin{aligned}\partial_t n_1^{\Sigma} = D\Big[\boldsymbol{\nabla}^2 n_1^{\Sigma} - \frac{\nu_0(x)}{2\lambda_D n_*}\,\big(\partial_x\nu_1\big) - \frac{\nu_0(x)}{\lambda_D^2 n_*}\,\big(\partial_x\nu_1\big)\\ - \frac{Ze\nu_0(x)}{k_{\mathrm{B}}T\lambda_D}\,\big(\partial_x\phi_1\big) - \frac{\nu_0(x)}{D\lambda_D}\,(\mathbf{v}_1)_x\Big].\end{aligned} \tag{A.24}$$

From the Poisson equation we get

$$\boldsymbol{\nabla}^2\phi_1 = -\frac{Ze}{\epsilon}\nu_1, \tag{A.25}$$

Finally, for the velocity field we have the Navier–Stokes equation

$$\rho\big(\partial_t\mathbf{v}_1 + \mathbf{v}_1\cdot\boldsymbol{\nabla}\mathbf{v}_1\big) = -\boldsymbol{\nabla} p_1 + \eta\boldsymbol{\nabla}^2\mathbf{v}_1 - Ze\nu_1\boldsymbol{\nabla}\phi_1 \tag{A.26a}$$

along with the incompressibility

$$\boldsymbol{\nabla}\cdot\mathbf{v}_1 = 0. \tag{A.26b}$$

We thus have 5 coupled differential equations for the 5 unknowns, $\mathbf{v}_1$, p_1, ϕ_1, n_1^{Σ}, and ν_1. Using an approximation in the high temperature limit, we can decouple some of those equations.

In the high-temperature limit Eq. (A.23) becomes

$$\partial_t \nu_1 \simeq D\Big[\boldsymbol{\nabla}^2 \nu_1 - \frac{1}{\lambda_D^2}\,\nu_1\Big],\ k_{\mathrm{B}}T \gg Ze\zeta_0, \tag{A.27}$$

which for an ansatz with a $\cos(qy)e^{i\omega t}$-dependence has a general solution

$$\nu_1(x,y,t) = C_1 e^{-\kappa x}\cos(qy)e^{i\omega t}$$

with $\omega_D = D/\lambda_D^2$ and

$$\kappa = (1/\lambda_D)\sqrt{1+(q\lambda_D)^2 + i\omega/\omega_D}. \tag{A.28}$$

Substituting into Eq. (A.25) and assuming a $\cos(qy)e^{i\omega t}$-dependence we get the following general solution for the potential

$$\begin{aligned}\phi_1(x,y,t) = \Big[&- C_1 \frac{Ze\lambda_D^2}{\epsilon}\frac{\omega_D}{\omega_D + i\omega} e^{-\kappa x} \\ &+ C_2 e^{-qx}\Big]\cos(qy)e^{i\omega t}.\end{aligned} \tag{A.29}$$

In order to satisfy the boundary condition at $x = 0$ we have

$$\zeta_1 = -C_1 \frac{Ze\lambda_D^2}{\epsilon}\frac{\omega_D}{\omega_D + i\omega} + C_2. \tag{A.30}$$

Since $\partial_y \phi_1 = \mathcal{O}^2(q\lambda_D)$ the Gauss's theorem gives a good approximation for the surface charge

$$-\partial_x \phi_1(x,y,t)|_{x=0} = -\frac{Ze}{\epsilon}\int_0^\infty dx\,\nu_1(x,y,t), \tag{A.31}$$

that gives

$$C_1\kappa\frac{Ze\lambda_D^2}{\epsilon}\frac{\omega_D}{\omega_D + i\omega} - C_2 q = C_1 \frac{Ze}{\epsilon\kappa}. \tag{A.32}$$

Solving for C_1 and C_2 we obtain (after substantial re-arrangements)

$$\phi_1(x,y,t) = \zeta_1 \frac{\kappa e^{-\kappa x} - q e^{-qx}}{\kappa - q}\,\cos(qy)e^{i\omega t}, \tag{A.33}$$

and

$$\nu_1(x,y,t) = -\frac{\kappa\epsilon\zeta_1}{Ze}(\kappa+q)e^{-\kappa x}\cos(qy)e^{i\omega t}. \tag{A.34}$$

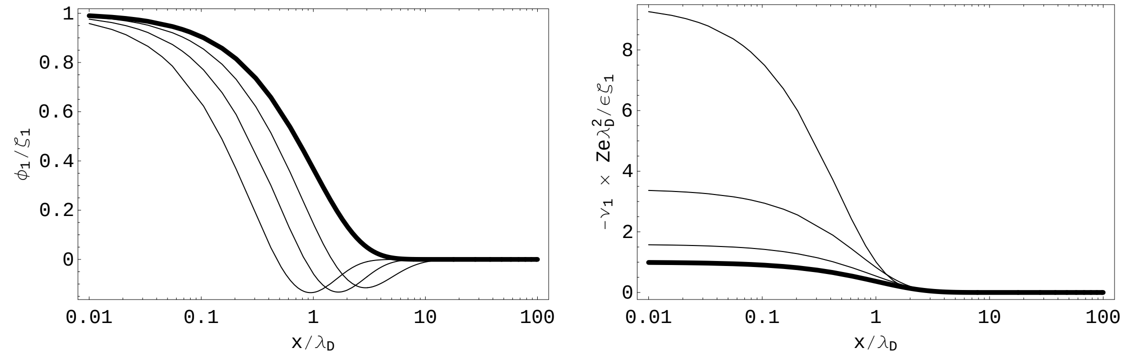

Figure A.1: Plot of ϕ_1 and ν_1 versus x, for $y = 0$, $t = 0$, and $\omega = 0$. For ϕ_1, left to right, we have $q\lambda_D = 2$, 1, 0.4, and 0 (thick line). The same values apply for ν_1, from top to bottom.

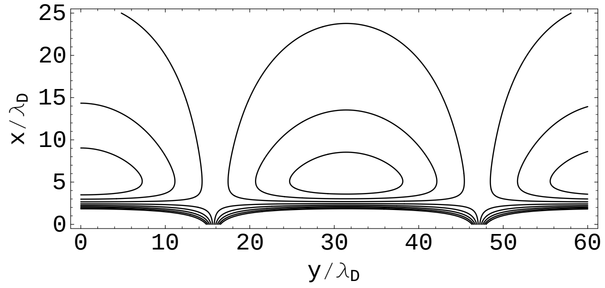

Figure A.2: Equipotential lines for ϕ_1 for $q\lambda_D = 0.1$, $t = 0$, and $\omega = 0$.

A.1.3 Body force

We now consider the body force, without making expansions. For the electrical field we have :

$$\mathbf{E}_0(\mathbf{r}, t) = \zeta_0 \lambda_D^{-1} e^{-x/\lambda_D} \hat{\mathbf{x}}, \tag{A.35}$$

$$\mathbf{E}_1(\mathbf{r}, t) = -\boldsymbol{\nabla}\, \phi_1(x, y, t). \tag{A.36}$$

For the body force, which is a non-linear expression, we have

$$\mathbf{g}_0 + \mathbf{g}_1 = Ze(\nu_0 + \nu_1)(\mathbf{E}_0 + \mathbf{E}_1) \tag{A.37}$$

and neglecting the second-order contribution $\nu_1 \mathbf{E}_1$ we get

$$\mathbf{g}_1 \simeq Ze(\nu_0 \mathbf{E}_1 + \nu_1 \mathbf{E}_0). \tag{A.38}$$

We now make an expansion for $q\lambda_D \ll 1$ and $\frac{\omega}{\omega_D} \ll 1$:

$$\mathbf{g}_1 \simeq -\frac{\epsilon\zeta_0\zeta_1}{\lambda_D^3} e^{-2x/\lambda_D}\, e^{i\omega\, t} \begin{pmatrix} \left(2 + i(\frac{3}{2} - \frac{x}{\lambda_D})\frac{\omega}{\omega_D}\right)\, \cos(q\, y) \\ \\ \left(q\,\lambda_D - \frac{1}{2} i x\, q \frac{\omega}{\omega_D}\right)\, \sin(q\, y) \end{pmatrix}. \tag{A.39}$$

Let's write the body force as a sum of two terms, a constant term and a frequency dependent term:

$$\mathbf{g}_1 = \mathbf{g}_1^0 + \mathbf{g}_1^\omega, \tag{A.40}$$

where

$$\mathbf{g}_1^\omega = -\frac{\epsilon\zeta_0\zeta_1}{\lambda_D^3} e^{-2x/\lambda_D}\, e^{i\,\omega\, t} \begin{pmatrix} i(\frac{3}{2} - \frac{x}{\lambda_D})\frac{\omega}{\omega_D}\, \cos(q\, y) \\ \\ -\frac{i}{2} x\, q \frac{\omega}{\omega_D}\, \sin(q\, y) \end{pmatrix}. \tag{A.41}$$

From this, it is possible to apply a slip velocity model to obtain the bulk velocity. However we can already discuss our results for the body-force.

A.2 Discussion

We wish now to compare the vanishing zeta potential case with the results form Chap. 4. The spatial modulation of the body-force obtained in Eq. (A.39) is q whereas in Eq. (4.25a) it was $2q$. This means that the flow patterns following from Eq. (A.39) will have a q modulation whereas the rolls from Chap. 4 had a $2q$ spatial modulation. Thus the topology of the flow totally differs from one case to the other.

If we now investigate the time-average of the body-force from Eq. (A.38), it is clear that we obtain 0 since

$$\begin{aligned} \left\langle \mathbf{E}_1 \right\rangle_t &= 0, \\ \left\langle \nu_1 \right\rangle_t &= 0. \end{aligned} \tag{A.42}$$

Thus, a non-zero time-averaged body-force — which is required to get any pumping velocity—, would rely on second order terms such as $\left\langle \mathbf{E}_1\, \nu_1 \right\rangle_t$. Those terms are the one calculated in Chap. 4!

This study assumed that $\zeta_1 \ll \zeta_0$. If we now assume that ζ_1 and ζ_0 are of the same magnitude, we may suppose that a q and a $2q$ modulated flow patterns will interfere with yet unpredicted results. However, the existence of the intrinsic zeta potential impose spatially constant constraint on the charges. This effect is not likely to increase the pumping velocities but rather decrease them.

Appendix B

Mesh transformation: a test

B.1 Analytical problem

This chapter is based on the work of Laurits H. Olesen. We consider a simple analytical problem of which we know the solution:

$$\Omega = \big(x, y\big)\,\epsilon\,\big[0, 1\big] \times \big[0, 1\big] \tag{B.1}$$

$$\boldsymbol{\nabla} u^2 = \big(a^2 - \pi^2\big)\, u \quad \text{for } (x, y)\,\epsilon\,\Omega \tag{B.2}$$

$$u = \sin(\pi\, y)\, e^{-a\, x} \quad \text{for } (x, y)\,\epsilon\,\partial\Omega. \tag{B.3}$$

It is easily proved that the solution of this problem is

$$u = \sin(\pi\, y)\, e^{-a\, x} \quad \text{for } (x, y)\,\epsilon\,\Omega. \tag{B.4}$$

Laurits H. Olesen made a FEMLAB script to solve numerically this problem. The results obtained with a standard mesh from FEMLAB and a highly distorted mesh were equivalent and very close to the analytical solution. This shows that it is possible to use high aspect ratio elements in FEMLAB under some circumstances. Yet, this method did not work in the more complicated simulations from Chap. 7.

B.2 Script listing

```
% 5/08/04
% Lauritz Højgaard Olesen
% Modified by L.Belmon for FEMLAB 3.0a
%
% we allow 1000 nodes
n = 1000;

% exponentially scaled mesh in the x-direction
L = 1; A = 2; fem.geom = rect2(0,L,0,1);
fem.mesh=meshinit(fem,'hmax',sqrt(L/n)); disp(fem.mesh);

%creating a mesh a struct type that we can work with.
mesh=struct('p',fem.mesh.p,'e',fem.mesh.e,'t',fem.mesh.t,'v',fem.mesh.v,'equiv',fem.mesh.equiv);
```

```
% plot the initial mesh
figure(1);meshplot(fem);axis equal;

%applying the nodal transformation
[n,m]=size(fem.mesh.p);
mesh.p(1,:)=L*[exp(fem.mesh.p(1,:)/A)-exp(0/A)]/[exp(L/A)-exp(0/A)];
fem.mesh=femmesh(mesh);

% plot the transformed mesh
figure(2);subplot(2,2,1);meshplot(fem); axis equal;

%setting up the equations
fem.sdim = {'x' 'y'}; fem.dim = {'u'}; fem.const = {'a' 25};
fem.expr = {'u0' '(x<1e-8)'};
fem.form = 'general'; fem.equ.ga = {{{'ux' 'uy'}}};
fem.equ.f ={{{'(a^2-pi^2)*u'}}};
% Dirichlet boundary conditions everywhere
fem.bnd.r = {{'u-u0'}};

%Solving
fem = femdiff(fem); fem.xmesh = meshextend(fem);
fem.sol = femlin(fem);

subplot(2,2,2);
postplot(fem,'tridata','u','triz','u','refine',1,'axisequal','on');

% error
disp('error(Linf) error(L2) min(meshqual)')
disp([postmax(fem,'u-u0')/postmax(fem,'u0') ...
 sqrt(postint(fem,'(u-u0)^2')/postmax(fem,'u0^2')) ...
 min(meshqual(fem.mesh.p,fem.mesh.t))])
```

Appendix C

Paper submitted to Phys. Rev. E

Title
Electro-hydrodynamics of bi-ionic electrolytes driven by modulated surface potentials

Authors
N.A. Mortensen, L. Belmon, L.H. Olesen and H. Bruus

Reference
http://arxiv.org/abs/cond-mat/0407160

arXiv:cond-mat/0407160 v1 7 Jul 2004

Electro-hydrodynamics of bi-ionic electrolytes driven by modulated surface potentials

Niels Asger Mortensen,[1] Lionel Belmon,[1,2] Laurits Højgaard Olesen,[1] and Henrik Bruus[1]
[1] *MIC – Department of Micro and Nanotechnology,*
Technical University of Denmark, DK-2800 Kongens Lyngby, Denmark
[2] *Ecole Centrale de Nantes, F-44321 Nantes, France*

(Dated: July 7, 2004)

We study the electro-hydrodynamics of the Debye screening layer that arises in an aqueous bi-ionic solution near a planar insulating wall when applying a spatially modulated ac-voltage with angular frequency ω. Using first order perturbation theory we establish the governing equations for the full non-equilibrium problem and obtain analytic solutions for the pressure and velocity field of the electrolyte and for the electric potential. Our work provides the theoretical foundations of phenomenological models discussed in the literature. The non-equilibrium approach also reveals unexpected high-frequency dynamics not predicted by phenomenological models.

PACS numbers: 47.65.+a, 47.32.-y, 47.70.-n, 85.90.+h

I. INTRODUCTION

Recently, there has been quite some interest in electro-hydrodynamics in microfluidic systems. AC-driven, modulated surface potentials have been used for pumping [1–7] and for fluid circulation and mixing, see Refs. [8–10] and references therein.

We revisit the problem studied by Ajdari [1] where an electrolyte is perturbed by an AC-driven spatially modulated surface potential. However, instead of modelling the surface as well as the Debye layer by simple capacitors we develop a full non-equilibrium description of the electro-hydrodynamics. This allows us to study the full dynamics of ion concentrations, electrical potentials, velocity fields, pressure fields, and electrical currents.

In the following we consider a bi-ionic electrolyte, *i.e.*, an aqueous solution of a salt containing a positive and a negative type of ions with charges $+Ze$ and $-Ze$, respectively, where Z is the valence and e the elementary charge. In terms of Cartesian coordinates xyz the electrolyte is confined to the semi-infinite space $x > 0$ by an impenetrable, homogeneous and planar insulating layer with dielectric constant ϵ_s placed at $-d < x < 0$, see Fig. 1. This layer either models a Stern layer or an oxide layer. The insulating layer is bounded by a conductor at $x < -d$ which has been biased at the surface $x = -d$ by a spatially modulated, external ac potential $V_{\rm ext}(y,t)$

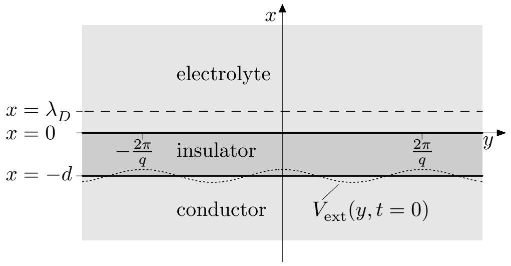

FIG. 1: A sketch of the system under study. The bi-ionic electrolyte is situated in the half space $x > 0$. Below it, for $-d < x < 0$, is a planar wall consisting of an insulating dielectric slab of thickness d and below that, for $x < -d$, is a semi-infinite conductor. The top surface, $x = -d$, of the conductor is biased by a periodically modulated potential $V_{\rm ext}(y,t)$ of period $2\pi/q$ (dotted line), which gives rise to the formation of a Debye screening layer of thickness λ_D in the electrolyte (dashed line).

$$V_{\rm ext}(y,t) = V_0 \cos(qy) e^{i\omega t}, \qquad (1)$$

where V_0 is the amplitude, q the wavenumber of the spatial modulation, and ω the driving angular frequency.

There is complete translation invariance along the z axis, so the z coordinate drops out of our analysis, and all positions $\mathbf{r} = (x, y)$ are therefore just refereing to the xy plane.

The manuscript is organized as follows: in Sec. II we introduce our non-equilibrium description and in Secs. III and IV we address the static and dynamic regimes, respectively. Finally, in Sec. V we discuss our results in relation to Refs. [1, 4] and in Sec. VI conclusions are given.

II. NON-EQUILIBRIUM DESCRIPTION

A. The insulating layer, $-d < x < 0$

The insulating layer contains neither free space charge nor free currents so the electrical potential $\phi(\mathbf{r},t)$ is governed by the Laplace equation,

$$\boldsymbol{\nabla}^2 \phi(\mathbf{r},t) = 0, \quad \text{for } -d < x < 0. \qquad (2)$$

B. The electrolyte, $x > 0$

In the liquid electrolyte we consider the ionic densities $n^{\pm}(\mathbf{r},t)$, the potential $\phi(\mathbf{r},t)$, the ionic current densities (the ionic flux densities) $\mathbf{i}^{\pm}(\mathbf{r},t)$, the velocity field $\mathbf{v}(\mathbf{r},t)$ of the electrolyte, and the pressure field $p(\mathbf{r},t)$.

The number densities of the ions couple to the potential via Poisson's equation,

$$\boldsymbol{\nabla}^2\phi(\mathbf{r},t) = -\frac{Ze}{\epsilon}\big[n^+(\mathbf{r},t) - n^-(\mathbf{r},t)\big]. \tag{3a}$$

The ionic current densities are coupled to the ionic densities by a continuity equation, which in the absence of any chemical reactions in the system is

$$\partial_t n^{\pm}(\mathbf{r},t) = -\boldsymbol{\nabla}\cdot\mathbf{i}^{\pm}(\mathbf{r},t). \tag{3b}$$

The presence of convection or of gradients in the densities $n^{\pm}(\mathbf{r},t)$ and the electric potential $\phi(\mathbf{r},t)$ will generate ionic current densities $\mathbf{i}^{\pm}(\mathbf{r},t)$. These currents are given by the Nernst–Planck equation

$$\begin{aligned}\mathbf{i}^{\pm}(\mathbf{r},t) = &-D\boldsymbol{\nabla}n^{\pm}(\mathbf{r},t) + n^{\pm}(\mathbf{r},t)\mathbf{v}(\mathbf{r},t)\\ &\mp \mu n^{\pm}(\mathbf{r},t)\boldsymbol{\nabla}\phi(\mathbf{r},t),\end{aligned} \tag{3c}$$

where, for simplicity, we have assumed that the two types of ions have the same diffusion constant D and the same mobility μ. We remind the reader that both the diffusion constant D and the electric conductivity σ are linked to the mobility μ via the Einstein relation $D = \frac{k_\mathrm{B}T}{Ze}\,\mu$ and $\sigma^{\pm} = Zen^{\pm}\mu$.

Finally, the velocity field and pressure field of the liquid are coupled to the potential and ionic densities by the Navier–Stokes equation

$$\begin{aligned}\rho\big[\partial_t\mathbf{v}(\mathbf{r},t) + \mathbf{v}(\mathbf{r},t)\cdot\boldsymbol{\nabla}\mathbf{v}(\mathbf{r},t)\big] &= -\boldsymbol{\nabla}p(\mathbf{r},t)\\ +\eta\boldsymbol{\nabla}^2\mathbf{v}(\mathbf{r},t) - Ze\big[n^+(\mathbf{r},t) &- n^-(\mathbf{r},t)\big]\boldsymbol{\nabla}\phi(\mathbf{r},t),\end{aligned} \tag{3d}$$

where ρ is the mass density, η is the viscosity of the liquid, and p is the pressure. Furthermore, treating the electrolyte as an incompressible fluid we have

$$\boldsymbol{\nabla}\cdot\mathbf{v}(\mathbf{r},t) = 0. \tag{3e}$$

The five coupled equations, Eqs. (3a) to (3e), fully govern the five physical quantities $n^{\pm}$, ϕ, $\mathbf{i}^{\pm}$, $\mathbf{v}$, and p.

C. Boundary conditions

Assuming a vanishing zeta-potential (*i.e.*, no unpassivated surface charges on the insulator-electrolyte interface), the boundary condition for the electric potential is

$$\phi(\mathbf{r},t)\big|_{x=-d} = V_\mathrm{ext}(y,t), \tag{4a}$$

$$\phi(\mathbf{r},t)\big|_{x=\infty} = 0. \tag{4b}$$

At the interface between the electrolyte and the insulating region the normal component of the ionic current density vanishes,

$$0 = \partial_x n^{\pm}(\mathbf{r},t)\big|_{x=0} \pm \frac{Ze}{k_BT}n^{\pm}(\mathbf{r},t)\partial_x\phi(\mathbf{r},t)\big|_{x=0}. \tag{5}$$

Here, we have utilized Eq. (3c) and the absence of convection at the interface due to the no-slip boundary condition,

$$\mathbf{v}(\mathbf{r},t)\big|_{x=0} = \mathbf{0}. \tag{6}$$

For the ionic densities we have

$$n^{\pm}(\mathbf{r},t)\big|_{x=\infty} = n_\infty, \tag{7}$$

where n_∞ is the homogeneous density of either of the two types of ions in the absence of an external perturbation, *i.e.*, when $V_0 = 0$. For the pressure, we assume that we have no externally applied pressure gradients so that p is the internal pressure caused by fluid flow and the electrical forces on the ions.

III. STATIC REGIME, $\omega = 0$

In the static regime we have equilibrium and neither current nor fluid flow, *i.e.*, $\mathbf{i}^{\pm} = \mathbf{0}$ and $\mathbf{v} = \mathbf{0}$. The pressure gradient balances the electrical forces on the charges. The governing equations for ϕ and $n^{\pm}$ of course reduce to those of electro-statics.

In the insulating layer $\phi(\mathbf{r})$ follows from Eqs. (2) and (4a),

$$\phi(\mathbf{r}) = \Big[\mathscr{C}_1 e^{-qx} + \mathscr{C}_2 e^{qx}\Big]\cos(qy), \quad \text{for } -d < x < 0, \tag{8}$$

where $\mathscr{C}_{1,2}$ are integration constants.

In the electrolyte $\phi(\mathbf{r})$ is governed by the Poisson–Boltzmann equation which in the Debye–Hückel approximation $ZeV_0 \ll k_BT$ becomes (see, *e.g.*, Sec. IV A below or Ref. [11])

$$\boldsymbol{\nabla}^2\phi(\mathbf{r}) = \lambda_D^{-2}\phi(\mathbf{r}). \tag{9}$$

Here, we have introduced the Debye screening length

$$\lambda_D \equiv \sqrt{\frac{\epsilon k_\mathrm{B}T}{2Z^2e^2n_\infty}}. \tag{10}$$

The space charge follows from Poisson's equation, Eq. (3a). From a straightforward solution for ϕ and $Ze(n^+ - n^-)$ we arrive at the following expression relating the total potential drop across the system and accumulated charge in the electrolyte,

$$\phi(\infty,y) - \phi(-d,y) \equiv \frac{\int_0^\infty dx\,Ze[n^+(\mathbf{r}) - n^-(\mathbf{r})]}{C_\mathrm{eff}}. \tag{11a}$$

The coefficient,

$$\begin{aligned}C_\mathrm{eff}^{-1} = &\big[1 + (q\lambda_D)^2\big]\frac{\sinh(qd)}{qd}\,C_s^{-1}\\ &+ \sqrt{1 + (q\lambda_D)^2}\,\cosh(qd)\,C_D^{-1},\end{aligned} \tag{11b}$$

is identified as the inverse of an effective series capacitance. The constant C_s is the intrinsic surface capacitance and C_D the capacitance of the Debye layer given by

$$C_s \equiv \frac{\epsilon_s}{d}, \tag{11c}$$

$$C_D \equiv \frac{\epsilon}{\lambda_D}. \tag{11d}$$

In Ref. [1] the potential in the bulk of the electrolyte ($x \gg \lambda_D$) is governed by the Laplace equation which is coupled to the external potential V_{ext} by an effective capacitance $C_{\text{eff}} = \left(C_s^{-1} + C_D^{-1}\right)^{-1}$. As shown above this approach is valid up to second order in the small parameters $q\lambda_D \ll 1$ and $qd \ll 1$.

IV. DYNAMIC REGIME, $\omega > 0$

We now solve Eqs. (3) in the dynamic regime, $\omega > 0$. First the ionic current densities are eliminated by inserting Eq. (3c) into Eq. (3b). Using the incompressibility of the fluid, Eq. (3e), we get the continuity equation

$$\begin{aligned}\partial_t n^{\pm}(\mathbf{r},t) = D\, \boldsymbol{\nabla}^2 n^{\pm}(\mathbf{r},t) - [\boldsymbol{\nabla} n^{\pm}(\mathbf{r},t)]\cdot \mathbf{v}(\mathbf{r},t)\\ \pm \mu \boldsymbol{\nabla}\cdot\big[n^{\pm}(\mathbf{r},t)\, \boldsymbol{\nabla}\phi(\mathbf{r},t)\big].\end{aligned} \tag{12}$$

A. Debye–Hückel approximation

To advance further by analytical methods, we now linearize the continuity equation, Eq. (12), in the density as follows. We assume $n^{\pm}(\mathbf{r},t)\big|_{x=\infty} \equiv n_\infty$ and write

$$n^{\pm}(\mathbf{r},t) = n_\infty + \delta n^{\pm}(\mathbf{r},t), \qquad \lim_{x\to\infty} \delta n^{\pm}(\mathbf{r},t) = 0. \tag{13}$$

It is a non-zero V_0 that spawns $\delta n^{\pm} \neq 0$, and when the applied voltage V_0 is much smaller than the thermal voltage V_T, defined by $V_T \equiv k_{\text{B}}T/Ze$, we have $|\delta n_0^{\pm}| \ll n_\infty$. In this limit the so-called Debye–Hückel approximation is valid, and $n^{\pm}(\mathbf{r},t)\, \boldsymbol{\nabla}\phi(\mathbf{r},t)$ is substituted by $n_\infty\, \boldsymbol{\nabla}\phi(\mathbf{r},t)$ in Eq. (12). We subsequently use Eq. (3a) to replace $\boldsymbol{\nabla}^2\phi(\mathbf{r},t)$ with $-\nu(\mathbf{r},t)/\epsilon$ where

$$\nu(\mathbf{r},t) \equiv n^+(\mathbf{r},t) - n^-(\mathbf{r},t) = \delta n^+(\mathbf{r},t) - \delta n^-(\mathbf{r},t). \tag{14}$$

Finally, we form the difference of the "±"-versions of Eq. (12) and obtain the partial differential equation

$$\partial_t \nu(\mathbf{r},t) = \left[D\boldsymbol{\nabla}^2 - D\frac{1}{\lambda_D^2} - \mathbf{v}(\mathbf{r},t)\cdot\boldsymbol{\nabla}\right]\nu(\mathbf{r},t). \tag{15}$$

B. Diffusive regime

From our study of the static regime we know that the net charge density is non-zero only in the Debye layer, $x \lesssim \lambda_D$. In this region the velocity will be vanishing because of the no-slip boundary condition. Thus, diffusion will dominate so that convection can be neglected, and the electro- and hydro-dynamic problems decouple. Since the density difference ν changes over the length scales λ_D and q^{-1} for the x and y directions, respectively, the condition for the decoupling is $|v_x|/\lambda_D + |v_y|q \ll Dq^2$ for $0 < x \lesssim \lambda_D$. In this limit Eq. (15) has a general $\cos(qy)e^{i\omega t}$ modulated decaying solution of the form

$$\nu(\mathbf{r},t) = \mathscr{C}_1 e^{-\kappa x}\cos(qy)e^{i\omega t}\ ,\ x > 0, \tag{16a}$$

where the decay parameter κ depends on the Debye frequency ω_D,

$$\kappa \equiv \frac{1}{\lambda_D}\sqrt{1 + (q\lambda_D)^2 + i\,\frac{\omega}{\omega_D}}, \tag{16b}$$

$$\omega_D \equiv \frac{D}{\lambda_D^2}. \tag{16c}$$

For the potential we seek a solution of a form similar to Eq. (16a), $\phi \propto \cos(qy)e^{i\omega t}$, and substituting this together with Eq. (16a) into Eq. (3a) yields

$$(\partial_x^2 - q^2)\phi(\mathbf{r},t) = -\frac{Ze}{\epsilon}\mathscr{C}_1 e^{-\kappa x}\cos(qy)e^{i\omega t}. \tag{17}$$

Demanding $\phi(\mathbf{r},t)\big|_{x=\infty} = 0$ the solution is

$$\begin{aligned}\phi(\mathbf{r},t) = &\Big[\mathscr{C}_1\frac{Ze}{\epsilon}(q^2-\kappa^2)^{-1}e^{-\kappa x} + \mathscr{C}_2 e^{-qx}\Big]\\ &\times \cos(qy)e^{i\omega t}, \quad x > 0.\end{aligned} \tag{18}$$

In the insulating layer we have the following $\cos(qy)e^{i\omega t}$ modulated general solution to Eq. (2),

$$\phi(\mathbf{r},t) = \Big[\mathscr{C}_3 e^{-qx} + \mathscr{C}_4 e^{qx}\Big]\cos(qy)e^{i\omega t}\ ,\ -d < x < 0. \tag{19}$$

In order to determine $\mathscr{C}_n$ ($n = 1,2,3,4$) we first consider the boundary condition for the current. Applying the Debye–Hückel approximation to the second term in Eq. (5) and forming the difference of the "±" solutions we arrive at

$$0 = \partial_x\Big[\nu(\mathbf{r},t) + \frac{C_D}{Ze\lambda_D}\phi(\mathbf{r},t)\Big]\Big|_{x=0}. \tag{20}$$

Together with the boundary condition for ϕ at $x = -d$ as well as the continuity of ϕ and $\epsilon\partial_x\phi$ at $x = 0$ we may determine the constants straightforwardly.

C. Long-period and low-frequency modulation

Next, we consider the regime where the spatial period of the modulation is much longer than all other length scales, *i.e.*, $q\lambda_D \ll 1$ and $qd \ll 1$. We also assume that $\omega \ll \omega_D$ so that $\kappa \simeq 1/\lambda_D$. In this limit we get

$$\nu(\mathbf{r},t) = -\frac{q\sigma_\infty V_0}{Ze\lambda_D}\frac{1}{\omega^* + i\omega}e^{-x/\lambda_D}\cos(qy)e^{i\omega t} + \mathcal{O}([q\lambda_D]^2), \tag{21}$$

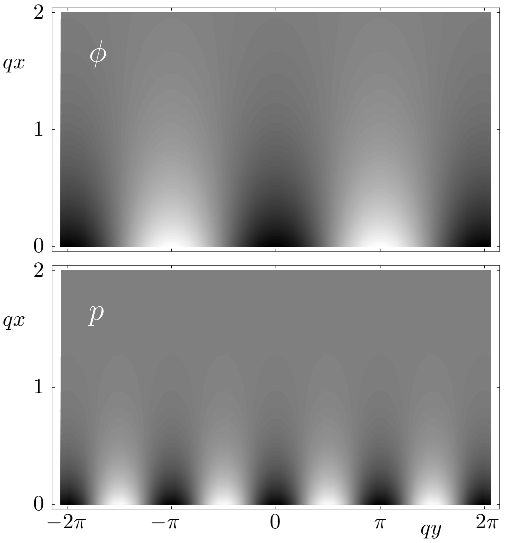

FIG. 2: Top and bottom panels are gray scale plots of the amplitudes of the potential $\phi(\mathbf{r},t)$ [see Eq. (22)] and of the pressure $p(\mathbf{r},t)$ [see Eq. (31)] as a function of qx and qy. Notice the period doubling in the pressure field compared to the electric potential.

and

$$\phi(\mathbf{r},t) = V_0 \frac{i\omega}{\omega^* + i\omega} e^{-qx}\cos(qy)e^{i\omega t} + \mathcal{O}(q\lambda_D), \tag{22}$$

where we have used the notation of Ajdari [1]

$$\text{resonance frequency: } \omega^* = q\lambda_D(1+\delta)\,\omega_D, \tag{23a}$$

$$\text{conductivity: } \sigma_\infty = \left[\sigma^+ + \sigma^-\right]\Big|_\infty = \epsilon\omega_D, \tag{23b}$$

$$\text{capacitance ratio: } \delta = \frac{C_D}{C_s}. \tag{23c}$$

These results are equivalent to those in Ref. [1] if we similarly to Eq. (11a) introduce the Debye layer surface charge $\sigma_D(y) = Ze\int_0^\infty dx\,\nu(x,y)$.

D. Body-force

Until this point we have used the exponential notation for the temporal dependence. However, since the body-force is essentially non-linear in the electrical potential/density [see last term in Eq. (3d)] we have to take the real part to get the body-force, *i.e.*, $\mathbf{F} = -Ze\nu\boldsymbol{\nabla}\phi = -Ze\mathrm{Re}\{\nu\}\mathrm{Re}\{\boldsymbol{\nabla}\phi\}$ so that we get

$$\mathbf{F}(\mathbf{r},t) = \frac{\eta v_1}{\lambda_D^2}\,\frac{\cos(2\omega t+\varphi)}{\frac{\omega}{\omega^*}+\frac{\omega^*}{\omega}}\,e^{-x/\lambda_D} \times\left[2\cos^2(qy)\mathbf{e}_x + \sin(2qy)\mathbf{e}_y\right] + \mathcal{O}\big([q\lambda_D]^2\big) \tag{24a}$$

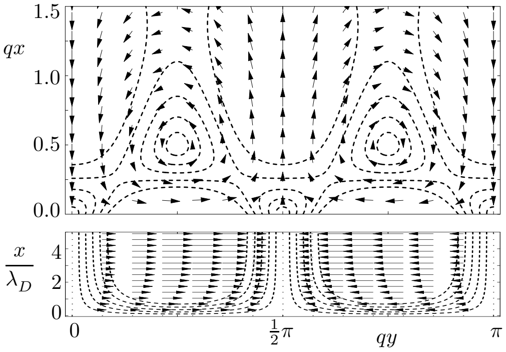

FIG. 3: Vector-plots of the vector-amplitude of the velocity-field $\mathbf{v}(\mathbf{r},t)$ in the bulk [top panel] given by Eq. (30) and in the Debye layer [bottom panel] given by Eq. (27). The flow pattern contains rolls (with a temporal harmonic motion), which are indicated by contours of constant velocity (dashed lines).

where we following Ref. [1] have introduced

$$v_1 \equiv \frac{q\epsilon V_0^2}{4\eta(1+\delta)} \tag{24b}$$

and the frequency dependent phase shift

$$\varphi = -\arctan\left(\frac{\omega}{2\omega^*} - \frac{\omega^*}{2\omega}\right). \tag{24c}$$

In the derivation of Eq. (24a) we have used that

$$\mathrm{Re}\left\{\frac{e^{i\omega t}}{i\omega+\omega^*}\right\}\mathrm{Re}\left\{\frac{i\omega e^{i\omega t}}{i\omega+\omega^*}\right\} = \frac{-1}{2\omega^*}\,\frac{\cos(2\omega t+\varphi)}{\frac{\omega}{\omega^*}+\frac{\omega^*}{\omega}}. \tag{25}$$

At low frequencies, $\mathbf{F} \propto \omega$, it becomes maximal at the resonance frequency ω^*, and then it falls off again at higher frequencies. We note that $\lim_{\omega\to 0}\mathbf{F} = \mathcal{O}\big([q\lambda_D]^2\big)$, but this small force will just be balanced by a pressure gradient so that $\lim_{\omega\to 0}\mathbf{v} = \mathbf{0}$ and $\lim_{\omega\to 0}\mathbf{i}^\pm = \mathbf{0}$.

E. Linearized flow in quasi-steady state

In order to solve the Navier–Stokes equation, Eq. (3d), we note that for a body-force of small magnitude and with slow temporal variation the fluid response is linear and the flow will approximately be at steady state at each moment in time. We begin by comparing the inertial terms on the left-hand side (LHS) with the viscous term (second term) on the right-hand side (RHS). The body force has a characteristic frequency ω and two characteristic length scales λ_D and q^{-1} for the x and y-directions, respectively. Since ∂_t essentially gives a factor of ω, and $\boldsymbol{\nabla}$ essentially gives $\lambda_D^{-1}\mathbf{e}_x + q\mathbf{e}_y$, we can show that the viscous term dominates over the LHS when

$\omega \ll \omega_c \equiv \frac{\eta}{\rho D}\,\omega_D$. This condition is easily fulfilled when $\omega \ll \omega_D$, since typically $\frac{\eta}{\rho D} \gg 1$, and Eq. (3d) then becomes

$$\mathbf{0} \simeq -\boldsymbol{\nabla} p(\mathbf{r},t) + \eta \boldsymbol{\nabla}^2 \mathbf{v}(\mathbf{r},t) + \mathbf{F}(\mathbf{r},t). \tag{26}$$

This is the resulting quasi-steady flow problem which is linear in the velocity field.

F. Debye layer flow

In order to solve Eqs. (3e) and (26) we study the flow over a λ_D-scale at the boundary first and then a q^{-1}-scale. For this boundary layer approach, we assume that for $x \lesssim \lambda_D$, we have $v_x \sim 0$. Solving for the pressure and substituting into the y-component of Eq. (26) we get

$$v_y(\mathbf{r},t) = v_s(y,t)\left(1 - e^{-x/\lambda_D}\right) + \mathcal{O}(q\lambda_D),\ x \lesssim \lambda_D \tag{27}$$

where the prefactor

$$v_s(y,t) \equiv v_1 \, \frac{\cos(2\,\omega\, t + \varphi)}{\frac{\omega}{\omega^*} + \frac{\omega^*}{\omega}} \, \sin(2\,q\,y), \tag{28}$$

in the limit $1/q \gg x \gtrsim \lambda_D$ can be interpreted as a slip-velocity at the wall acting as a conveyor belt for the bulk fluid (see bottom panel of Fig. 3).

G. Bulk flow

For $x \gtrsim \lambda_D$ we have that $\mathbf{F} \simeq \mathbf{0}$ and we solve Eq. (26) together with Eq. (3e) and the boundary condition

$$\mathbf{v}(\mathbf{r},t)\big|_{x=0} = v_s(y,t)\,\mathbf{e}_y. \tag{29}$$

To lowest order in $q\lambda_D$ this gives

$$\begin{aligned}\mathbf{v}(\mathbf{r},t) \simeq v_1 \, &\frac{\cos(2\,\omega\, t + \varphi)}{\frac{\omega}{\omega^*} + \frac{\omega^*}{\omega}} \, e^{-2qx} \\ &\times \Big(- 2qx\cos(2qy)\mathbf{e}_x + (1-2qx)\sin(2qy)\mathbf{e}_y \Big),\end{aligned} \tag{30}$$

and

$$p(\mathbf{r},t) \simeq 4q\eta v_1 \, \frac{\cos(2\omega t + \varphi)}{\frac{\omega}{\omega^*} + \frac{\omega^*}{\omega}} \, e^{-2qx}\cos(2qy). \tag{31}$$

If we now substitute into Eq. (3d) we get RHS $-$ LHS $\propto e^{-x/\lambda_D} + \mathcal{O}(\omega/\omega_D) + \mathcal{O}([q\lambda_D]^2)$ which shows that Eqs. (30) and (31) are indeed excellent approximations to the full solution of the non-linear time-dependent Navier–Stokes equation, Eq. (3d), for $x \gg \lambda_D$. For the incompressibility constraint, Eq. (3e), our solution gives $\boldsymbol{\nabla}\cdot\mathbf{v} = \mathcal{O}([q\lambda_D]^2)$. In Fig. 3 we show a field-plot of the velocity-field, Eq. (30), along with the contours for constant velocity.

TABLE I: Typical values of central parameters.

Spatial modulation	q^{-1}	10^{-5}	m
Insulator thickness	d	10^{-8}	m
Debye screening length	λ_D	10^{-8}	m
Resonance frequency	ω^*	10^{6}	s^{-1}
Debye frequency	$\omega_D = \sigma_\infty/\epsilon$	10^{7}	s^{-1}
Critical frequency	$\omega_c = (\eta/\rho D)\sigma_\infty/\epsilon$	10^{10}	s^{-1}
Thermal voltage	$V_T = k_B T/Ze$	25	mV
Critical voltage	$V_c = \sqrt{(1+\delta)\eta D/\epsilon}$	100	mV
Ionic density	n_∞	1	$\mathrm{mol\,L^{-1}}$
Viscosity	η	10^{-3}	Pa s
Mass density	ρ	10^{3}	$\mathrm{kg\,m^{-3}}$
Ionic diffusion constant	D	10^{-9}	$\mathrm{m^2\,s^{-1}}$
Capacitance ratio	$\delta = C_D/C_s$	10	

V. DISCUSSION

We have analyzed the full non-equilibrium electro-hydrodynamics of the Debye screening layer that arises in an aqueous bi-ionic solution near a planar wall when applying a spatially modulated ac-voltage $V_0\cos(qy)e^{i\omega t}$, Eq. (1). Our analysis applies to the low-frequency Debye–Hückel regime where the amplitude V_0 of the external potential is lower than the thermal voltage V_T and the driving frequency ω is lower than the inverse response-time of the electrolyte $\omega_D = \sigma_\infty/\epsilon$ (see Secs. IV A and IV C). Furthermore, we have limited ourselves to the diffusive regime where convection can be neglected corresponding to a sufficiently low driving amplitude, $V_0 \ll V_c$ where $V_c \equiv \sqrt{(1+\delta)\eta D/\epsilon}$ is a critical voltage [see first paragraph of Sec. IV B, $\mathbf{v} \sim v_1\mathbf{e}_y$ in the Debye layer]. We have also considered the low-frequency regime $\omega \ll \omega_c$ where viscosity dominates over inertia (see Sec. IV E). Finally, we have considered the limit with the spatial modulation being much longer than all other length scales in the problem, i.e. $qd \ll 1$ and $q\lambda_D \ll 1$ (see Sec. IV C). In summary this means that we have studied the effect of Eq. (1) in the limits

$$q \ll \min\left\{d^{-1},\ \lambda_D^{-1}\right\}, \tag{32a}$$

$$\omega \ll \min\left\{\omega_D,\ \omega_c\right\}, \tag{32b}$$

$$V_0 \ll \min\left\{V_T,\ V_c\right\}. \tag{32c}$$

Typical values of our parameters are listed in Table I.

Using first order perturbation theory we have obtained analytic solutions for the pressure and velocity field of the electrolyte and for the electric potential. The solutions have been obtained both in the narrow Debye layer on the length scale λ_D and in the bulk on the larger length scale $1/q$ set by the period of the applied external potential. As a main result we have supplied a proof for the validity of the phenomenological capacitor model.

The full dynamics seems however not to be captured by the capacitor model. Taking the time-average in Eqs. (24a) and (30) we get $\left\langle\mathbf{F}\right\rangle_t = \mathbf{0}$ and $\left\langle\mathbf{v}\right\rangle_t = \mathbf{0}$ (in full agreement with the discussion in Ref. [1]). In contrast, we obtain $\left\langle\mathbf{F}\right\rangle_t \neq \mathbf{0}$ if we begin from Eqs. (16a) and (18) without expanding in ω/ω_D and $q\lambda_D$ (the result is finite even in the zero-frequency limit). Somewhat similar results were reported in another non-equilibrium study [4], though for a different geometry. Naively, this observation could suggest that $\langle \mathbf{v} \rangle_t \neq \mathbf{0}$ contrary to the statement in Ref. [1]. However, by also averaging over the y-direction we get $\langle F_y \rangle_{t,y} = 0$ suggesting that $\langle v_y \rangle_{t,y} = 0$ in agrement with the symmetry arguments emphasized in Ref. [1]. If the finite $\langle \mathbf{F} \rangle_t$ does not give the fluid a directional flow globally, we might speculate that, at high frequencies, it makes the fluid circulate in non-oscillating vortices (with a spatial pattern like in Fig. 3) whereas the fluid is at rest at zero-frequency – despite $\langle \mathbf{F} \rangle_t$ being finite. The solution to this apparent contradiction lies in the pressure which will compensate the body-force at low frequencies. This has not been pointed out previously in the literature. We can explicitly show that the time-averaged body-force can be written as a gradient-potential

$$\big\langle \mathbf{F}(\mathbf{r},t) \big\rangle_t = \nabla p_F(\mathbf{r}) + \mathcal{O}\big([\omega/\omega_D]^2\big) \tag{33}$$

where

$$p_F(\mathbf{r}) = p_0 + \frac{\frac{1}{4}\epsilon q^2 V_0^2}{\Big[q\lambda_D \cosh(qd) + \frac{\epsilon}{\epsilon_s}\sqrt{1+(q\lambda_D)^2}\,\sinh(qd)\Big]^2} \times e^{-2\sqrt{1+(q\lambda_D)^2}\,x/\lambda_D}\cos^2(qy) \tag{34}$$

with p_0 being a constant. Introducing the effective capacitance, Eq. (11b), we can also write this as

$$p_F(\mathbf{r}) = p_0 + q\eta v_1 \left(1 + \frac{C_D}{C_s}\right)\left(\frac{C_{\text{eff}}}{C_D}\right)^2 \frac{1+(q\lambda_D)^2}{(q\lambda_D)^2} \times e^{-2\sqrt{1+(q\lambda_D)^2}\,x/\lambda_D}\cos^2(qy). \tag{35}$$

The form of Eq. (33) suggests that

$$\big\langle \mathbf{v}(\mathbf{r},t) \big\rangle_t = \mathbf{0} + \mathcal{O}\big([\omega/\omega_D]^2\big) \tag{36}$$

with p_F being a pressure that compensates the low-frequency part of the body force, see Eq. (26). At high frequencies we expect vortices to co-exist with the harmonic fluid motion described in Eq. (30) whereas at low frequencies the circulation vanishes and we are left with the pure harmonic motion. Time-dependent finite-element simulations seem to confirm this picture [12] and similar time-averaged flow in a slightly different geometry has been observed both experimentally, theoretically, and numerically [3–5].

VI. CONCLUSION

Our results provide the theoretical underpinning of the phenomenological capacitor model widely used in the literature [1–3, 5, 13, 14], and form a firm starting point for future studies of electro-kinetic pumps and mixers driven by spatially modulated surface potentials. However, our non-equilibrium approach has also revealed interesting short-comings in the capacitor approach in [1] for high-frequency dynamics where vortices may appear along with the harmonic rolls also predicted by the capacitor model.

Acknowledgement

We thank T. S. Hansen for sharing his numerical results with us. N. A. M. is supported by The Danish Technical Research Council (Grant No. 26-03-0073) and L. B. by a Socrates/Erasmus grant from the European Community.

[1] A. Ajdari, Phys. Rev. E **61**, R45 (2000).

[2] A. B. D. Brown, C. G. Smith, and A. R. Rennie, Phys. Rev. E **63**, 016305 (2000).

[3] N. G. Green, A. Ramos, A. Gonzalez, H. Morgan, and A. Castellanos, Phys. Rev. E **61**, 4011 (2000).

[4] A. Gonzalez, A. Ramos, N. G. Green, A. Castellanos, and H. Morgan, Phys. Rev. E **61**, 4019 (2000).

[5] N. G. Green, A. Ramos, A. Gonzalez, H. Morgan, and A. Castellanos, Phys. Rev. E **66**, 026305 (2002).

[6] A. Ajdari, Phys. Rev. E **65**, 016301 (2002).

[7] I. Gitlin, A. D. Stroock, G. M. Whitesides, and A. Ajdari, Appl. Phys. Lett. **83**, 1486 (2003).

[8] S. R. Yeh, M. Seul, and B. I. Shraiman, Nature **386**, 57 (1997).

[9] A. Ramos, H. Morgan, N. G. Green, and A. Castellanos, J. Phys. D Appl. Phys. **31**, 2338 (1998).

[10] H. A. Stone, A. D. Stroock, and A. Ajdari, Annu. Rev. Fluid Mech. **36**, 381 (2004).

[11] R. Feynman, R. B. Leighton, and M. L. Sands, *The Feynman lectures on physics*, vol. 2 (Addison-Wesley Publishing Company, Reading, Massachusetts, 1964).

[12] T. S. Hansen *et al.*, unpublished (2004).

[13] F. Nadal, F. Argoul, P. Kestener, B. Pouligny, C. Y. C, and A. Ajdari, Eur. Phys. J. E **9**, 387 (2002).

[14] H. Morgan and N. G. Green, *AC Electrokinetics: colloids and nanoparticles*, Microtechnologies and Microsystems series (Institute of Physics Publishing, Bristol, 2003).

Bibliography

[1] A. B. D. Brown, C. G. Smith, and A. R. Rennie. 'Pumping of water with ac electric fields applied to asymmetric pairs of microelectrodes.' Phys. Rev. E 63, 016305 (2000).

[2] M.Mpholo, C. Smith, and A. Brown. 'Low voltage plug flow pumping using anisotropic electrode arrays.' Sens. Actuators B Chem. 92, 262 (2003).

[3] J. Kirchheiner, L. Bertilsson, H. Bruus, A. Wolff, I. Roots, and M. Bauer. 'Individualized Medicne - Implementation of Pharmacogenetic Diagnostics in Antidepressant Drug Treatment of Major Depressive Disorders.' Pharmacopsychiatry 36, S235 (2003).

[4] D. J. Laser and J. G. Santiago. 'A review of micropumps.' J. Micromech. Microeng 14, R35 (2003).

[5] H. A. Stone, A. D. Stroock, and A. Ajdari. 'Engineering flows in small devices: Microfluidics toward a lab-on-a-chip.' Annu. Rev. Fluid Mech. 36, 381 (2004).

[6] A. Ajdari. 'Pumping liquids using asymmetric electrode arrays.' Phys. Rev. E 61, R45 (2000).

[7] M. Washizu, S.Suzuki, 0.Kurosawa, T. Nishizaka, and T.Shinohara. 'Molecular dielectrophoresis of biopolymers.' IEEE Trans. Ind. Appl. 30, 835 (1994).

[8] A. Brask, H.Bruus, and J. P. Kutter. 'Electroosmotic pump with ion exchange membranes and a current feedback for flow control.' μTAS 2003, Lake Taho, USA, October 2003, proc. 1, 223 (2003).

[9] M.Arnoldus and M.Hansen. *B.Sc., Asymmetric electrode micropumps* (MIC, 2004).

[10] N. A. Mortensen, L. Belmon, L. H. Olesen, and H. Bruus. 'Electro-hydrodynamics of bi-ionic electrolytes driven by modulated surface potentials.' submitted to Phys. Rev. E (2004). Http://arxiv.org/cond-mat/0407160.

[11] R. F. Probstein. *PhysicoChemical Hydrodynamics, an introduction* (John Wiley and Sons, New-York, 1994).

[12] L. D. Landau and E. M. Lifshitz. *Fluid Mechanics*, volume 6 of *Landau and Lifshitz, Course of Theoretical Physics* (Butterworth-Heinemann, Oxford, 1987), 2nd edition.

[13] A. Brask. *M.Sc. thesis, Principles of electroosmotic pumps* (MIC, 2002).

[14] M. Z. Bazant, K. Thornton, and A. Ajdari. 'Diffuse-Charge Dynamics in Electrochemical Systems.' unpublished (2004). Http://fr.arxiv.org/abs/cond-mat/0401118.

[15] Ómar Gústafsson. *M.Sc. thesis, Application of Stationary Phases in Microfluidic Channels* (MIC, 2004).

[16] V. Studer, A. Pepin, C. Y, and A. Ajdari. 'Fabrication of microfluidic devices for AC electrokinetic fluid pumping.' Microelectron. Eng. 61, 915 (2002).

[17] N. G. Green, A. Ramos, A. Gonzalez, H. Morgan, and A. Castellanos. 'Fluid flow induced by nonuniform ac electric fields in electrolytes on microelectrodes. I. Experimental measurements.' Phys. Rev. E 61, 4011 (2000).

[18] Y.Takamura, H. Onoda, H. Inokuchi, S. Adachi, A. Oki, and Y. Horiike. *Micro Total Analysis Systems 2001, proc.* (J. M. Ramsey and A. van den Berg (eds.)Kluwer Academic Publishers, 2001).

[19] A. Brask, H. Bruus, and J. P. Kutter. 'Long-term stability for frit-based EO pumps under varying load conditions using ion exchange membranes with controlled diffusion layer widths.' Accepted at muTAS-2004, Malmö, Sweden, March 2004 (2004).

[20] A. Gonzalez, A. Ramos, N. G. Green, A. Castellanos, and H. Morgan. 'Fluid flow induced by nonuniform ac electric fields in electrolytes on microelectrodes. II. A linear double-layer analysis.' Phys. Rev. E 61, 4019 (2000).

[21] V. Studer, A. Pepin, C. Y, and A. Ajdari. 'Fast and tunable integrated AC electrokinetic pumping in a microfluidic loopg.' unpublished (2004). Http://hogarth.pct.espci.fr/ armand/.

[22] R. Feynman, R. B. Leighton, and M. L. Sands. *The Feynman lectures on physics*, volume 2 (Addison-Wesley Publishing Company, Reading, Massachusetts, 1964).

[23] L. H. Olesen. *M.Sc. thesis, Computational Fluid Dynamics in microfluidic systems* (MIC, 2003).

[24] H.Kardestuncer. *Finite Element Handbook* (McGraw-Hill, New-York, 1987).

[25] Comsol support and Femlab documentation, www.comsol.com.

[26] N. G. Green, A. Ramos, A. Gonzalez, H. Morgan, and A. Castellanos. 'Fluid flow induced by nonuniform ac electric fields in electrolytes on microelectrodes. III. Observation of streamlines and numerical simulation.' Phys. Rev. E 66, 026305 (2002).